Exotic Phases in Frustrated Low Dimensional Spin Systems

A Thesis submitted for the degree of
Doctor of Philosophy (Science)
in
Physics (Theoretical)

by

Aslam Parvej

Department of Physics
University of Calcutta
2018

Dedicated to my family . . .

List of publications

Included in the thesis

1. *"Level crossing, spin structure factor and quantum phases of the frustrated spin-1/2 chain with first and second neighbor exchange"*, Manoranjan Kumar, **Aslam Parvej**, and Zoltán G. Soos, J. Phys.: Condens. Matter **27**, 316001 (7pp) (2015).
2. *"Numerical study of incommensurate and decoupled phases of spin-1/2 chains with isotropic exchange J_1, J_2 between first and second neighbors"*, Zoltán G. Soos, **Aslam Parvej**, and Manoranjan Kumar, J. Phys.: Condens. Matter **28**, 175603 (12pp) (2016).
3. *"Degeneracies and exotic phases in an isotropic frustrated spin-1/2 chain"*, **Aslam Parvej** and Manoranjan Kumar, J. Mag. Mag. Mat. **401**, 96-101 (2016).
4. *"Multipolar phase in frustrated spin-1/2 and spin-1 chains"*, **Aslam Parvej** and Manoranjan Kumar, Phys. Rev. B **96**, 054413 (2017).
5. *"Study of the dynamical properties of the multipolar phase of spin-1/2 chain"*, **Aslam Parvej**, Monalisa Singh Roy, and Manoranjan Kumar (in preparation)

Other works

1. *"Efficient density matrix renormalization group algorithm to study Y junctions with integer and half-integer spin"*, Manoranjan Kumar, **Aslam Parvej**, Simil Thomas, S. Ramasesha, and Zoltán G. Soos, Phys. Rev. B **93**, 075107 (2016).
2. *"Density matrix renormalization group (DMRG) for cyclic and centrosymmetric linear chains"*, Manoranjan Kumar, Dayasindhu Dey, **Aslam Parvej**, S. Ramasesha, and Zoltán G. Soos, arXiv:1610:00998 (2016).

Acknowledgements

I would like to express my sincere thanks to all the people who helped me to reach this present position. At the onset, I would like to acknowledge and extend my heartfelt gratitude to my supervisor Dr. Manoranjan Kumar for the continuous and immeasurable support throughout my Ph.D. tenure. His patience, motivation and immense knowledge that he imparted helped me to proceed with my research work smoothly. The successful completion of my research work and thesis was possible due to his excellent guidance and encouragement. I would always remain grateful and indebted to him for his mentor-ship.

I also extend my sincere gratitude to Prof. Zoltán G. Soos from Dept. Of Chemistry at Princeton University. I am extremely thankful and indebted to him for sharing expertise, sincere and valuable guidance and for the encouragement that he extended to me. I would like to thank and be grateful to Prof. S. Ramasesha from Dept. of Solid State and Structural Chemistry unit at IISC Bangalore.

My sincere thanks also goes to Prof. Priya Mahadevan who guided me in the process of selection of the supervisor in the beginning of my Ph.D. career in the S.N. Bose centre. So her help and support provided me a great opportunity to join and work with Dr. Manoranjan Kumar. I take this opportunity to express gratitude to all my respected teachers specially Madam Samapti and Sir Bhupati from City College, University of Calcutta from where I earned my B.Sc. degree. I would also like to thank Dr. Aritra Banerjee, Prof. Debnarayan Jana, Prof. Parongama Sen, Dr. Biswajit Ray, Dr. Sourish Banerjee from Rajabazar Science College, University of Calcutta from where I earned my M.Sc. degree, for their help and unconditional support. Raju da, one of my favourite person played a very crucial role in my academic as well as personal life which really helped me a lot.

I thank my fellow lab-mates Rakesh, Sudipta, Debasmita, Monalisa, Sudip, Koushik, Daya Da for their stimulating discussions and help, and for all the fun that we had in the last five years. I also thank Subhajit Da, Biplab Da, Semanti Di, Rupali, Monalisa, Poulami, Debasis, Subhadip, Subrata, Kartik, Sagar, Sarowar Da, Somnath, Rajkumar, Maheboob, Ejaj, Keshab, Animesh Da, Siddhi Di,Arindam Da, Ananda and the entire SNB family.

Last but not the least, I would like to thank my family that includes my parents, sister, brothers, my partner for supporting me spiritually and unconditionally throughout my Ph.D. tenure and my life in general.

Contents

List of Figures

List of Tables

Chapter 1

Introduction

1.1 Frustrated Low Dimensional Quantum Spin System

The study of physical properties of materials is one of the most emerging branches of condensed matter physics. The frontier research in this field leads to many new materials which can be used in our daily life like Light emitting diodes (LED's), organic polymer based touch screens, storage devices, magnetic sensors, high speed RAM etc.

Most of the bulk materials are generally three dimensional (3D), but in some cases they can effectively behave as a low dimensional (LD) system. The LD system includes one dimensional (1D), quasi-1D or two dimensional (2D) systems. The 3D system can effectively be treated as a LD system if the inter-atomic distance (bond length) in one direction is quite small compared to other directions. For example, if the inter-atomic coupling along x-direction is much stronger than y and z-direction then all the electronic properties are confined along x-direction. In these LD systems the quantum fluctuations are dominant because of particles confinement, and these fluctuations lead to many interesting phases.

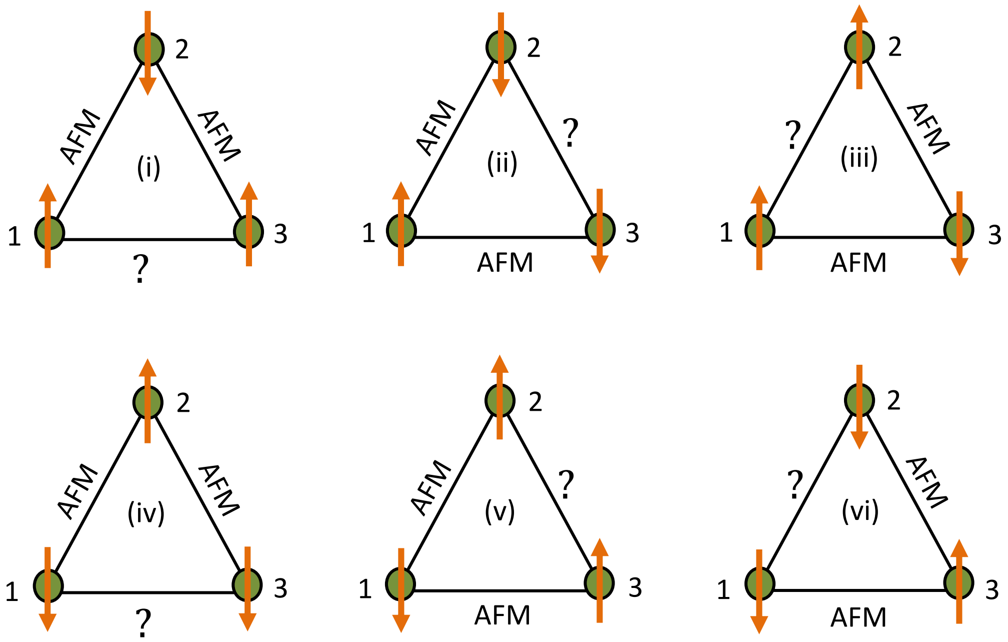

Figure 1.1: Schematic representation of the geometrical frustration. In each triangle Ising spins are interacting through nearest neighbor AFM interaction. There are total six configurations numbered as (i)-(vi) with minimum energy. In each configuration one bond is frustrated.

In the last nine decades, studies of the LD systems were mostly theoretical. The 1D Ising model is one of the oldest and simplest models, and later the exact solution of 2D Ising model was given by Onsager [1]. He showed that the 2D system exhibits spontaneous order. The isotropic Heisenberg model for a spin-1/2 chain was studied by Bethe, and he calculated the ground state (gs) energy and correlation function of this model using the Bethe ansatz technique [2]. Quasi-1D and 2D model systems are extensively studied numerically [3]. Some of these models are relevant to real materials and helps us to understand the properties of the material. In the last four decades tremendous effort has been put to synthesize, characterize and understand the experimental findings of the LD systems [4]. These studies show many interesting properties like magnon condensation, spin liquid, dimer order, vector chiral etc. In the last few decades many 1D system like $LiCuVO_4$ [5], $LiCuSbO_4$ [6], $LiCu_2O_2$ [7] etc. and quasi-1D like $Ba_3Cu_3Sc_4O_{12}$ [8], $Ba_3Cu_3In_4O_{12}$ [9] systems have been synthesized which show interesting behavior. Some of these systems form frustrated magnets.

The frustrated magnetic systems in LD are abundant in nature, and their studies

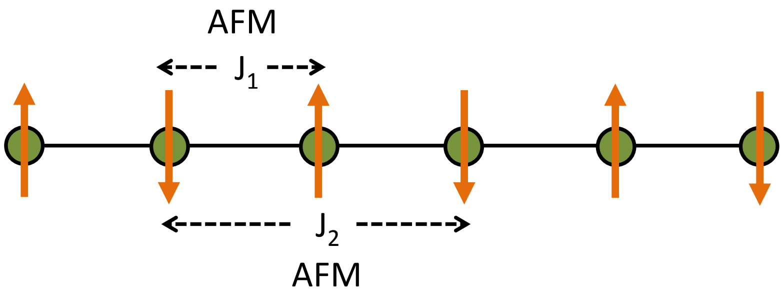

Figure 1.2: A 1D chain where spins are interacting with AFM nearest neighbor interaction (J_1) and AFM next nearest neighbor interaction (J_2). Due to the next nearest neighbor interaction the system is frustrated.

have been a frontier area of research in the last couple of decades. Recently the frustrated magnetic materials has attracted lots of attention due to the observation of the striking magnetic properties in experimental as well as in theoretical studies. A triangular lattice with anti-ferromagnetic (AFM) interaction is the prototypical example of the frustrated magnetism. The frustration in the system can be understood within the framework of Ising model, and one can show that if all the spins are interacting through AFM interaction, then spins on all the vertices of a triangle can not be simultaneously anti-parallel. For a system of 3 spins, there are a total six configurations with a minimum energy and for each of these configurations there is one frustrated bond as shown in Fig. 1.1. The degeneracy in the gs of this system increases with the increase of the system size. This kind of frustration is called geometrical frustration. The frustration can also be induced through the interaction e.g., $J_1 - J_2$ model system which is shown in Fig. 1.2. In this system J_1 and J_2 are the nearest neighbor (NN) and next nearest neighbor (NNN) interaction strength, respectively, and if J_1 is AFM then the system is frustrated irrespective of the sign of J_2. These systems show many interesting phases like spin liquid, dimer, spiral phase etc. [10–14].

In this section, a brief overview of model Hamiltonian in the LD systems is presented at first, and then the frustrated quantum spin system in the absence and presence of the magnetic field h is reviewed in the next section.

1.2 Interacting Model Hamiltonian in the Low Dimension

A solid is composed of atoms and these atoms are bonded together through various kinds of interactions. In a metallic solid, atoms share electrons and their atomic orbitals are hybridized with the orbitals of the neighboring atomic orbitals. These shared electrons interact with each other through the coulomb interaction. The nuclear degree of freedom can be ignored as the time scale of nuclear dynamics is much larger than electrons. A general many-body electronic Hamiltonian for a solid can be written as

$$H = \sum_{<ij>,\sigma} t_{ij}(a^{\dagger}_{i,\sigma}a_{j,\sigma} + h.c) + \sum_{ijkl}\sum_{\sigma,\sigma'} V_{ijkl}\, a^{\dagger}_{i,\sigma}a^{\dagger}_{j,\sigma'}a_{l,\sigma'}a_{k,\sigma}. \tag{1.1}$$

In Eq. 1.1, t_{ij} is the hopping matrix element of an electron between two orbitals i and j. $a_{i,\sigma}$ annihilates and $a^{\dagger}_{i,\sigma}$ creates an electron with spin $\sigma(\uparrow)$ or $\sigma'(\downarrow)$ on the ith orbital. V_{ijkl} represents coulomb repulsion of electron. The terms t_{ij} and V_{ijkl} are given by,

$$t_{ij} = \int d^3\vec{r}\,\phi^*_i(\vec{r})(-\frac{\hbar^2}{2m}\nabla^2)\phi_j(\vec{r}), \tag{1.2}$$

$$V_{ijkl} = \frac{1}{2}\int d^3\vec{r}_1 \int d^3\vec{r}_2\, \phi^*_i(\vec{r}_1)\phi_j(\vec{r}_1)V(\vec{r}_1 - \vec{r}_2)\phi^*_k(\vec{r}_2)\phi_l(\vec{r}_2), \tag{1.3}$$

where $V(\vec{r}_1 - \vec{r}_2) = \frac{e^2}{r_{12}}$ and subscripts i, j, k, and l have been used to index orbitals while the index 1 and 2 corresponds to the electron coordinate. In the limit of zero differential overlap case, most of the interaction integral vanishes and only the charge density confined at one orbital interacts with the charge on the other orbital. Therefore, we can safely write $V(i, j, k, l) = V(i, i, k, k)\delta_{ij}\delta_{kl}$.

The Hamiltonian in Eq. 1.1 can be simplified further, based on the following assumptions: (i) there is only one orbital per each site, (ii) hopping matrix elements on on-site and NN sites are non-zero only, ($t_{ii} = \epsilon_i$ and $t_{ij} = t$ if $j = i\pm1$), (iii) V_{ijkl} integral is non-zero for $i = j = k = l$ i.e., V_{iiii} which is usually denoted as U known as Hubbard parameter, same for all sites in the system. This approximation is valid in a case where screening of coulomb interaction is very high. Therefore, the Hamiltonian in Eq. 1.1 can be written as

$$H = t\sum_{i=1}^{N}\sum_{\sigma}(a^{\dagger}_{i,\sigma}a_{i+1,\sigma} + h.c) + \sum_{i=1}^{N}\epsilon_i n_i + U\sum_{i=1}^{N} n_{i,\sigma}n_{i,\sigma'}, \tag{1.4}$$

where $n_{i,\sigma}$ and $n_{i,\sigma'}$ are number operators with spin σ and σ', and $n_i = (n_{i,\sigma}+n_{i,\sigma'})$ is the total number operator for site i. In the limit, $U = 0$ or $t = 0$ the Hubbard model is exactly solvable. The non-interacting limit i.e., $U = 0$ corresponds to the band theory in the tight-binding approximation, while the $t = 0$ limit corresponds to the atomic limit. The effective Hubbard U can be either attractive ($U < 0$) or repulsive ($U > 0$). The repulsive single-band Hubbard model was proposed independently in 1963 by Kanamori [15], Gutzwiller [16], and Hubbard [17] to study the problem of itinerant electron ferromagnetism in transition metals. This model looks a very simple model, but it is a highly non-trivial problem of electron correlations, and it also takes care of short-range electron correlation effect. The positive U has been used in many contexts to understand the metal to Mott insulator transition [18], whereas the attractive Hubbard model ($U < 0$) claimed to have explained the superconductivity in the system [19].

In the large U limit i.e., $U/t \to \infty$, a half-filled Hubbard model system can be mapped to an isotropic Heisenberg spin-1/2 model by using the perturbation theory. In this limit the charge degrees of freedom are frozen, and each lattice site is occupied by a single unpaired electron. Therefore, at every site there are two possible degrees of freedom either spin up or spin down. In this case, electron can not move, but it can still exchange its spin. Treating the hopping term as a perturbation in the strong electron-electron interaction limit, and if we consider the leading terms only up to second order, then the spin Hamiltonian can be mapped to an isotropic Heisenberg model which can be written as

$$H = \sum_{<ij>} J_{ij}\vec{S}_i \cdot \vec{S}_j, \tag{1.5}$$

where $\vec{S}_i$ and $\vec{S}_j$ are the spin operator localized at site i and j. The single bracket holds for only NN and J_{ij} represents exchange interaction strength between sites i and j. Depending on the various kind of interaction strengths system can form various lattices such as a linear chain, the square lattice, and the cubic lattice etc. There are other lattice structures such as ladder which are the interpolation structure between a linear chain and the square lattice. But in this thesis, our main focus is on the 1D and quasi-1D spin chain. The spin $\vec{S}_i$ is a vector quantity in Eq. 1.5 and it is 3D in nature. Depending on the strength of interaction in various spatial direction, it can be either an isotropic i.e., interaction strength in all three spatial directions are same, or anisotropic where different directions have different interaction strengths. The most general Hamiltonian can be written as

$$H = \sum_{<ij>} J_{ij}^{\alpha,\beta} S_i^{\alpha} \cdot S_j^{\beta}, \tag{1.6}$$

where $J_{ij}^{\alpha,\beta}$ is anisotropic exchange interaction and $\alpha/\beta = x, y$ or z. For Ising model, exchange interactions are $J_{ij}^{x,x} = J_{ij}^{y,y} = 0$ and $J_{ij}^{z,z} \neq 0$. If the exchange interactions along x and y-direction are same, and the interaction along the z-axis vanishes then the model is called XY model and can be written as

$$H_{XY} = \sum_{<ij>} J_{ij}[S_i^x S_j^x + S_i^y S_j^y]. \tag{1.7}$$

The model in Eq. 1.5 is isotropic if the interaction strength $J_{ij}^{x,x} = J_{ij}^{y,y} = J_{ij}^{z,z} = J$ then the Hamiltonian in Eq. 1.5 can be written as

$$H = J \sum_{<ij>} \vec{S}_i \cdot \vec{S}_j. \tag{1.8}$$

The sign of the exchange interaction strength determines alignment of the spins. For $J < 0$ the interaction of the spin is ferromagnetic (FM), and for $J > 0$ spins are aligned anti-ferromagnetically. Now let us examine the effect of exchange interaction on the magnetic ordering of the system one can consider large spins as classical vector spin. The interaction energy of the model Hamiltonian in Eq. 1.8 can be given as $JS^2\cos\theta$, where θ is the angle between spins. For $J < 0$ the energy minima occurs for a configuration with $\theta = 0$ i.e., the gs is FM where all the NN spins are parallel. Whereas, for $J > 0$, the minimum energy configuration is at $\theta = \pi$ i.e., the AFM gs where NN spins are anti-parallel.

The magnetism is a purely quantum mechanical phenomenon, therefore, the Hamiltonian should be treated quantum mechanically rather than classically. The Hamiltonian for a spin-1/2 system, in Eq. 1.8, can be written in second quantized notation as

$$H = J \sum_{i=1}^{N} [\frac{1}{2}(S_i^+ S_{i+1}^- + S_i^- S_{i+1}^+) + S_i^z S_{i+1}^z], \tag{1.9}$$

where $S_i^+ = S_i^x + iS_i^y$ and $S_i^- = S_i^x - iS_i^y$ are the spin raising and spin lowering operators, respectively. In the case of FM gs, the energy is same for the classical and the quantum mechanical gs, but in the case of AFM gs or Néel state the quantum fluctuation is quite significant and the classical gs is quite different from the quantum gs. The solving of quantum mechanical problem is quite difficult as the degrees of freedom increases as 2^N where N is the number of sites.

Now let us represent the Eq. 1.6 with $\alpha = \beta$, also known as XYZ model [20] where the interaction strength along x, y, and z direction is different and it can be written as

$$H = \sum_{i=1}^{N} [J_x \, S_i^x S_{i+1}^x + J_y \, S_i^y S_{i+1}^y + J_z \, S_i^z S_{i+1}^z]. \tag{1.10}$$

This model is very important as it takes care of various kinds of anisotropy in the system and can explain any real material with only spin degrees of freedom. Other models are an approximation of this model and in various limits this can be reduced to the Ising model for $J_x = J_y = 0$, XY model (Eq. 1.7) for $J_z = 0$, to an isotropic Heisenberg model or XXX model for $J_x = J_y = J_z$, or to an anisotropic Heisenberg model like XXZ model for $J_x = J_y \neq J_z$. These models for a 1D system are studied extensively in the literature. Now let us consider the XXZ model Hamiltonian which is written as

$$H = J \sum_{i=1}^{N} [S_i^x S_{i+1}^x + S_i^y S_{i+1}^y + \gamma \, S_i^z S_{i+1}^z]. \tag{1.11}$$

In the limit of $\gamma = 1$ and $J < 0$ the system preserves the full rotational symmetry and shows an isotropic FM behavior [21]. The gs wavefunction does not change when an external magnetic field h is applied, but it results in an additional energy contribution hS^z_{tot} to the system. The external magnetic field h along the z-direction lifts the $(2S + 1)$ fold degeneracy in the gs of a system with total spin S [21]. In the FM phase the lowest-lying excited states are one magnon excitation, and it is gapped at momentum $q \to 0$ for $J < 0$ and $\gamma > 1$. The excitation spectrum is gapless for $\gamma = 1$ and $J > 0$ and the gs show continuous symmetry breaking. In this system the Mermin and Wagner theorem holds as it shows a quasi-long-range-order (QLRO) in the gs, and exponential decaying correlation at finite temperature [22].

In the Ising anisotropy limit, $J > 0$ and $\gamma > 1$, the gs is in the AFM phase and has finite sublattice magnetization and long-range-order (LRO) in the spin-spin correlation function. However, quantum fluctuations prevent the LRO as the sublattice magnetization coexist [22]. The gs is a doubly degenerate Néel phase. The lowest elementary excitations can be induced by spin-flip from one of the two Néel states [3].

When $\gamma = 0$ the model in Eq. 1.11 reduces to the isotropic XY model. The anisotropic XY model is one where x and y component of exchange interactions have unequal weights. This model is interesting because the exact solution can be found by both Bethe ansatz and by mapping this model to a non-interacting spin-less fermion model using Jordan-Wigner transformation [23, 24].

For $\gamma = 1$, the model in Eq. 1.11 becomes the isotropic Heisenberg model. For $J < 0$ the gs is a FM state, whereas, for $J > 0$ it is AFM. The exact gs energy in the FM phase is proportional to the product of z component of all the spins. Whereas, the AFM model is exactly solved by Bethe [2] and the exact gs energy for N site system is

$$E_{gs} = \frac{NJ}{4} - JN \ln 2. \tag{1.12}$$

The low-lying excitation spectrum calculated by des Cloizeaux and Pearson [25] is

$$\epsilon = \frac{\pi}{2} J |\sin k|, \tag{1.13}$$

where

$$k = \frac{2\pi m}{N}; \qquad m = 0, \pm 1, \pm 2, ...N/2. \tag{1.14}$$

Faddeev and Takhtajan [26] calculated the low-lying spectrum more rigorously. The energy of the low-lying excited states can be written as

$$E(k_1, k_2) = \epsilon(k_1) + \epsilon(k_2). \tag{1.15}$$

For a fixed momentum k one gets continuum of scattering states. The lower bound of the continuum is given by des Cloizeaux and Pearson [25]. The upper bound is obtained for $k_1 = k_2 = k/2$

$$\epsilon_k^U = \pi J \left| \sin \frac{k}{2} \right|. \tag{1.16}$$

The low-lying excitation spectrum for a $S = 1/2$ HAF model is spinon which is a $S = 1/2$ object, and the combination of two spinons give rise to $S = 1$ and $S = 0$ states. In the Heisenberg model, the spinons are only non-interacting in the thermodynamic limit.

1.3 Frustrated Model Hamiltonian

In the model Hamiltonian in Eq. 1.8, we have restricted our spin exchange interaction to NN only, but there are many systems where spin interactions extend to NNN. This model is generally called $J_1 - J_2$ model [27, 28]. The Hamiltonian can be written as

$$H(J_1, J_2) = J_1 \sum_r \vec{S}_r \cdot \vec{S}_{r+1} + J_2 \sum_r \vec{S}_r \cdot \vec{S}_{r+2}. \tag{1.17}$$

The above model with isotropic exchange J_1 and J_2, between first and second neighbors, respectively, is the prototypical example of a frustrated spin-1/2 chain. The parameter $\alpha = J_2/J_1$ quantifies the competition between first and second neighbor exchange interaction strength where the NN exchange interaction J_1 can be either AFM or FM. In $J_2 = 0, J_1 > 0$ limit, the model in Eq. 1.17 behaves like a linear Heisenberg antiferromagnetic (HAF) model which has gapless spectrum and shows a QLRO. However, for $J_1 = 0, J_2 > 0$ the system behaves like two independent HAF chains where one chain is made up of even sites and whereas the second chain is made up of odd sites of the full system. Sandvik [3] has reviewed the linear HAF chain and other related spin chains including $H(J_1, J_2)$ for $0 < \alpha < 1$. An earlier review by Lecheminant addresses frustrated quantum 1D systems mainly in terms of field theory for $0 < \alpha < 1$ [29].

The Hamiltonian in Eq. 1.17 with J_1 and J_2 AFM interactions for 1D spin-1/2 chain has been studied extensively [27–32]. This model shows a quantum phase transition from a gapless critical AFM phase to a gapped dimer phase at $\alpha_c = 0.2411$ shown by Okamoto and Nomura [32]. The exact gs of this model is known at $\alpha = 1/2$, and this model is known as the Majumdar-Ghosh model [27, 28] and this model has dimerized doubly degenerate gs which can be represented as products of singlet pairs. The doubly degenerate gs breaks the inversion symmetry through the sites. In this phase, the system has a finite energy gap E_m between the lowest singlet and triplet state. For $J_2/J_1 > 0.5$ the system goes to an incommensurate (IC) phase. However, its result at higher J_2 is still debatable.

The model in Eq. 1.17 with FM J_1 and AFM J_2 is also an example of the frustrated spin model. In this parameter space, gs goes from a FM to singlet gs at $|\alpha| = 0.25$. The gs is in the gapless FM phase with LRO for $|\alpha| \leqslant 0.25$. At the quantum critical point $|\alpha_c| = 0.25$, singlet and FM state are degenerate with the energy $E_{gs} = -\frac{3}{16}N|J_1|$ [33]. Hamada *et al.* showed that the singlet is the uniformly distributed resonating valence bond (RVB) state, and is degenerate with the FM gs of parallel spins at this critical point [33]. In this parameter space the dimer and IC phase coexist for $|\alpha| > 0.25$. However, in the large J_2 limit, the system behaves like two decoupled HAF chains [34].

The 1D spin-1/2 isotropic $J_1 - J_2$ model in the presence of an axial magnetic field h have been studied, but is not a well understood model. The Hamiltonian for the

$J_1 - J_2$ model in the axial magnetic field h is written as

$$H(J_1, J_2) = J_1 \sum_r \vec{S}_r \cdot \vec{S}_{r+1} + J_2 \sum_r \vec{S}_r \cdot \vec{S}_{r+2} - h \sum_r S^z_r. \tag{1.18}$$

The $J_1 - J_2$ model in Eq. 1.18 with J_1 and J_2 AFM interactions is studied extensively over several decades in the literature [35–45]. It exhibits various unconventional phases induced by frustration in the system. The quantum phase diagram in this parameter space is constructed by using the numerical results and bosonization analysis. These studies shows that the $J_1 - J_2$ model shows cusp singularities and a plateau at 1/3 of the saturated magnetization M_{sat} in the $M - h$ curve [36, 39–41]. The 1/3-plateau phase has a magnetic LRO of *up-up-down* structure. At large magnetic field h and $\alpha \geqslant 1$, two magnon bound state occurs. In the presence of h, the system shows a gapped dimer phase ($M = 0$), 1/3-plateau phase ($M = 1/6$), FM phase ($M = 1/2$) at saturation field h_s, TLL1, TLL2, vector chiral (VC), and spin density wave of type two (SDW$_2$) phase. Magnetization plateau and cusp singularities occur at $0.487 < \alpha \leqslant 1.25$ and $0.25 \leqslant \alpha \leqslant 0.7$, respectively, at intermediate magnetic field [36, 39–41]. The model also shows LRO of VC in the presence of anisotropic exchange couplings [46–48].

The frustrated $S = 1/2$ model with FM J_1 and AFM J_2 in the presence of an external magnetic field h are relatively new and have not been explored extensively. Since last decade there is sudden surge in studies of magnetic properties of this model. The model has attracted lots of attention because it is considered to explain many magnetic properties of recently synthesized edge-sharing chain cuprates. These compound includes $LiCuVO_4$ [5], $LiCuSbO_4$ [6], $Ba_3Cu_3Sc_4O_{12}$ [8] ,$Ba_3Cu_3In_4O_{12}$ [9] etc. Therefore, these compounds are suitable for studies of exotic phases induced by the quantum fluctuations, which are observed at low temperature. Some of these compounds e.g., $LiCu_2O_2$ shows multiferroic behavior below a critical temperature [7]. In this model the gs has FM phase with LRO for $|\alpha| < 0.25$ and gapped dimer phase coexisting with a spiral phase for $|\alpha| > 0.25$ [11, 12, 14, 49]. The dimer phase is gapped in nature, and the spin-spin correlation decays exponentially [10, 13, 31].

In the last decade, the $J_1 - J_2$ model with the FM J_1 has been studied extensively [50–54], but there is no agreement on the quantum phase diagram in the large α limit [34]. The quantum phase diagram of the model at the finite h is a zoo of the exotic quantum phases [50–54]. Using bosonization procedure, Chubukov has suggested a uniaxial dimerized and a biaxial spin nematic phase in the gs [50], where the rotational symmetry is broken about a site or about a bond, respectively [50]. Hikihara *et al.* used bosonization technique, ED and DMRG method to calculate the different phases in the presence of the axial magnetic field h. The VC and the multipolar phases are shown to exist in the presence of a finite magnetic field h [51, 52]. Sudan *et al.* also showed the presence of the VC and the multipolar phases using the ED. The square of the VC order parameter and the structure factor are used to construct the quantum phase diagram [53]. In the earlier works, the quantum phase diagrams are constructed based on correlation functions, especially the VC phase [53, 54], where the square of the order parameter and its related correlation functions are calculated.

The VC phase is an interesting phase with spontaneously broken spin parity and inversion symmetries. The phase boundary of these exotic phases such as VC and multipolar phases are calculated based on the order parameters, energy level crossings, and steps in the magnetization in the system. The order parameter of the VC phase is calculated using broken symmetry state at the finite magnetic field. In the presence of a magnetic field, the spin parity symmetry is broken. Therefore, non-zero value of VC order parameter exist only if gs has the broken inversion and spin parity symmetry. This kind of state can be created by taking the linear combination of degenerate states. These degeneracies exist even in the finite system [55]. The ED and DMRG results are used to show that the VC phase exists only in a narrow range of parameter space J_2/J_1. In the quadrupolar phase the magnetization steps can be associated with the binding energy of two magnons localized at two different legs of the zigzag chain. The energy level crossings and degeneracies in the presence of magnetic field h are studied in detail using ED method. The VC phase has been studied extensively because of its potential application in improper multiferroic systems [56, 57].

Moreover, the frustrated $J_1 - J_2$ model in Eq. 1.18 with NN FM and NNN AFM interaction for spin-1/2 and spin-1 chains are studied in the presence of magnetic field h. Hikihara *et al.* suggest existence of metamagnetic or spin multipolar phase in the presence of the high axial magnetic field h for FM J_1 [52]. The order parameters of these multipolar phases are hidden in nature so these can not be probed directly. The number of paired magnons p of these multipoles depend on the exchange coupling ratio α [52, 53]. These multipolar phases are of different types such as dipolar ($p = 1$), quadrupolar ($p = 2$), octupolar ($p = 3$) and hexadecapolar ($p = 4$) phases etc. Existence of the multipolar phases of odrer $p > 4$ for this model near the quantum critical point $|\alpha_c| = 0.25$ is either not well understood or has been controversial. In this model, there are many unsettled issues such as the metamagnetic phase in the small α regime has been completely unexplored, and is difficult to characterize because of small gaps.

The quadrupolar phase is a Tomonaga-Luttinger (TL) liquid of hard core bosons [52], and each boson is made up of two magnons. In this phase, the correlations between bosons and density fluctuations follow a power law. However, the boson propagator is dominant over the density fluctuations in this phase [52]. In the seminal work of Chubukov he has predicted that this phase has dimerized (gs) [50], but Hikihara *et al.* showed the absence of dimerization [52]. In the large α regime, field theoretical calculations show that the SDW_2 phase exists in low magnetic field, whereas spin nematic (SN) phase exists in the narrow range of magnetic field near the saturation field [52]. The order parameter in the multipolar phases is probed indirectly by inelastic neutron scattering (INS) [6, 58] and the resonant inelastic X-Ray scattering (RIXS) [59, 60] experiments. The nematic phase in a real material $\mathrm{LiCuVO_4}$ is confirmed by using the INS data of dynamical structure factor [58], and NMR data of this compound shows a sharp single and solitary line which moves with magnetic field [61, 62].

The existence of quadrupolar phase in spin-1 systems is controversial, as steps of two i.e. $\Delta S^z = 2$ in the magnetization-magnetic field $M - h$ curve is absent [63, 64], whereas the other studies for general spin show the existence of this phase.

Now let us discuss the probing of the multipolar phases by using the dynamical probes like inelastic neutron scattering etc.

1.4 Theory of Neutron Scattering

Neutron scattering is a powerful technique for the determination of microscopic properties of magnetic materials. It measures the spin-spin correlation functions, and gives the information about geometrical arrangements of spins. The probe can even differentiate between a paramagnet and an ordered FM phase based on the above information. Energy of neutron is comparable to the low energy magnetic excitations, therefore, this can be probe to study the dynamics of the elementary excitations such as magnons, spinons etc. The higher energy excitations can also be probed by neutron scattering experiment, however, these excitations have very weak signal. As neutron is chargeless, it can penetrate deep into the sample and provide information about the bulk properties. Neutron has a very low magnetic moment which enables it to interact with unpaired electrons of the magnetic atom resulting in the scattering of neutron. This allows to obtain information about the magnetic structure and spin dynamics of magnetic materials.

In the scattering experiment, one measures and analyzes the incident and outgoing neutron beams and gives us information about energy and momentum transferred to/from the sample [65, 66]. In the scattering experiment, the laws of energy and momentum conservation is satisfied i.e., if the momentum and the energy of the incident/outgoing neutron is $\hbar\vec{k}_i/\hbar\vec{k}_f$ and $\hbar\omega_i/\hbar\omega_f$, the following condition is satisfied

$$\hbar\vec{Q} = \hbar\vec{k}_i - \hbar\vec{k}_f \quad \text{and} \quad \Delta E = \hbar\omega_i - \hbar\omega_f. \tag{1.19}$$

Based on the conservation laws, the neutron scattering is of two kinds, the elastic and the inelastic neutron scattering [65, 66]. In elastic neutron scattering, the total energy and momentum is conserved i.e., $|E_i| = |E_f|$ and $|\vec{k}_i| = |\vec{k}_f|$. In this case the angle of incidence is equal to the angle of scattering, and $\hbar\vec{Q}$ is normal to the set of crystal planes. The Bragg's condition is satisfied when $|\vec{Q}| = |\vec{G}|$ where $\vec{G}$ is the reciprocal lattice vector. Thus the elastic neutron scattering experiment provides the magnetic structure of the sample. Another interesting and a more complicated type of scattering is the inelastic neutron scattering (INS). In this case the kinetic energy and momentum of the incident particle is not conserved because some fraction of the energy of the incident particle is transferred energy and momentum to/from the sample. In a sample with single crystal, energies become dependent on the relative momentum $\hbar\vec{q}$ which is measured with respect to the reciprocal lattice vector, and the momentum transfer to the sample can be written as $\vec{Q} = \vec{G} + \vec{q}$. In the INS experiment a constant $\hbar\vec{q}$ measurement is performed by varying the scattering angle [65, 66].

Let us consider a neutron beam, characterized by the wave vector $\vec{k}_i$ and the flux $\phi(\vec{k}_i)$, incident on a sample. The rate of neutron scattering by the sample is given by the product $\phi(\vec{k}_i)\sigma$, where σ is the scattering cross section. In a neutron scattering experiment, the rate at which neutrons are scattered in a given solid angle $d\Omega_f$ in the direction of the wave vector $\vec{k}_f$ and in the energy range between E_f and $E_f + dE_f$, is given by the product of $\phi(\vec{k}_i)$ and the double-differential cross section $\frac{d^2\sigma}{d\Omega_f dE_f}$. The differential cross section is the sum of two parts, coherent and incoherent i.e., $\frac{d^2\sigma}{d\Omega_f dE_f} = (\frac{d^2\sigma}{d\Omega_f dE_f})_{coh} + (\frac{d^2\sigma}{d\Omega_f dE_f})_{incoh}$. The coherent part gives information about the cooperative effects among different atoms, such as elastic Bragg scattering or inelastic scattering by phonons or magnons, whereas the incoherent part is proportional to the time auto-correlation of an atom, and provides information of the motion of an individual particle. This part gives information about the short range ordered phase. The neutrons act as a weak perturbation, therefore, it does not modify the states within the systems. The scattering cross-section can be obtained from the Fermi-Golden rule and can be written as [65, 66],

$$\frac{d^2\sigma}{d\Omega_f dE_f} = N\frac{k_f}{k_i}b^2 S(\vec{q},\omega), \tag{1.20}$$

where $S(\vec{q},\omega)$ is the dynamical structure factor (DSF) and b is the nuclear scattering length. The aim of neutron scattering is to obtain the information about the spins spatial distribution and also explain the low energy excitation. The dynamical structure factor $S(\vec{q},\omega)$ is given as a function of excitation momentum q and energy ω. The momentum can be connected to the pitch angle between the neighboring spins in the magnetic system.

1.5 Resonant Inelastic Neutron Scattering

Resonant inelastic x-ray scattering (RIXS) is a fast developing experimental technique to probe the low energy excitation in the magnetic system. In this probe x-ray photons are scattered inelastically from the sample and measure the change in energy, momentum, and polarization of the scattered photon which are transferred to intrinsic excitations of the material. Thus RIXS gives information about low-lying excitations and works on the principal of resonant energy technique [59, 60]. In this probe the energy of the incident photon is chosen such that excitation coincides and hence resonates with absorption edges of the material such as a K edge for exciting 1s ($n = 1$) core electrons, an L edge for electrons in the $n = 2$ shell, or an M edge for electrons in $n = 3$ shell. Due to the resonance, the inelastic scattering cross section is enhanced by many orders of magnitude, and helps to detect the weak signal of excitations caused by the perturbation in magnetic, charge, and orbital degrees of freedom in a crystal. In neutron scattering, excitations always carry integer spin, so that pairwise creation of spinons are probed through the INS experiment. The INS amplitude is determined by the single spin dynamical structure factor (DSF) [67], whereas the corresponding scattering amplitude is given by two spin DSF also known as spin exchange DSF [59, 60]. In chapter 6, both the probes will be explained in detail.

1.6 Outline of the Thesis

The thesis is organized in the following way:

Chapter 2 describe the numerical methods i.e., exact diagonalization and density matrix renormalization group methods. These two numerical methods are used to solve all the problems in this thesis.

In **chapter 3**, we focus on the numerical study of incommensurate and decoupled phases of spin-1/2 chains with isotropic exchange J_1, J_2 between first and second neighbors in the absence of the magnetic field h. The decoupled phase is characterised based on the level crossing of excited states and extrapolated to the thermodynamic limit, divergence of structure factor peak, and jump in spin densities in lowest triplet state in the absence of a magnetic field. The quantum phase diagram is constructed in the $J_1 - J_2$ plane with $J_1 > 0$ and $J_1 < 0$ sector by keeping $J_2(> 0)$ fixed. This chapter is based on our published paper in J. Phys.: Condens. Matter **27**, 316001 (7pp) (2015) and J. Phys.: Condens. Matter **28**, 175603 (12pp) (2016).

Chapter 4 reports degeneracies and level crossings in an isotropic frustrated spin-1/2 chain with FM NN and AFM NN in the presence of the external magnetic field. These degenerate states are used to characterize the VC and multipolar phases. In the large α limit, zigzag nature of the spin chain is responsible for the quadrupolar phase. The boundary of these exotic phases are calculated based on the level crossings and steps in the magnetization vs. magnetic field $M - h$ plot. The work related to this chapter has been published in J. Mag. Mag. Mat. **401**, 96-101 (2016).

The existence of different phases for the $J_1 - J_2$ model with FM NN and AFM NNN in an axial magnetic field h is either not understood in detail or has been controversial yet. In **chapter 5**, we show the existence of higher order $p > 4$ multipolar phases near the critical point $|\alpha_c| = 0.25$. The criteria to detect the quadrupolar or SN/SDW$_2$ phase are discussed. We also discuss the dimerized and degenerate ground state in the quadrupolar phase. We also show that the major contribution of binding energy in the spin-1/2 system comes from the longitudinal component of the NN bonds. We also discuss SN/SDW$_2$ phase in spin-1 system in large α limit. The work related to this chapter has been published in Phys. Rev. B **96**, 054413 (2017).

Chapter 6 describes the dynamical properties of multipolar phases in the $J_1 - J_2$ model in the presence of magnetic field h. The characterization of quadrupolar or SN/SDW$_2$ phase using the experimental INS result is discussed, and experimental INS results of LiCuVO$_4$ and LiCuSbO$_4$ compound is modeled in the limit of $J_1 - J_2$ model.

In **chapter 7**, conclusions of our all the investigations of this thesis are summed up and some future outlook is provided.

Bibliography

[1] E. Ising, Z. Phys. **31**, 253258 (1925).

[2] H. Bethe, Z. Phys. **71**, 205 (1931).

[3] A. W. Sandvik, AIP Conf. Proc. **1297**, 135 (2010) and references therein.

[4] E. Dagotto and T. M. Rice, Science **271**, 618-623 (1996).

[5] M. Enderle, C. Mukherjee, B. Fåk, R. K. Kremer, J. -M. Broto, H. Rosner, S. -L. Drechsler, J. Richter, J. Málek, A. Prokofiev, W. Assmus, S. Pujol, J. -L. Raggazzoni, H. Rakoto, M. Rheinstadter, and H. M. Rønnow, Eur. Phys. Lett. **70**, 237243 (2005).

[6] S. E. Dutton, M. Kumar, M. Mourigal, Z. G. Soos, J. -J. Wen, C. L. Broholm, N. H. Andersen, Q. Huang, M. Zbiri, R. Toft-Petersen, and R. J. Cava, Phys. Rev. Lett. **108**, 187206 (2012).

[7] S. Park, Y. J. Choi, C. L. Zhang, and S. W Cheong, Phys. Rev. Lett. **98**, 057601 (2007).

[8] O. S. Volkova, I. S. Maslova, R. Klingeler, M. Abdel-Hafiez, Y. C. Arango, A. U. B. Wolter, V. Kataev, B. Büchner, A. N. Vasiliev, Phys. Rev. B **85**, 104420 (2012).

[9] S. E Dutton, M. Kumar, Z. G Soos, C. L Broholm, R. J Cava, J. Phys.: Condens. Matter **24**, 166001 (2012); M. Kumar, S. E Dutton, R. J Cava, Z. G Soos, J. Phys.: Condens. Matter **25**, 136004 (2013).

[10] C. Itoi and S. Qin, Phys. Rev. B **63** 224423 (2001).

[11] S. Mahdavifar, J. Phys.: Condens. Matter **20**, 335230 (2008).

[12] J. Sirker, Phys. Rev. B **81**, 014419 (2010).

[13] M. Kumar, S. Ramasesha, and Z. G. Soos, Phys. Rev. B **81**, 054413 (2010).

[14] M. Kumar and Z. G. Soos, Phys. Rev. B **85**, 144415 (2012).

[15] J. Kanamori, Prog. Theor. Phys. **30**, 275 (1963).

[16] M. C. Gutzwiller, Phys. Rev. Lett. **10**, 159 (1963).

[17] J. Hubbard, Proc. R. Soc. **A276**, 238-257 (1963); Proc. R. Soc. **A277**, 237 (1946).

[18] N. F. Mott, *Metal Insulator Transitions*, (Taylor & Francis Ltd., London, 1974).

[19] R. Micnas, J. Ranninger, and S. Robaszkiewicz, Rev. Mod. Phys. **62**, 113 (1990); E. Dagotto Rev. Mod. Phys. **66**, 763 (1994).

[20] F. Pinheiro, G. M. Bruun, J. -P. Martikainen, and J. Larson, Phys. Rev. Lett. **111**, 205302 (2013).

[21] U. Schollwöck, J. Richter, D. J. J. Farnell, R. E Bishop (Eds.), *Quantum Magnetism*, chapter1, Lect. Notes Phys. 645 (Springer, Berlin Heidelberg 2004).

[22] N. D. Mermin and H. Wagner, Phys. Rev. Lett. **17**, 1133 (1966).

[23] P. Jordan and E. Wigner: Z. Phys. **47**, 631 (1928).

[24] E. Lieb, T. D. Schultz, and D. C. Mattis, Ann. Phys. **16**, 407 (1961).

[25] J. des Cloizeaux and J. J. Pearson, Phys. Rev. **128**, 2131 (1962).

[26] L. D. Faddeev and L. A. Takhtajan, Phys. Lett. A **85**, 375-377 (1981).

[27] C. K. Majumdar and D. K. Ghosh, J. Math. Phys. **10**, 1388 (1969).

[28] C. K. Majumdar and D. K. Ghosh, J. Math. Phys. **10** 1399 (1969).

[29] P. Lecheminant, *Frustrated Spin Systems*, Ed. by H. T. Diep, chapter 6, page 307 (Singapore: World Scientific 2004).

[30] F. D. M. Haldane, Phys. Rev. B **25**, 4925 (1982).

[31] S. R. White and I. Affleck, Phys. Rev. B **54**, 9862 (1996).

[32] K. Okamoto and K. Nomura, Phys. Lett. A **169**, 433 (1992).

[33] T. Hamada, J. Kane, S. Nakagawa, and Y. Natsume, J. Phys. Soc. Japan. **57**, 1891 (1988).

[34] M. Kumar, A. Parvej, and Z. G. Soos J. Phys.: Condens. Matter **27**, 316001 (7pp) (2015).

[35] T. Tonegawa and I. Harada, Physica B **155**, 379 (1989).

[36] T. Tonegawa, K. Okamoto, K. Okunishi, K. Nomura, and M. Kaburagi, Physica B **346-347**, 50 (2004).

[37] M. Schmidt, C. Gerhardt, K. -H. Mutter̈, and M. Karbach, J. Phys.: Condens. Matter. **8**, 553 (1996).

[38] D. C. Cabra, A. Honecker, and P. Pujol, Eur. Phys. J. B **13**, 55 (2000).

[39] K. Okunishi, Y. Hieida, and Y. Akutsu, Phys. Rev. B **60**, R6953 (1999).

[40] K. Okunishi and T. Tonegawa, J. Phys. Soc. Jpn. **72**, 479 (2003).

[41] K. Okunishi and T. Tonegawa, Phys. Rev. B **68**, 224422 (2003).

[42] K. Okunishi, J. Phys. Soc. Jpn. **77**, 114004 (2008).

[43] N. Maeshima and K. Okunishi, Phys. Rev. B **62**, 934 (2000).

[44] T. Hikihara, T. Momoi, A. Furusaki, and H. Kawamura, Phys. Rev. B **81**, 224433 (2010).

[45] I. P. McCulloch, R. Kube, M. Kurz, A. Kleine, U. Schollwöck, and A. K. Kolezhuk, Phys. Rev. B **77**, 094404 (2008).

[46] A. A. Nersesyan, A. O. Gogolin, and F. H. L. Essler, Phys. Rev. Lett. **81**, 910 (1998).

[47] M. Kaburagi, H. Kawamura, and T. Hikihara, J. Phys. Soc. Jpn. **68**, 3185 (1999).

[48] T. Hikihara, M. Kaburagi, and H. Kawamura, Phys. Rev. B **63**, 174430 (2001).

[49] D. V. Dmitriev and V. Ya. Krivnov, Phys. Rev. B **73**, 024402 (2006).

[50] A. V. Chubukov, Phys. Rev. B **44**, 4693 (1991).

[51] L. Kecke, T. Momoi, and A. Furusaki, Phys. Rev. B **76**, 060407R (2007).

[52] T. Hikihara, L. Kecke, T. Momoi, and A. Furusaki, Phys. Rev. B **78**, 144404 (2008).

[53] J. Sudan, A. Lüscher, and A. M. Läuchli, Phys. Rev. B **80**, 140402(R) (2009).

[54] F. Heidrich-Meisner, I. P. McCulloch, and A. K. Kolezhuk, Phys. Rev. B **80**, 144417 (2009).

[55] A. Parvej and M. Kumar, J. Mag. Mag. Mater. **401**, 96-101 (2016).

[56] W. Eerenstein, N. D. Mathur, and J. F. Scott, Nature **442**, 759-765 (2006).

[57] H. Katsura, N. Nagaosa, and A. V. Balatsky, Phys. Rev. Lett. **95**, 057205 (2005).

[58] M. Enderle, B. Fåk, H. -J. Mikeska, R. K. Kremer, A. Prokofiev, and W. Assmus, Phys. Rev. Lett. **104**, 237207 (2010).

[59] A. Klauser, J. Mossel, J. -S. Caux, and J. van den Brink, Phys Rev. Lett. **106**, 157205 (2011).

[60] L. J. P. Ament, M. van Veenendaal, T. P. Devereaux, J. P. Hill, and J. van den Brink, Rev. Mod. Phys. **83**, 705 (2011).

[61] M. Sato, T. Momoi, and A. Furusaki, Phys. Rev. B **79**, 060406(R) (2009).

[62] M. Sato, T. Hikihara, and T. Momoi, Phys. Rev. B **83**, 064405 (2011).

[63] M. Arlego, F. Heidrich-Meisner, A. Honecker, G. Rossini, and T. Vekua, Phys. Rev. B **84**, 224409 (2011).

[64] A. K. Kolezhuk, F. Heidrich-Meisner, S. Greschner, and T. Vekua, Phys. Rev. B **85**, 064420 (2012).

[65] G. Shirane, S. M. Shapiro, and J. M. Tranquada, *Neutron Scattering with a Triple-Axis Spectrometer, Basic Techniques*, Chapters: 1, 2 (Cambridge University Press 2004).

[66] S. W. Lovesey, *Theory of Neutron Scattering from Condensed Matter*, Vol. 2, Chapter 9 (Oxford University Press, New York, 1984).

[67] B. Thielemann *et al.*, Phys. Rev. Lett. **102**, 107204 (2009).

Chapter 2

Numerical Methods

In the first chapter, we discussed that the quantum many-body effect in the real material is very relevant. There are only a few quantum many-body model systems which can be solved analytically, for example, for 1D Heisenberg model some of the low energy state can be solved analytically using the Bethe ansatz [1]. However, most of these model Hamiltonians can be solved by approximate methods which can be either analytical or numerical. The analytical methods are like spin wave analysis, [2] and field theoretical methods, e.g., bosonization [3], and renormalization group [4]. These methods are widely used for the study of quantum magnetism in LD. These approximate methods are limited to very few models. For complicated models, these approximate analytical methods are not reliable. In such scenario, the numerical methods have also been proved to be promising tools. Numerical methods can be categorized into two types e.g., exact numerical methods for finite systems and approximate numerical methods. Exact diagonalization numerical technique is limited to small system sizes, whereas, approximate numerical methods can be used for large system sizes. In some cases, approximate methods can be used to do the finite size scaling to understand the results in the thermodynamic limit. We first discuss the exact diagonalization numerical method, and then a brief introduction of the approximate numerical methods will be provided.

In fermionic quantum many-body systems each site can have four possible configurations: vacant, singly occupied with spin up, singly occupied with spin down and doubly occupied. The degrees of freedom of the system goes as 4^N for a system of size N. But in case of spin systems the charge degrees of freedom are frozen, and spin degrees of freedom goes as 2^N for N site system. In this thesis, model Hamiltonians discussed in chapter 1 are solved numerically. We have used two numerical techniques i.e., the exact diagonalization (ED) and the density matrix renormalization group (DMRG) method. At first, the ED method will be discussed in the next section, and then DMRG method will be discussed.

2.1 Exact Diagonalization Method

The properties of the model Hamiltonians can be obtained by the calculation of eigenvalues and eigenstates of the Hamiltonian. These eigenstates are obtained by setting up the Hamiltonian matrix in a preferred basis and then diagonalize it. In the ED method, one deals with the full Hilbert space of a finite system. The Hamiltonians discussed in Eq. 1.5 of chapter 1 commute with S and S^z i.e., $[H, S^2] = 0$ and $[H, S^z] = 0$. Therefore, if two operators commute with each other, then they will have a common set of eigenfunctions. The eigenvalues of H, S^2 and S^z are denoted by $E, S(S+1)$ and m_s, respectively. The commutation relation assures the conservation of the S and S^z, and matrix elements of the Hamiltonian in a fixed S^z is non-zero with different S. Therefore, the Hamiltonian matrix in a S^z basis is block diagonal for each conserved quantities of a system. The block

Table 2.1: Total number of basis states in different S^z sectors for a system of N spins

S^z	Total no. of basis state
0.0	${}^{N}C_{N/2}$
1.0	${}^{N}C_{N/2-1}$
2.0	${}^{N}C_{N/2-2}$
...	...
N/2	1

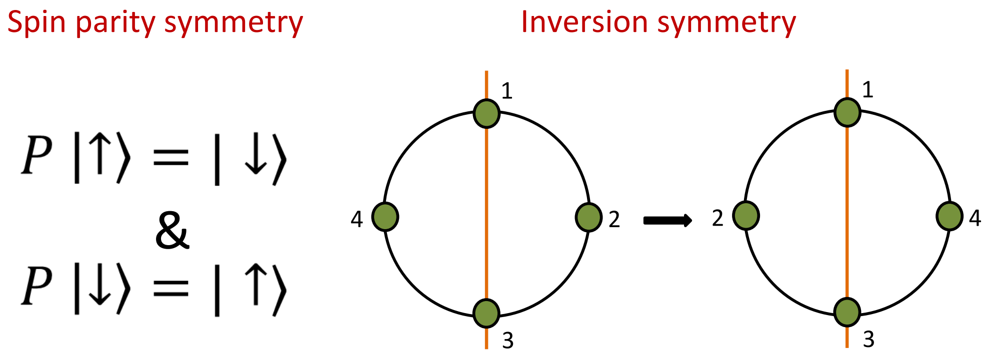

FIGURE 2.1: Spin parity symmetry flips the spin at each site whereas inversion symmetry rotates the system about an axis passes through the two sites.

diagonal properties of the Hamiltonian matrix help to reduce the computational cost of diagonalization of the Hamiltonian blocks. For representation of the spin-1/2 systems, the z-axis is chosen as quantization axis, and denote two possible spin directions i.e., spin up and spin down by 1 and 0 respectively. The x and y components of the spin operator i.e., S^x and S^y are expressed in terms of the spin raising S^+ and spin lowering S^- operators in the total Hamiltonian. The basis state forms an orthonormal set, therefore, the Hamiltonian matrix becomes symmetric in this basis. For a system of N spins, the total number of basis states in the different S^z sectors are shown in Table 2.1.

The gs properties of the frustrated magnetic model are non-trivial due to the large degeneracies in the low-lying states and these degeneracies lead to slow or non-convergence of the low-lying energy states. To get rid of this problem and also to separate out these degenerate states in different symmetry subspaces, the Hilbert space is divided into different symmetry subspaces. In the most of our model systems, spin-parity and inversion symmetry are preserved. The spin-parity operator corresponds to rotation of all the spins in a system around x or y-axis by an angle π which leaves the Hamiltonian invariant, which is valid only in $S^z = 0$ sector. The inversion symmetry corresponds to a rotation of all sites about an axis passing through two sites 1 and $N/2 + 1$ by an angle π, and this operation leaves the Hamiltonian invariant. This full operation is depicted in the Fig. 2.1. The Hamiltonian in different symmetry subspaces can be obtained by a rotation operation as $\tilde{H} = U^{\dagger} H U$ where U is a unitary symmetry operator of size $N \times m$. After rotation of Hilbert space, the dimension of the Hamiltonian $\tilde{H}$ is $m \times m$. The Hamiltonian matrix is represented in the basis states of total S and S^z. It is constructed in such way that it forms a sparse matrix and only the non-zero matrix elements are stored.

To calculate the expectation value of any observable, first, we need to calculate the eigenvalues and eigenvectors. However, even evaluating a few low-lying states of a matrix of order $10^6 - 10^7$ requires considerable computational efforts. There are many algorithms to find some low-lying states, and this can be done without full diagonalization of the Hamiltonian matrix. These algorithms are the Lanczos [6], modified Lanczos [7], and Davidson algorithms [8]. Davidson algorithm is one of the most celebrated algorithms for dealing with low-lying eigenstates of a large symmetric and sparse matrix [8]. In this thesis, we have used Retrup's algorithm which is a modification of the Davidson algorithm to a non-symmetric matrix. The brief outline of the Retrup's algorithm is given below [9].

Retrup's algorithm for a given large sparse Hamiltonian matrix H of order $N \times N$ starts with a set of m orthogonal vectors $\{\vec{Q}_i : i = 1, ..., m\}$. Using these vectors as the basis, we construct a small $m \times m$ matrix $h^{(m)}$ such that $h^{(m)}_{ij} = (\vec{Q}_i \mathbf{H} \vec{Q}_j)$. This small matrix is diagonalized using standard exact diagonalization routines. The eigenvectors $\vec{c}^{(m)}_k$ of $h^{(m)}$ are arranged in ascending order of eigenvalues $e^{(m)}_k$. The approximate eigenvectors for the large matrix are given by

$$\vec{C}^{(m)}_l = \sum_{i=1}^{m} \vec{c}^{(m)}_l(i) \vec{Q}_i, \tag{2.1}$$

where $\vec{c}^{(m)}_l(i)$ is the i^{th} component of the l^{th} eigenvector of the small matrix $h^{(m)}$. We construct i^{th} component of the vector $\vec{P}^{(m)}_l$ as

$$\vec{P}^{(m)}_l(i) = \frac{\vec{R}^{(m)}_l(i)}{e^{(m)}_l - H_{ii}}, \tag{2.2}$$

where $\vec{R}_l^{(m)}(i)$ is the i^{th} component of the residue vector for the l^{th} eigenvalue, and is defined as

$$\vec{R}_l^{(m)} = (\mathbf{H} - e_l^{(m)} I)\vec{C}_l^{m}. \tag{2.3}$$

The initial space is now augmented with a normalized vector $\vec{Q}_{m+1}$ which is obtained from Gram-Schmidt orthogonalization of P_l^m to the set of vectors $\{\vec{Q}_i : i = 1, ..., m\}$ i.e.,

$$\vec{Q}_{m+1} = \frac{\vec{Q}'_{m+1}}{||\vec{Q}'_{m+1}||}, \qquad \vec{Q}'_{m+1} = \vec{P}_l^{(m)} - \sum_{k=1}^{m} (\vec{P}_l^{(m)}, \vec{Q}_k)\vec{Q}_k. \tag{2.4}$$

The small matrix $h^{(m)}$ is now augmented to the matrix $h^{(m+1)}$ by adding new row and new column and the iteration is resumed. Next, we restart the procedure with $\{\vec{Q}_i : i = 1, ..., m\}$ replaced by $\{\vec{C}_i^{(l)} : i = 1, ..., m\}$ until the dimensionality of the small matrix $h^{(k)}$ exceeds a threshold value. The iteration is stopped when the desired eigenvalue converges within a chosen accuracy.

However, the computational cost to find the lowest state goes as N^2, therefore diagonalization of the Hamiltonian matrix for the large system is difficult with system size. Few low-lying states of a sparse matrix of dimension $10^7 \times 10^7$ can be obtained on a normal desktop. The ED for large systems and $N \geq 36$ for spin-1/2 systems are only possible after applying all symmetries and parallel computing. Therefore, the ED method is not suitable for large systems, and we rely on approximate techniques. There are many reliable approximate numerical techniques like the renormalization group (RG) method [4], Quantum Monte Carlo (QMC) method [5], and DMRG method for dealing with large system sizes. In this thesis, we have used the DMRG method extensively, therefore, we discuss this method in brief.

2.2 Density Matrix Renormalization Group Method

In 1975 renormalization group (RG) [4] method was developed and applied to the Kondo lattice by Wilson found great success, and it was a breakthrough development in the theoretical condensed matter physics. This development leads to a new tool to solve quantum many-body problems, and later this method was extended for solving the gs of the quantum many-body systems in real space [10]. Although the results of real space RG in the quantum systems are found to be quite inaccurate. White discussed the main reason for the failure of this method using the example of a particle in a box problem [11]. They argued that the direct product of the gs of two boxes of length L will not give the gs of a box of size $2L$. White [12] showed a new way to truncate the Hilbert state of the system block by keeping only the states with largest eigenvalues of the density matrix of the system block. These states are used to construct a new basis for the larger system. This new way of truncation of irrelevant degrees of freedom is known as DMRG method.

The DMRG method is based on the systematic truncation of irrelevant degrees of freedom i.e., truncation of the degrees of freedom is done at every step of the growing system. This is a state-of-the-art numerical technique to solve the quantum many-body problems in 1D [12–14]. The DMRG method is reviewed very frequently because of its potential application in quantum many-body systems in 1D and quasi-1D. This method can deal with large system sizes without compensating the accuracy of gs and calculate the wavefunction which can be used to calculate both static and dynamic properties of the model Hamiltonian. The DMRG method consists of two algorithms which are to be performed sequentially as: (a) First, the infinite DMRG algorithm where system is grown systematically and (b) Second, the finite DMRG algorithm which helps the superblock calculation to optimize the basis of relevant degrees of freedom. Fig. 2.2 gives a schematic picture of the infinite DMRG algorithm, and the procedure is explained below.

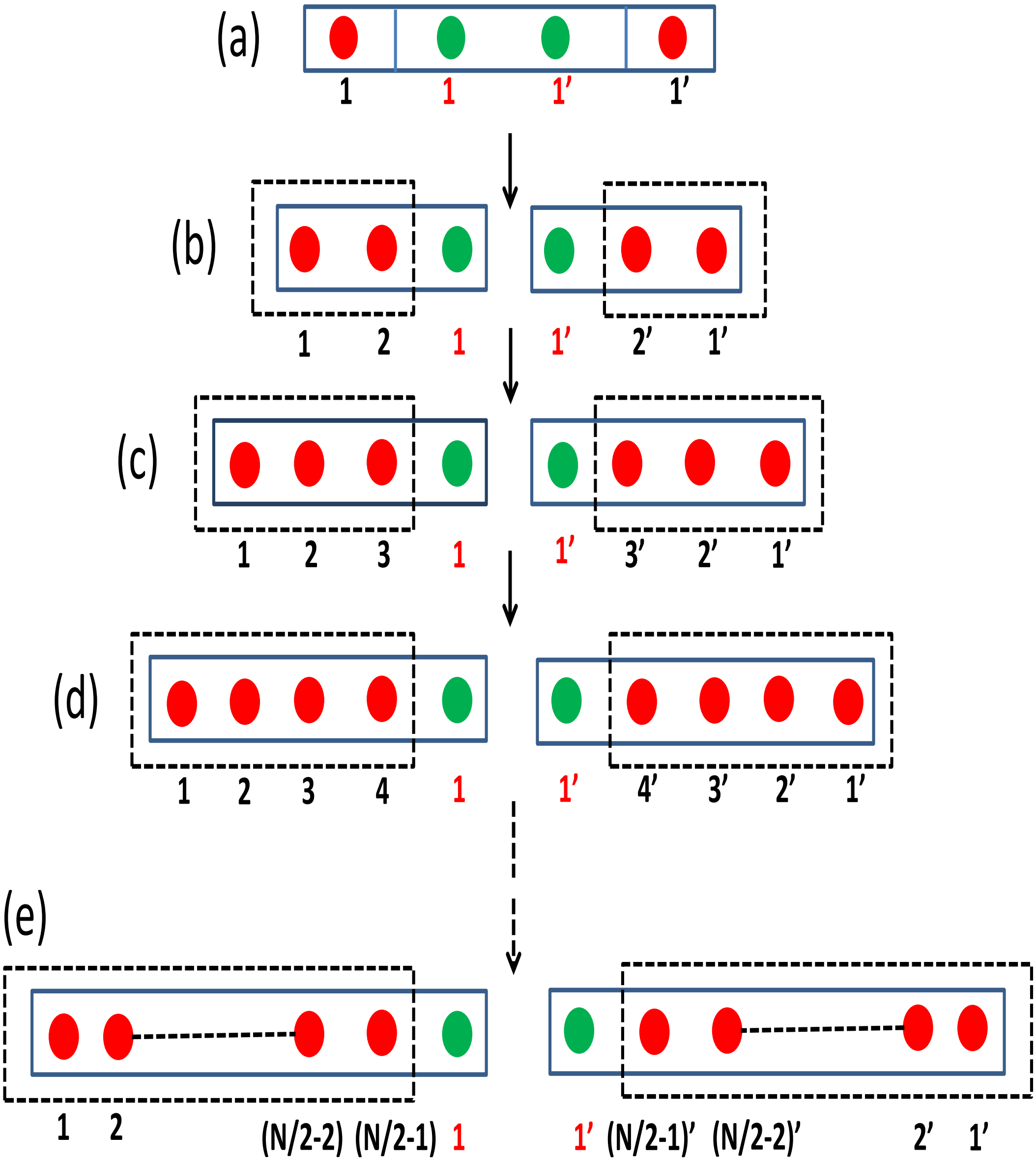

Figure 2.2: Schematic representation of the infinite DMRG algorithm procedure for a 1D chain. The filled red and green dots are old (numbering with black color) and new sites (numbering with red color), respectively. The black dashed boxes represent old system blocks (Left block) without new sites while, the solid blue boxes depict the new system blocks including new sites. The right side boxes are environment block.

As shown in Fig. 2.2, we start with a four site superblock which consists of a left and a right block where each block consists of one site, and two new sites. The system consists of first two sites from left block whereas last two sites in the right block are treated as the environment. Next, we calculate the gs eigenvector $|\psi\rangle$ and gs eigenvalue of the superblock, and expand the wavefunction $|\psi\rangle$ in the basis of the system and the environment block as

$$|\psi\rangle = \sum_{ij} C_{ij} |i\rangle |j\rangle . \tag{2.5}$$

Here $|i\rangle$ and $|j\rangle$ represents basis states of the system and the environment block, respectively. The matrix elements of the density matrix of the system block can be written as

$$\rho_{ij} = \sum_{k} C^*_{ik} C_{kj}, \tag{2.6}$$

where the sum is over the environment degrees of freedom. Let us assume that the dimension of the density matrix ρ is $M \times M$. The density matrix ρ is then diagonalized, and we keep the eigenvectors of the density matrix ρ corresponding to the largest m eigenvalues. Now let us construct a reduced density matrix ρ' of dimension $M \times m$ made up of m largest eigenvectors corresponding to m largest eigenvalues. The Hamiltonian and all the operators are now renormalized with reduced density matrix ρ' and renormalized Hamiltonian and operators can be represented in the truncated basis as

$$\tilde{H} = (\rho')^{\dagger} H \rho' \quad \text{and} \quad \tilde{O} = (\rho')^{\dagger} O \rho', \tag{2.7}$$

where $(\rho')^{\dagger}$ is the transpose of the reduced density matrix and $\tilde{H}$ and $\tilde{O}$ are effective Hamiltonian and operators, respectively, in the new system block.

The following steps illustrate the infinite DMRG algorithm for a 1D chain and these steps are represented pictorially in Fig 2.2

(a) Initially start with four sites, the superblock in Fig. 2.2.

(b) Find the gs eigenvalue and eigenvector of the superblock.

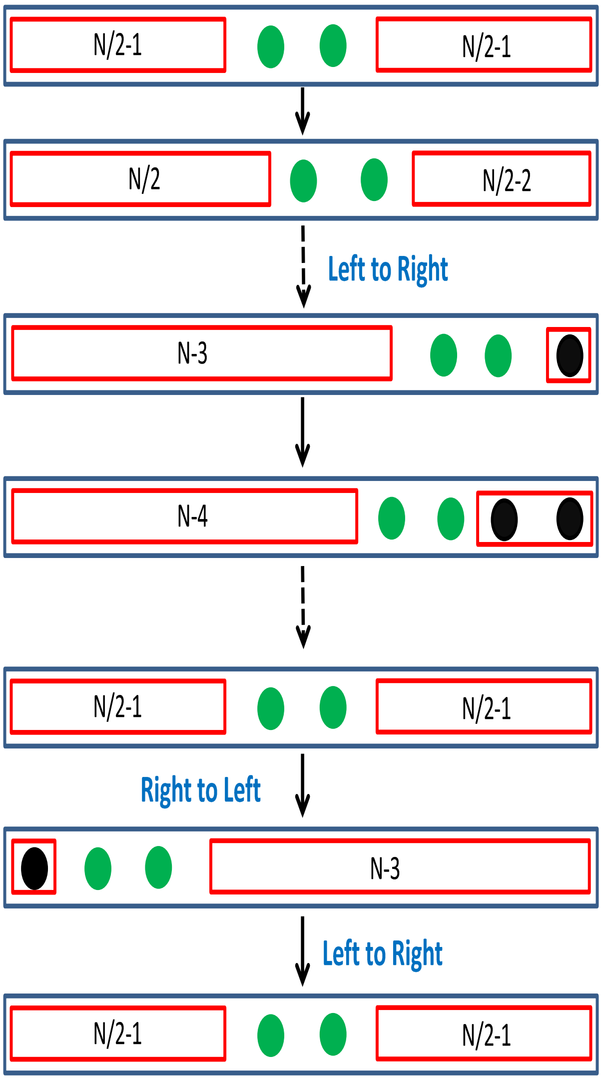

Figure 2.3: Schematic representation of the finite DMRG algorithm for a 1D chain. Filled green dots represent the new sites, blue boxes depict the final system of size N coming from infinite DMRG algorithm, and red boxes of unequal length represents the left and right block of varying sizes.

(c) The density matrix ρ of the system block is constructed. Diagonalize ρ and keep only the eigenvectors corresponding to the m largest eigenvalues.

(d) Renormalize all the operators and the Hamiltonian for the system block using Eq. 2.2. The new system block is old system block and a new site.

(e) Construct the superblock Hamiltonian using the effective Hamiltonian and operators of system blocks and two new sites.

(f) Repeat the process from (b) to (e) until the desired size is reached.

In the above process, the system is grown to desired N sites while keeping the fixed number of m relevant basis. However, the wavefunction of the full system may not be fully optimized. To have accurate results we need to optimized the system. To obtain accurate results for spin densities, correlation functions, and other gs properties in a finite system, the finite DMRG procedure is to be performed. The finite DMRG procedure is depicted schematically in Fig. 2.3 and summarized below.

(a) Start with the superblock with an equal number of sites in the left and the right block which was obtained at the end of the infinite DMRG algorithm procedure shown in Fig. 2.2.

(b) Find the gs eigenvector of the superblock. The new system block is the old block plus a new site as shown in Fig. 2.3. In the system block, one site is added to the system block at the left and removed from the environment block at the right at every step. Construct the reduced density matrix ρ' of the system block.

(c) Renormalize the Hamiltonian and operators of the system block through ρ'.

(d) The superblock Hamiltonian is constructed using the effective Hamiltonian and all the operators of the new system blocks and two new sites.

(e) Repeat all the steps from (a) to (d) until the left block goes to a site of $N-3$ and the right block reduced to one site.

(f) Now we grow the right block using (a) to (d) process till the left block reduced to 1 and the right block to $N-3$.

(g) In the next step, we again start moving the left block and reducing the right block till we reach a step where the left and the right block have the same size. The whole process is called one finite sweep.

In general $5-10$ finite sweeps are adequate to thermalize the 1D system.

The DMRG algorithm is a state-of-art numerical technique for a 1D and quasi-1D with open boundary condition (OBC). However, this algorithm fails to give an accurate result. It is well known that the PBC is essential to get rid of the boundary effect of a finite open chain and also to preserve the inversion symmetry in the system [15]. The number of relevant degrees of freedom in a 1D system with OBC is small as the entanglement between the blocks are small [13, 14]. Let us consider that for a system with OBC and for a given accuracy, m_{obc} number of eigenvectors of the density matrix are required. Then for the PBC system in the conventional DMRG, number of eigenvectors of the density matrix ρ required is $O(m_{obc}^2)$ [16] for same accuracy. The computational effort in the conventional DMRG for the OBC systems with sparse matrices goes as $O(m_{obc}^3)$, whereas it goes as $O(m_{obc}^6)$ for the PBC system [17]. The convergence accuracy of energies for the PBC systems calculated from the conventional DMRG decreases significantly.

The conventional DMRG is solved in a S^z basis. Therefore, most of the dominant S^z operator remains diagonal, whereas the raising operator S^+ and lowering operator S^- are off diagonal in this basis. Therefore, the multiple times renormalizations of these operators deteriorates the accuracy of these operators. The conventional algorithm is excellent for a 1D open chain as superblock is constructed with only one time renormalized operators. However, for a PBC system, one needs a long bond; therefore, at least two operators of superblock are renormalized multiple times. In a new algorithm [18], the multiple time renormalization of the operator is avoided by considering a superblock with four blocks consisting of a left and a right block and two new site blocks. In this algorithm, the superblock Hamiltonian is constructed using the effective Hamiltonian of blocks and operator which are renormalized once. Therefore, the truncation of long bond is avoided in this algorithm [18].

In this thesis, we are using conventional DMRG and another modified DMRG algorithm where four sites are added at every DMRG steps. This algorithm helps us avoid to use the multiple time renormalized operator in constructing the superblock of $J_1 - J_2$ model.

Bibliography

[1] H. Bethe, Z. Phys. **71**, 205 (1931).

[2] P. W. Anderson, Phys. Rev. **83**, 1260 (1951).

[3] A. O. Gogolin, A. A. Nersesyan, and A. M. Tsvelik, *Bosonization and Strongly Correlated systems*, (Cambridge University Press 1998).

[4] K. G. Wilson, Rev. Mod. Phys. **47**, 773 (1975); Rev. Mod. Phys. **55**, 583 (1983).

[5] M. Suzuki (Ed.), *Quantum Monte Carlo Methods in Condensed Matter Physics*, (World Scientific, Singapore 1993).

[6] C. Lanczos, J. Res. Natl. Bur. Stand. **45**, 255 (1950); J. Res. Natl. Bur. Stand. **49**, 33 (1952).

[7] R. Riedinger and M. Benard, J. Chem. Phys. **94**, 1222 (1990).

[8] E. R. Davidson, J. Comp. Phys. **17**, 87 (1975); E. R. Davidson, Computer in Physics **7**, 519 (1993).

[9] S. Rettrup, J. Comp. Phys. **45**, 100 (1982).

[10] J. W. Bray and S. T. Chui, Phys. Rev. **19**, 4876 (1979); J. E. Hirsh, Phys. Rev. B **22**, 5259 (1980).

[11] S. R. White and R. M. Noack, Phys. Rev. Lett. **68**, 3487-3490 (1992).

[12] S. R. White, Phys. Rev. Lett. **69**, 2863 (1992); Phys. Rev. Lett. **48**, 10345 (1993).

[13] K. A. Hallberg, Advances in Phys. **55**, 477-526 (2006).

[14] U. Schollwöck, Rev. Mod. Phys. **77**, 259 (2005).

[15] Z. G. Soos, A. Parvej, and M. Kumar, J. Phys. Condens. Matter **28**, 175603 (2016).

[16] U. Schollwöck, Ann. Phys. **326**, 96 (2011).

[17] P. Pippan, S. R. White, and H. G. Evertz, Phys. Rev. B **81**, 081103 (2011).

[18] D. Dey, D. Maiti, and M. Kumar, Papers in Physics **8**, 080006 (2016).

Chapter 3

Study of Quantum Phases for the Frustrated Heisenberg Spin-1/2 Model

3.1 Introduction

The $J_1 - J_2$ model with isotropic exchange J_1, J_2 between first and second neighbors is the frustrated spin-1/2 chain with a dimer phase, also called a bond-order-wave (BOW) phase [1–16]. The $J_1 - J_2$ Hamiltonian with PBC is shown in Eq. 1.17 in chapter 1. There is one spin per unit cell and the total spin S is conserved. The limit $J_2 = 0, J_1 > 0$ is the linear Heisenberg antiferromagnet (HAF) with non-degenerate ground state and QLRO at wave vector $q = \pi$. The limit $J_1 = 0, J_2 > 0$ corresponds to HAFs on sublattices of odd and even numbered sites, QLRO at $q = \pi/2$ and the model is frustrated for either sign of J_1. Sandvik [17] has reviewed numerical studies of the HAF and related spin chains, including $H(J_1, J_2)$ at $\alpha < 1$. An earlier review by Lecheminant [18] addresses frustrated 1D spin systems mainly in terms of field theory, also for $\alpha < 1$.

In addition to extensive HAF results, the exact gs is known at $\alpha_{MG} = 1/2$, the MajumdarGhosh [1] point, and at $J_1/J_2 = -4, J_2 > 0$, the quantum critical point

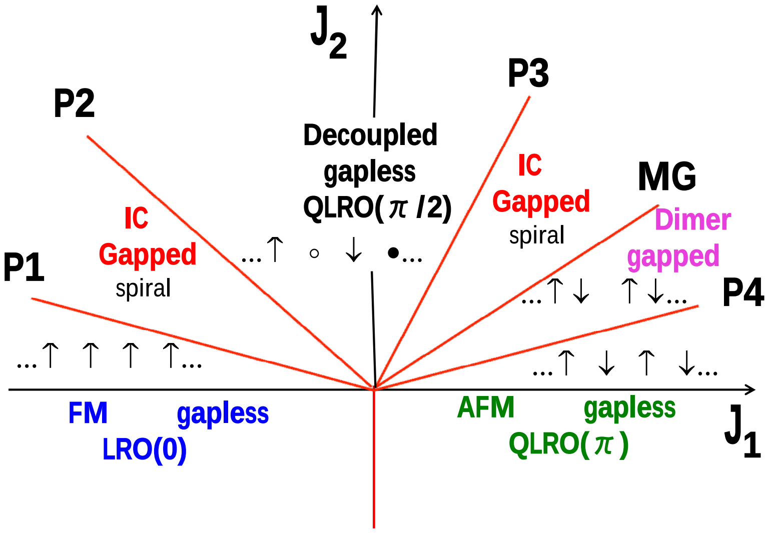

FIGURE 3.1: Quantum phase diagram of $H(J_1, J_2)$, Eq. 1.17. The J_1/J_2 values at the critical points are $P1 = -4, P2 = -1.24, P3 = 0.44$, and $P4 = 4.148$. The exact point $P1$ is between a gapless FM phase and a gapped IC phase. The gapless decoupled phase is between $P2$ and $P3$; open and closed circle denote spins pointing in and out of the plane. The gapped IC phase extends to the MG point, $J_1 = 2J_2$, and the dimer phase to $P4 = 4.148$, beyond which lies a gapless AFM phase.

$P1$ discussed by Hamada *et al.* [7] and shown in Fig. 3.1. Okamoto and Nomura [9] used ED of finite systems, level crossing and extrapolation to find the critical point $P4$ at $1/\alpha_{ON} = 4.148$ in Fig. 3.1. The dimer phase has doubly degenerate gs, broken inversion symmetry at sites and finite energy gap E_m to the lowest triplet state. The dimer phase and $P4$ were the initial focus of theoretical and numerical studies [1–19]. Attention has recently shifted to the $J_1 - J_2$ model with FM $J_1 < 0$ that is the starting point for the magnetic properties of Cu(II) chains in some cupric oxides [19–22]. Moreover, models in an applied magnetic field or with anisotropic exchange have multipolar, vector chiral and exotic phases [23–28]. Furukawa *et al.* [28] discuss both anisotropic and isotropic exchange using field theory and numerical methods and note that less is known about the $J_1 < 0$ sector.

The critical points $P2$ and $P3$ in Fig. 3.1 are obtained in the present study. An earlier estimate ($P2 = -1.2, P3 = 0.45$) was based [29] on level crossing and divergent structure factor peaks. We consider the phase diagram of the $J_1 - J_2$ model with particular attention to $P2$ and $P3$, the IC or spiral phases with spin correlations of finite range, the decoupled phase with QLRO($\pi/2$), and the commensurate to incommensurate (C-IC) point [30, 31] at $J_1/J_2 = 2$. We present numerical evidence such as the degeneracy of the gs to identify IC phases, the periodicity of spin correlations and the spin densities of the triplet state using ED for systems up to $N = 28$ spins and DMRG calculations [32, 33]. DMRG returns accurate gs energies and spin correlation functions $C(r)$ in systems of a few hundred spins. The combination of ED and DMRG in finite systems affords a detailed picture of IC and decoupled phases. The thermodynamic limit is deferred as long as possible.

Field theories introduce continuous operators for spin chains at the beginning and follow RG flows to distinguish between gapped and gapless phases. Exponentially small energy gaps or long-range spin correlations are beyond the reach of approximate numerical methods, and that is the case when J_1/J_2 is small or negative. Direct comparison is limited to systems with short-range spin correlations. Other comparisons are needed to support field theory or to assess conflicting results for IC and dimer phases. However, all field theories [12–14, 18, 23–26, 28] find that the QLRO($\pi/2$) phase in Fig. 3.1 is limited to the point $J_1 = 0$. We question the assertion that arbitrarily small J_1 suppresses the QLRO($\pi/2$) phase while finite $J_2/J_1 = 0.2411$ is needed to suppress the QLRO(π) phase. Weak exchange J_1 between HAFs on sublattices poses interesting and unresolved challenges, akin to dispersion forces, that merit closer attention.

There are basic differences at arbitrarily small gaps. Gapless critical phases at $J_1 = 0$ or $J_2 = 0$ have non-degenerate gs and divergent structure factor peaks. Gapped phases have doubly degenerate gs and finite structure factor peaks. We show that variable q in IC phases provides direct information about gs degeneracy and that the lowest triplet in the QLRO($\pi/2$) phase has broken sublattice spin densities. The physical picture in Fig. 3.1 extends the QLRO($\pi/2$) phase of HAFs on sublattices to small frustration J_1 of either sign, just as the QLRO(π) phase is stable against small frustration J_2. Increasing $J_1/J_2 > 0$ induces a quantum transition at $P3$ to a gapped IC phase with $q \geqslant \pi/2$ that terminates at the MG point, $J_1/J_2 = 2$. Decreasing $J_1/J_2 < 0$ gives a transition at $P2$ to an IC phase with $q \leqslant \pi/2$ that terminates at $J_1/J_2 = -4$. We use other numerical results than exponentially small energy gaps to obtain the quantum phase diagram in Fig. 3.1.

The chapter is organized as follows. The gs degeneracy and inversion symmetry are related in section 3.2 to the wave vector q_G of gs correlations. The structure factor $S(q)$, the Fourier transform of gs spin correlations, of finite systems is a discrete function. Its peak $S(q^*)$ is shown in section 3.3 to occur at $q^* = q_G$ except near the C-IC point. DMRG yields q_G in systems of several hundred spins using spin correlations instead of energy degeneracy. Level crossing of excited states is combined with q_G in section 3.4 and extrapolated to the thermodynamic limit to estimate the critical points $P2$ and $P3$. The decoupled phase is characterized in section 3.5 using the spin densities and sublattice spin of the lowest triplet state. The magnitude of $S(q)$ peaks at π or $\pi/2$ with increasing system size are compared in section 3.6. The gs expectation value $S_A^2 = S_B^2$ of the square of sublattice spin is related in section 3.7 to the asymmetry of $P2$ and $P3$ about $J_1 = 0$. Spin correlations $C(2r)$ within sublattices and $C(2r-1)$ between sublattices are compared. Two extensions of the $J_1 - J_2$ model are sketched in section 3.8. The first is an analytical model in which IC phases are suppressed and the decoupled phase expands to $J_1/J_2 = \pm 4 \ln 2$. The second has frustrated sublattices and a single IC phase without an intervening QLRO($\pi/2$) phase. In the Discussion we summarize the numerical evidence for the phase diagram in Fig. 3.1 and compare the field theoretical expression for $C(r)$ in gapped IC phases to DMRG results.

3.2 Ground State Spin Correlations

An even number of spins is assumed in spin-1/2 chains with isotropic exchange to ensure integer $S \leqslant N/2$. We take $N = 4n$ in order to have integer spin $S_A, S_B \leqslant n$

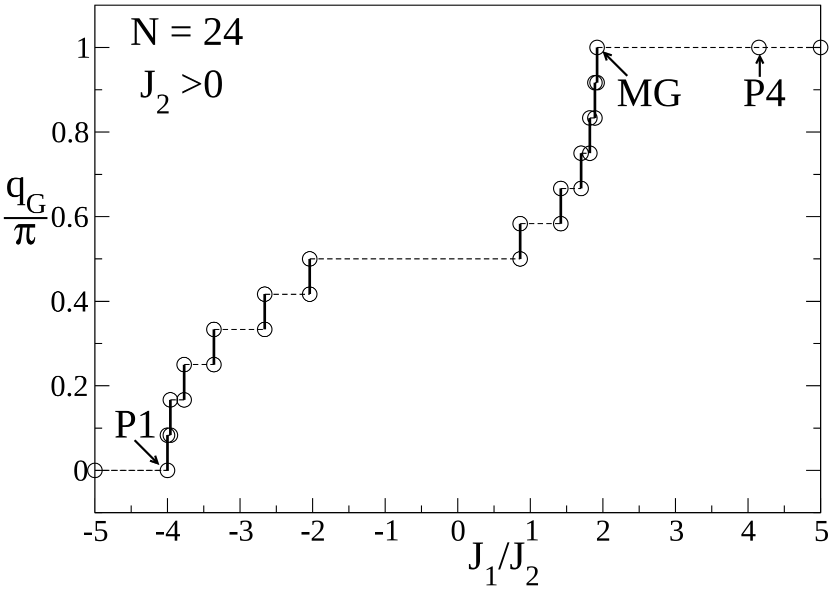

FIGURE 3.2: ED results for the wave vector q_G of gs correlations of the $J_1 - J_2$ model with 24 spins in Eq. 1.17. The singlet gs is degenerate at 12 points in sectors that are even and odd under inversion at sites; q_G switches between $\sigma = \pm 1$ with increasing J_1/J_2 starting with $q_G = 0$ at $J_1/J_2 = -4$ and ending with $q_G = \pi$ at $J_1/J_2 = 2$, both exact in the thermodynamic limit. The critical point $P4 = 4.148$ is to the gapless phase that includes the linear HAF at $J_2 = 0$.

on sublattices of odd and even numbered sites. The $J_1 = 0$ limit of Eq. 1.17 is then $2n$-spin HAFs, which is quite different from half-integer S_A, S_B when $N/2$ is an odd integer. The spontaneously broken symmetry is inversion σ at sites. Finite systems of $4n$ spins with PBC also have inversion symmetry σ' at the center of bonds. Open boundary conditions break σ symmetry and limit σ' to the central bond. While this does not matter in the thermodynamic limit, the issue would not come up if there were accurate results in that limit. The size limitations of ED are partly compensated by access to excited states. DMRG yields accurate gs properties [32, 33] of much larger systems. We use DMRG with PBC and four spins added per step [29, 34].

The gs is non-degenerate in $J_1 - J_2$ models of $4n$ spins with PBC except at $2n$ values [15, 27] of J_1/J_2. The wave vector is $k = 0$ or π in the $\sigma = 1$ or -1 sectors. We focus below on the wave vector q_G of gs spin correlations instead of k. As sketched in Fig. 3.1, spin correlations in the FM gs with $J_1/J_2 \leqslant -4$ have long-range order (LRO) at $q_G = 0$. On the AFM side, the gs has short-range spin correlations at $q_G = \pi$ for $J_1/J_2 \geqslant 2$ and QLRO at $q_G = \pi$ for $J_1/J_2 > 4.148$. The point $J_1 = 0$ with HAFs on sublattices has QLRO at $q_G = \pm\pi/2$. The gs of classical spins in Eq. 1.17 is a spiral phase with LRO(q_{cl}) in the interval $-4 \leqslant J_1/J_2 \leqslant 4$. The pitch angle q_{cl} between adjacent spin is given by $4\cos q_{cl} = -J_1/J_2$ and ranges from $q_{cl} = 0$ to $\pm\pi$ with increasing J_1/J_2. The same range of q_G occurs for quantum spins in which fluctuations suppress LRO and there is no simple relation to J_1/J_2. The evolution of q_G with increasing J_1/J_2 holds more generally for spin-1/2 chains with isotropic exchange and $q_G = 0$ or π at large negative or positive J_1.

Spin correlations $\langle \mathbf{S}_0 \cdot \mathbf{S}_r \rangle$ are gs expectation values that are commensurate in finite systems and limited to $r \leqslant 2n$ for $N = 4n$ sites. PBC leads to discrete q in the first Brillouin zone

$$q = \frac{\pi r}{2n}, \qquad r = 0, \pm 1, ..., 2n. \tag{3.1}$$

The periodicity of gs correlations in the $J_1 - J_2$ model increases from $q_G = 0$ to π, or decreases from $q_G = 0$ to $-\pi$, in $2n$ steps of $\pi/2n$ between $P1$ at $J_1/J_2 = -4$ and the MG point at $J_1/J_2 = 2$. The end points are exact and hold in the thermodynamic limit.

The gs degeneracy at $J_1/J_2 = 2$ is between two singlets, the Kekulé valence bond (VB) diagrams for singlet-pairing of adjacent spins,

$$\begin{aligned} |K1\rangle &= (1,2)(3,4)...(4n-1)(4n), \\ |K2\rangle &= (2,3)(4,5)...(4n,1), \end{aligned} \tag{3.2}$$

where $(1,2) = (\alpha_1\beta_2 - \beta_1\alpha_2)/\sqrt{2}$ at sites 1 and 2. The diagrams are related by inversion at sites. The inversion symmetry is also broken at $J_1/J_2 = -4$ and altogether at $2n$ points $\alpha_p(4n) = J_2/J_1, p = 1, 2, ...2n$ [15, 27]. The α_p are known up to $N = 28$ and are accessible [17] for $N = 32$. The Kekulé diagrams are asymptotically orthogonal, with overlap $\langle K1|K2\rangle = (-2)^{-n+1}$ for n singlet pairs given by Paulings island counting rule [35]. Spin correlations in small systems at $J_1/J_2 = 2$ depend on overlap [5], but overlap is negligible for $N > 24$ and $\langle \mathbf{S}_0 \cdot \mathbf{S}_r \rangle = 0$ for $r \leqslant 2$ at the MG point.

The FM gs for $J_1/J_2 \leqslant -4$ and singlet gs for $J_1/J_2 \geqslant 2$ are in the $\sigma = 1$ sector for arbitrarily large $N = 4n$. The gs transforms as $\sigma = -1$ at $q_G = \pi r/2n$ when r is an odd integer and as $\sigma = 1$ when r is an even integer. Fig. 3.2 shows q_G for $N = 24$ as a function of J_1/J_2 with 12 steps at $\alpha_p(4n)$. The staircase goes from $q_G = 0$ to π. An equivalent staircase runs from $q_G = 0$ to $-\pi(= \pi)$. The stairs have equal risers $\pi/2n$ and variable steps governed by $\alpha_p(4n)$, both of which depend on system size. The onset and termination of IC phases at $J_1/J_2 = -4$ and 2 are exact. The long step or plateau at $q_G = \pi/2$ in Fig. 3.2 is between $\alpha_n(4n)$ with $J_1 < 0$ and $\alpha_{n+1}(4n)$ with $J_1 > 0$. Another special feature of this step becomes apparent on doubling the system from N to $2N$, or from 24 to 48 in Fig. 3.2. The wave vectors $\{q\}_N$ also appear in $\{q\}_{2N}$ of the larger system that has N additional qs. The additional wave vectors are midway between every $\{q\}_N$ except at $q = \pi/2$ where there are two new steps at $q = \pi/2 \pm \pi/N$.

The gs degeneracy and inversion symmetry specify the periodicity $2\pi/q_G$ of spin correlations in finite $J_1 - J_2$ models. The wave vectors are uniformly distributed while the degeneracies are not. The degeneracy density between $0 \leqslant J_1/J_2 \leqslant 2$ is twice that between $-4 \leqslant J_1/J_2 \leqslant 0$. More important is the possibility of an interval without degeneracy. What is the fate of the $q_G = \pi/2$ plateau in the thermodynamic limit? A plateau implies a C phase, as in Fig. 3.1, between two IC phases. Small deviations from $q_G = \pm\pi/2$, on the other hand, would indicate a C point at $J_1 = 0$ between IC phases. Exact degeneracies require ED and are therefore limited to small systems. To follow the evolution of q_G with increasing J_1/J_2, we use DMRG and gs spin correlations instead of energy degeneracy.

3.3 Spin Structure Factor

The static structure factor $S(q)$ is the Fourier transform of spin correlations in the gs

$$S(q) = \sum_r \langle \vec{S}_0 \cdot \vec{S}_r \rangle \exp(iqr). \tag{3.3}$$

The wave vectors in Eq. 3.1 are for $4n$ spins and one spin per unit cell. $S(q)$ is even in q and symmetric about $q = 0$ and π. $S(0)$ is the sum of $\langle \mathbf{S}_0 \cdot \mathbf{S}_r \rangle$ over r, and $S(0) = 0$ when the gs is a singlet. The discrete function $S(q)$ has peaks at $\pm q^*$ over a finite J_1/J_2 interval. Bursill *et al.* [11] discussed an effective periodicity $2\pi/q^*$ based on $S(q)$ peaks. Except close to $J_1/J_2 = 2$, IC phases have $q_G = q^*$. Instead of energy degeneracy and symmetry, however, q^* is based on gs spin correlations and is much more convenient to evaluate. First, we are seeking q_G as a function of J_1/J_2 in the thermodynamic limit rather than staircases such as Fig. 3.2 in large systems. Second and more importantly, DMRG is an excellent gs approximation that yields spin correlations in large systems.

Broken inversion symmetry is the motivation for evaluating average spin correlations as

$$C(r) = (\langle \vec{S}_0 \cdot \vec{S}_r \rangle + \langle \vec{S}_0 \cdot \vec{S}_{-r} \rangle)/2. \tag{3.4}$$

The two expectation values are equal by translational symmetry for non-degenerate gs, for example in the $\sigma = 1$ or -1 sectors, but are not equal for arbitrary linear combinations of degenerate gs. Indeed, the order parameter of the dimer phase in Fig. 3.1 is the difference between the two expectation values with $r = 1$ in Eq. 3.4 and can be evaluated directly in finite $J_1 - J_2$ models at points where the gs is doubly degenerate [15, 27]. The Kekulé diagrams have $\langle \mathbf{S}_0 \cdot \mathbf{S}_1 \rangle = -3/4$ and 0 at nearest neighbors. The average $C(r)$ enters in $S(q)$ since the sum in Eq. 3.3 is over sites both to the right and left. Inversion symmetry is not specified in our DMRG algorithm. We compute both expectation values in Eq. 3.4 and take the average or difference as required by the problem being addressed.

The nodal structure of $C(r)$ for $J_1 < 0$ confirms that $q_G = q^*$. The $S(q)$ peak is at the Fourier component that matches the sign changes of $C(r)$. Peaks at

$q^* = \pm\pi/2n$ close to $q_G = 0$ at $P1$ are well resolved for any system size since $S(0) = 0$ in the singlet gs with $\sigma = -1$ and two sign changes of $C(r)$. The peaks jumps to $q^* = \pm\pi/n$ at $\alpha_2(4n)$ when the gs is even under inversion and $C(r)$ changes sign four times. We verified for $N = 24$ that q^* follows q_G exactly when $J_1 < 0$ and $C(r)$ changes sign up to $2n$ times. We have $C(2r-1) = 0$ at $J_1 = 0$ and $C(2r) \propto (-1)^r$. The $q^* = \pi/2$ peak is reached well before $J_1 = 0$, however, at small rather than vanishing correlations between spins in different sublattices.

We also find $q^* = q_G$ for $J_1 > 0$ except near the MG point, $J_1/J_2 = 2$, where the exact structure factor is

$$S_{MG}(q) = 3(1 - \cos q)/4. \tag{3.5}$$

The size dependence is entirely in the discrete values of q, with $q^* = \pi$ and

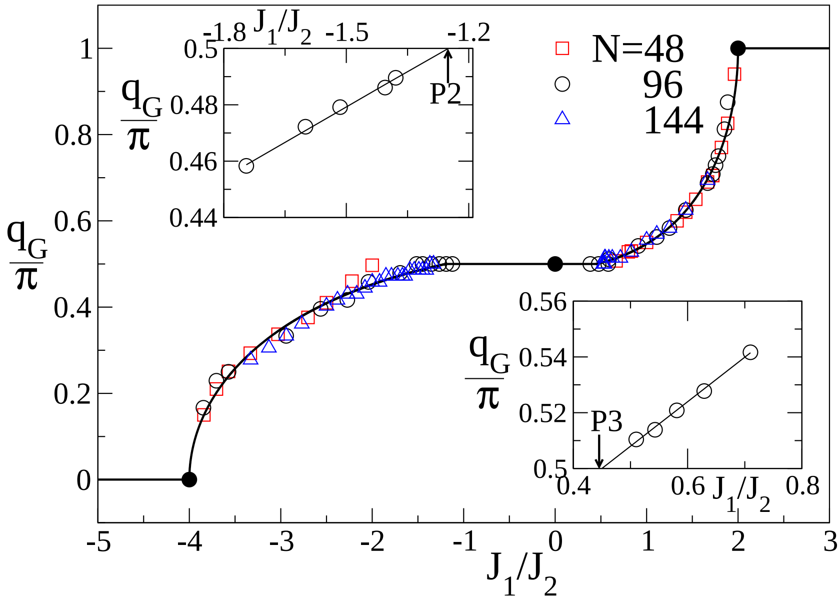

Figure 3.3: DMRG results for the wave vector q_G of gs correlations as a function of J_1/J_2 in models of N spins in Eq. 1.17. Closed circles are exact in the thermodynamic limit. The insets show the J_1/J_2 values in Table 3.1 at which the $q_G/\pi = 1/2$ plateau is reached and left in a step $2/N$ for $J_1 < 0$ and $J_1 > 0$; linear extrapolation gives the quantum critical points $P2 = -1.24$ and $P3 = 0.44$. The intervals $(-4, P2)$ and $(P3, 2)$ with variable q_G are IC phases with degenerate gs. The C phase between $P2$ and $P3$ has a non-degenerate gs.

$S_{MG}(\pi) = 3/2$. A broad profile in reciprocal space is readily understood as extremely short range $C(r)$ in real space. The profile narrows for $J_1/J_2 > 2$ as the range of correlations increases [29]; $S(\pi)$ increases and diverges in the QLRO(π) phase with $J_1/J_2 \geqslant 4.148$.

On the other hand, the gs in the $\sigma = -1$ sector at the MG point has $q_G = \pi - \pi/2n$ and is the C-IC point of the $J_1 - J_2$ model, as noted [30, 31] previously for spin chains with an exact point. Finite $S(\pi)$ leads to overlapping profiles at $q_G = \pi \pm r \pm /2n$ that are first resolved in the thermodynamic limit at the Lifshitz point where $S''(\pi) = 0$. Bursill *et al.* [11] found $(J_2/J_1)_L = 0.52063(6)$ using DMRG with OBC. $S''(\pi) = 0$ requires that the spin correlations at $(J_1/J_2)_L$ satisfy

$$0 = -4n^2 C(2n) - 2 \sum_{r=1}^{2n-1} r^2 (-1)^r C(r). \tag{3.6}$$

Short-range correlations make it possible to evaluate $(J_1/J_2)_L$ accurately. We find $(J_2/J_1)_L = 0.52066(2)$ for $N > 50$ in excellent agreement with the earlier result [11]. The resolved peaks at $\pm q^*$ separate for $J_1/J_2 < 1.92$ and merge with $\pm q_G$. We have $q^* = q_G$ for $q_G \leqslant 2\pi/3$ at $N = 24$ and expect similar merging of q^* to q_G in large systems since as shown in section 3.7, $S(\pi)$ decreases rapidly with decreasing $J_1/J_2 < 2$.

DMRG and $S(q)$ peaks yield q_G in large systems. The evolution of $q^* = q_G$ with J_1/J_2 in IC phases is shown in Fig. 3.3 for $4n = 48, 96$ and 144. The point at $J_1 = 0$ is exact, as are $q_G = 0$ and π for $J_1/J_2 \leqslant -4$ and $\geqslant 2$, respectively. The size dependence is confined to the $q_G = \pi/2$ plateau that defines an interval with non-degenerate gs in finite systems. The plateau is reached at $(J_1/J_2)_n$ in a step of $\pi/2n$ for $J_1 < 0$ and is left at $(J_1/J_2)_{n+1}$ in a step of $\pi/2n$ for $J_1 > 0$. These points are listed in Table 3.1 up to $N = 192$ and are shown in the insets of Fig. 3.3. The lines are linear extrapolations to the thermodynamic limit. The intercepts $J_1/J_2 = -1.24$ and 0.44 are the q_G estimates for $P2$ and $P3$ in Fig. 3.1. To check the accuracy, we recall that the sum $\sum_r C(r) = S(0)$ is zero in singlet states; it is $< 6 \times 10^{-4}$ up to $N = 144$ in Table 3.1 and about 3×10^{-3} at $N = 192$. The linear

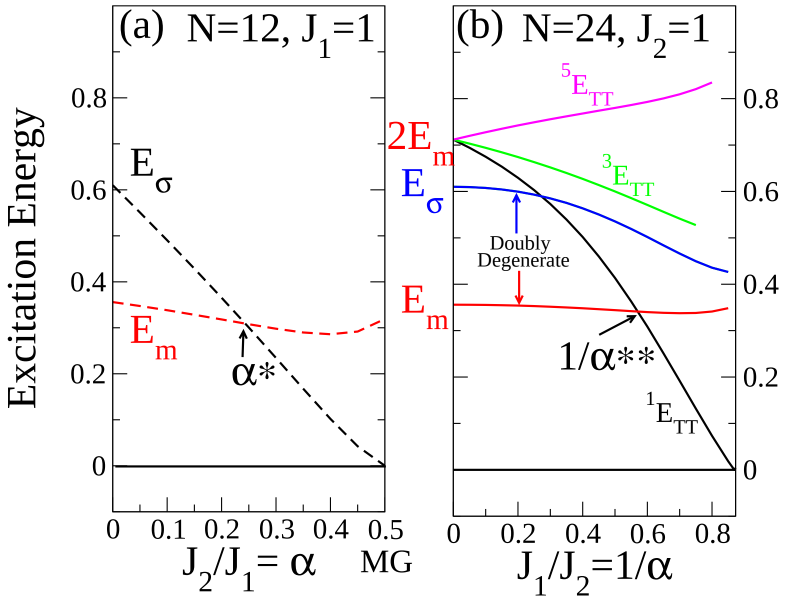

FIGURE 3.4: Excitation energies of the $J_1 - J_2$ model, Eq. 1.17: (a) Lowest triplet E_m and singlet E_σ for $N = 12$ and $\alpha = J_2/J_1 \leqslant \alpha_{MG} = 1/2$ where the gs is doubly degenerate. The crossing $E_m = E_\sigma$ is $\alpha^* = 0.245$. (b) $N = 24, J_2 = 1$ and $1/\alpha = J_1/J_2 \leqslant 0.87$ where the gs is doubly degenerate. $2E_m$ is nine-fold degenerate at $J_1 = 0$ with a triplet on each sublattice. The singlet ${}^1E_{TT}$ has allowed crossings with E_σ and E_m.

behavior of $(J_1/J_2)_n$ and $(J_1/J_2)_{n+1}$ for $N > 48$ are directly related to system size since q_G steps are known to be $\pm\pi/2n$.

To conclude the analysis of q_G in IC phases, we construct the solid line in Fig. 3.3. Classical spins account for the square root behavior at the exact point $J_1/J_2 = -4$. Nomura and Murashima [33] suggested on general field theoretical grounds that $q \propto (\alpha - \alpha_c)^{1/2}$ near the C-IC point, with $J_2/J_1 \geqslant \alpha_c = 1/2$. We expand instead about small J_1/J_2 and recall that the gs correlations of Eq. 1.17 have $q_G = 0, \pi/2$ and π, respectively, at $J_1/J_2 \leqslant -4, 0$ and $\geqslant 2$. The combination of a square root singularity at exact points and the $J_1 = 0$ constraint of $q_G = \pi/2$ suggests the expressions

$$\begin{aligned}
\frac{q_G}{\pi} &= A\Big(4+\frac{J_1}{J_2}\Big)^{1/2}\exp\Big(-a\Big(4+\frac{J_1}{J_2}\Big)\Big)\leqslant\frac{1}{2} & -4\leqslant\frac{J_1}{J_2}\leqslant P2\\
\frac{q_G}{\pi} &= \frac{1}{2} & P2\leqslant\frac{J_1}{J_2}\leqslant P3\\
\frac{q_G}{\pi} &= 1-B\Big(2-\frac{J_1}{J_2}\Big)^{1/2}\exp\Big(-b\Big(2-\frac{J_1}{J_2}\Big)\Big)\geqslant\frac{1}{2} & P3\leqslant\frac{J_1}{J_2}\leqslant 2.
\end{aligned}\qquad(3.7)$$

The corresponding curve from $q_G = 0$ to $-\pi(=\pi)$ is $-q_G/\pi$. The parameters in Fig. 3.3 are $A = 0.38, B = 0.565, a = 0.086$ and $b = 0.22$. A and B refer to singularities that are known in the thermodynamic limit; a and b are negligible near the exact points but they matter for the critical points $P2$ and $P3$ that delimit the $q_G = \pi/2$ phase. Eq. 3.7 combines singularities at exact points and with the translational symmetry of the $J_1 - J_2$ model before making a continuum approximation.

3.4 Level Crossing

The gs degeneracy of finite $J_1 - J_2$ models is between singlets with opposite inversion symmetry. We define E_σ and E_m as the excitation energy to the lowest singlet and triplet, respectively. Both have finite-size contributions. Fig. 3.4 (a) shows the evolution of E_m and E_σ with increasing frustration $\alpha = J_2/J_1$ for $N = 12$ spins in Eq. 1.17. The gs and excited singlet cross at $\alpha_{MG} = 1/2$ where $E_\sigma = 0$. The singlet and triplet levels cross at $\alpha^*(12) = 0.245$ where $E_\sigma = E_m$. Motivated by field theory, Okamoto and Nomura [9] argued that the gapped dimer phase with doubly degenerate gs must have two singlets below the lowest triplet. In finite systems, the singlet and triplet cross at $\alpha^*(N)$ where $E_\sigma = E_m$. They found [9] $\alpha^*(N)$ exactly to $N = 24$, noted the weak size dependence and extrapolated to $\alpha_{ON} = 0.2411 = 1/P4$.

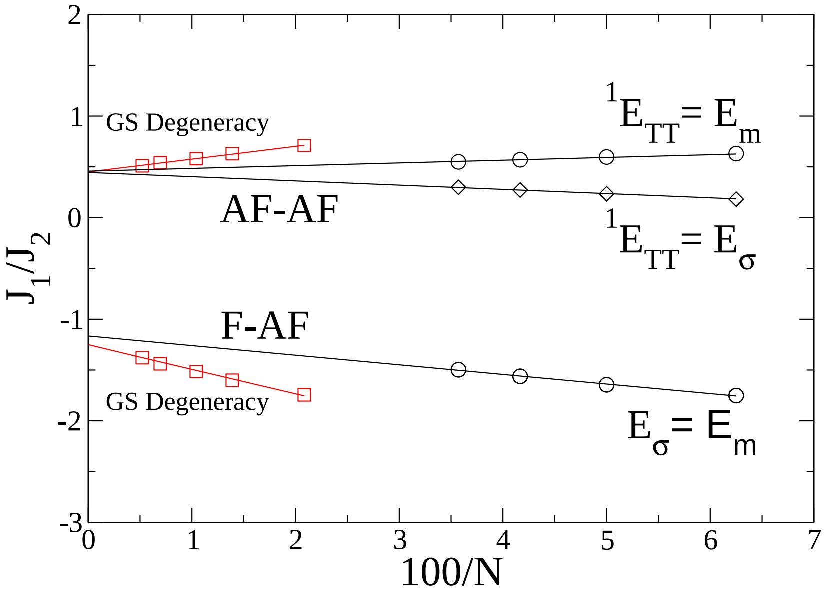

FIGURE 3.5: ED results for level crossing and DMRG results for gs degeneracy in $J_1 - J_2$ models with $N = 4n$ spins in Eq. 1.17. The crossing $E_\sigma = E_m$ is between the lowest singlet excitation and lowest triplet state; ${}^1E_{TT}$ is the singlet excitation that evolves from triplets on each sublattice at $J_1 = 0$. The gs degeneracy and linear extrapolation are the q_G points in the insets to Fig. 3.3. The critical points in the thermodynamic limit are at $P2 = -1.24$ and $P3 = 0.44$.

The excitations E_m and E_σ are well known at $J_2 = 0$. To lowest order in logarithmic corrections,Woynarovich and Eckle report [36]

$$E_m(N) = \frac{\pi^2}{2N}\left(1 - \frac{1}{2\ln N}\right). \tag{3.8}$$

Faddeev and Takhtajan show [37] that the triplet (E_m) and singlet (E_σ) are degenerate in the infinite chain; they are the $S = 1$ and 0 linear combinations of two $S = 1/2$ kinks with identical dispersion relations. Combining $E_m(N)$ with coupling constants reported by Affleck *et al.* [8], the difference $E_\sigma(N) - E_m(N)$ is of order $1/(N \ln N)$, even smaller than $1/N$.

The $J_1 = 0$ limit of Eq. 1.17 has HAFs on sublattices. As seen in Fig. 3.4 (b), the $N = 24$ excitations at $1/\alpha = 0$ are those of $N = 12$ HAFs. Now E_m and E_σ transform [29] with wave vector $k = \pm\pi/2$ and remain doubly degenerate for

TABLE 3.1: DMRG results for the points $(J_1/J_2)_n$ and $(J_1/J_2)_{n+1}$ at which the $q_G = \pi/2$ plateau is reached and left in $J_1 - J_2$ models of $4n$ spins.

$N = 4n$	$(J_1/J_2)_n$	$(J_1/J_2)_{n+1}$
24	-2.033	0.868
48	-1.745	0.710
72	-1.600	0.629
96	-1.515	0.581
144	-1.439	0.543
192	-1.379	0.510
∞	-1.24	0.44

small J_1/J_2. The nine-fold degeneracy at $2E_m$ for a triplet on each sublattice corresponds to a singlet, a triplet, and a quintet whose energies we denote as ${}^1E_{TT}$, ${}^3E_{TT}$, and ${}^5E_{TT}$, respectively. The degeneracy is lifted for $J_1 > 0$ when only total spin is conserved. The singlet at excitation energy ${}^1E_{TT}$ has allowed crossings [29] with E_σ and E_m at finite J_1/J_2 that are shown in Fig. 3.5 up to $N = 28$. The HAF excitations above rationalize why both level crossings in finite systems extrapolate to $J_1/J_2 \sim 0.45$. The crossings $E_\sigma(N) = E_m(N)$ for $J_1 < 0$ are also shown to $N = 28$.

Fig. 3.5 also shows the points in Table 3.1 at which the $q_G = \pi/2$ plateau is reached and left. The same linear extrapolation is used. Level crossing and gs degeneracy are consistent and independent determinations. Level crossing involves excited states while q_G depends on gs correlations. Although $P2 = -1.24(3)$ and $P3 = -0.44(2)$ are approximate, they indicate two IC phases in Fig. 3.1 separated by a C phase with $q_G = \pi/2$ and non-degenerate gs between $J_1/J_2 = -1.24$ and 0.44. The size dependence of level crossings at small J_1 is far weaker than that of q_G, but not as weak as at small J_2.

On the other hand, field theories that limit QLRO($\pi/2$) to $J_1 = 0$ would require all lines in Fig. 3.5 to extrapolate to $J_1 = 0$. This seems unlikely to us and in any case level crossing has to be taken into account. For whatever reason, field theories [12–14, 18, 23, 28] that routinely refer to $E_\sigma = E_m$ for $P4$ have not considered level crossing at small J_1/J_2. The present analysis of gs degeneracies is new evidence for a C phase with non-degenerate gs and $q_G = \pm\pi/2$ between two IC phases with doubly degenerate gs and variable q_G.

3.5 Triplet State Spin Densities

In this section we further characterize the decoupled C phase using the triplet state $|T, \sigma\rangle$ with $S = S^z = 1$, excitation energy E_m and inversion symmetry σ. ED gives $|T, \sigma\rangle$ explicitly in finite systems. The spin density at site r is

$$\rho_r(\sigma) = \langle T, \sigma | S_r^z | T, \sigma \rangle. \tag{3.9}$$

The triplets wave vector k_T can be inferred from spin densities. Uniform $\rho_r = (4n)^{-1}$ at all sites indicates non-degenerate $|T, \sigma\rangle$ with $k_T = 0$ for $\sigma = 1$ and π for $\sigma = -1$. Doubly degenerate $|T, \sigma\rangle$ with $\pm k_T$ in Eq. 3.1 indicates broken

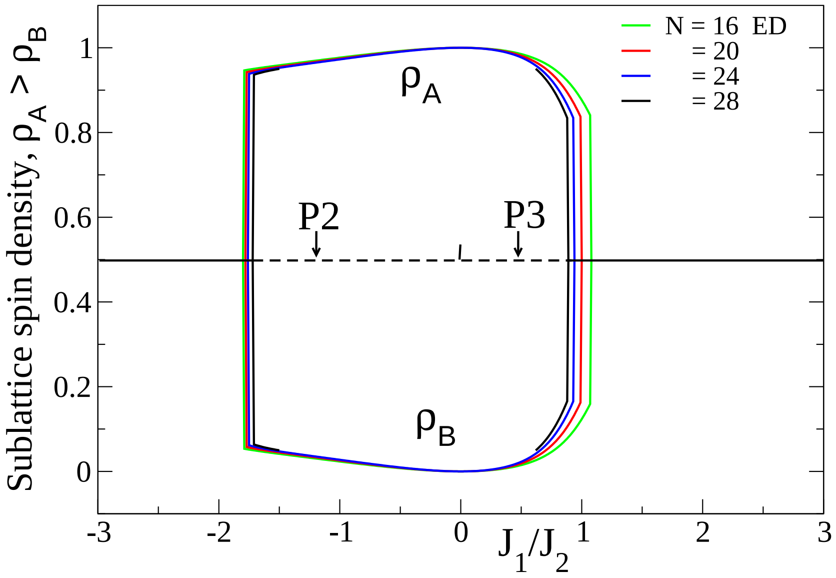

FIGURE 3.6: Sublattice spin density, Eq. 3.10, with $\rho_A \geqslant \rho_B$ as a function of J_1/J_2 for N spins in Eq. 1.17. ED results to $N = 28$ show finite $|\rho_A - \rho_B|$ when the lowest triplet state $|T, \sigma\rangle$ has wave vector $k_T = \pm\pi/2$ and $\rho_A = \rho_B = 1/2$ otherwise. The critical points $P2$ and $P3$ are based on q_G and $|\rho_A - \rho_B| = 1$ at $J_1 = 0$ is exact.

spin density symmetry with $\rho_r(1) \neq \rho_r(-1)$. The spin densities for $\sigma = \pm 1$ are proportional to $\cos^2 k_T r$ and $\sin^2 k_T r$, so that the sum $(4n)^{-1}$ is the same at all sites. The spin density of odd numbered sites is

$$\rho_A = \sum_{r=1}^{n} \rho_{2r-1}. \tag{3.10}$$

The sublattice spin density of even numbered sites is $\rho_B = 1 - \rho_A$ since $S^z = 1$ is conserved. We have $\rho_A = \rho_B = 1/2$ except when $k_T = \pm\pi/2$. At $J_1 = 0$, for example, $|T, \sigma\rangle$ is either $|T\rangle\,|G\rangle$ or $|G\rangle\,|T\rangle$ where $|G\rangle$ and $|T\rangle$ are the gs and lowest triplet of sublattices. The product functions have opposite σ symmetry; ρ_A or ρ_B is uniformly $(2n)^{-1}$ on one sublattice and 0 on the other.

The evolution of $\rho_A \leqslant \rho_B$ is shown in Fig. 3.6 as a function of J_1/J_2 using ED up to $N = 28$. The sudden changes to $\rho_A = \rho_B = 1/2$ at $(J_1/J_2)_T$ indicate a level crossing of triplets. There are four degenerate triplets at $(J_1/J_2)_T$, a pair $|T, \pm 1\rangle$ with $k_T = \pi/2$ and a pair with $k_T = \pi/2 - \pi/2n$ in the $J_1 < 0$ sector or $\pi/2 + \pi/2n$ in the $J_1 > 0$ sector. Increasing $J_1/J_2 > 0$ or decreasing $J_1/J_2 < 0$ generates additional triplet degeneracies at which the sublattice spin densities do not change. The points $(J_1/J_2)_T$ are close to $(J_1/J_2)_n$ and $(J_1/J_2)_{n+1}$ where q_G reaches and leaves the $\pi/2$ plateau. The IC phases have degenerate $|T, \sigma\rangle$ with $k_T < \pi/2$ or $> \pi/2$, while $|T, \sigma\rangle$ is non-degenerate in the dimer phase with $E_m > 0$ or in the QLRO(π) phase with $E_m = 0$.

The eigenstates at $J_1 = 0$ are products of $2n$-spin HAFs. The product basis is complete, and $|T, \sigma\rangle$ can expanded at any J_1/J_2 as a linear combination of products of sublattice eigenstates with $S_A + S_B = 1$. Since σ does not interchange sublattices, product functions have fixed σ. Since the sublattices are equivalent, however, the expansion coefficients C_{ij} and C_{ji} of products such as ${}^3|j\rangle\,{}^1|i\rangle$ and ${}^1|i\rangle\,{}^3|j\rangle$ must have equal magnitudes, where $|i\rangle$ and $|j\rangle$ refer to the ith singlet and jth triplet of $2n$-spin HAFs. Triplets based on $S_A = S_B \geqslant 1$ have $\rho_A = \rho_B = 1/2$, while triplets based on $|S_A - S_B| = 1$ have $\rho_A \neq \rho_B$. Degenerate triplets $|T, \sigma\rangle$ at finite J_1/J_2 are linear combinations of product functions with decreasing but finite $|\rho_A - \rho_B|$ in Fig. 3.6 as long as $k_T = \pm\pi/2$.

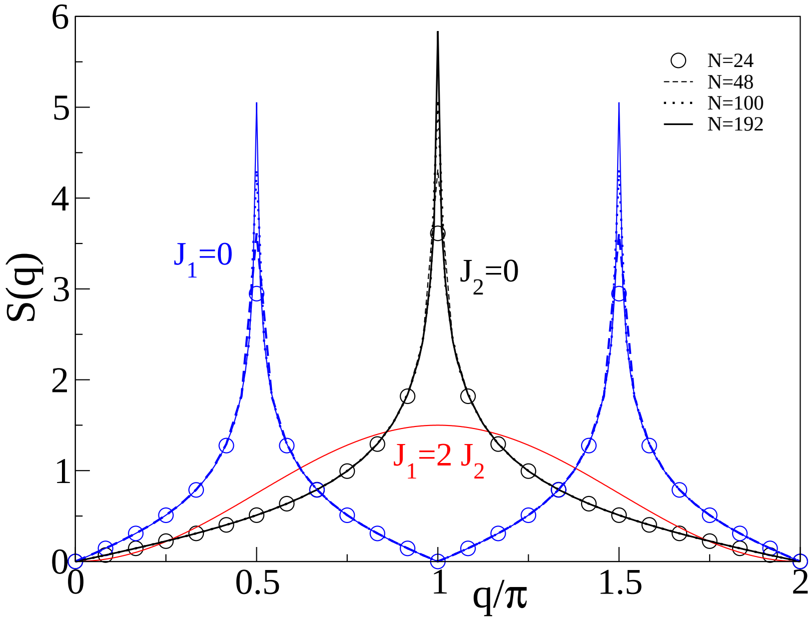

FIGURE 3.7: Spin structure factor $S(q)$, Eq. 3.3, for $J_2 = 0, J_1 = 0$, and $J_1/J_2 = 2$ in Eq. 1.17. Open symbols are ED for $N = 24$ and discrete wave vector q. Lines are DMRG for $N = 48, 96$, and 192, respectively, with increasing peaks and continuous q. $S(q)$ at $J_1/J_2 = 2$ is Eq. 3.5, exact in the thermodynamic limit. The π and $\pi/2$ peaks diverge in that limit.

DMRG is applicable to larger systems because $|T, \sigma\rangle$ has the lowest energy in the sector $S = S^z = 1$. The algorithm does not specify inversion symmetry, however, and returns some linear combination of $|T, 1\rangle$ and $|T, -1\rangle$ for a degenerate triplet. There are four degenerate triplets at $(J_1/J_2)_T$ where sublattice spins become unequal. When $k_T = \pi/2$, we have $\rho_A \neq \rho_B$ except for the plus or minus linear combination. On the other hand, all linear combinations of $|T, 1\rangle$ and $|T, -1\rangle$ lead to $\rho_A = \rho_B = 1/2$ when $k_T \neq \pi/2$. The wave vector is sufficient to estimate $(J_1/J_2)_T$ in large systems. Within numerical accuracy, finite J_1/J_2 leads to equal sublattice spin densities when $k_T \neq \pi/2$ and to finite fluctuations $|\rho_A - \rho_B| > 0$ when $k_T = \pi/2$. DMRG results for $(J_1/J_2)_T$ are consistent with but considerably less accurate than $(J_1/J_2)_n$ and $(J_1/J_2)_{n+1}$ in Table 3.1 for reaching and leaving the $q_G = \pi/2$ plateau. The $J_1 = 0$ spin densities for non-interacting sublattices are exact for any system size and $|\rho_A - \rho_B| > 0$ is readily demonstrated for $-1.2 < J_1/J_2 < 0.4$. The decoupled C phase identified by level crossing and gs degeneracy has a degenerate triplet $|T, \pm 1\rangle$ with $k_{_T} = \pm\pi/2$ and broken sublattice spin density $\rho_{_A} \neq \rho_{_B}$.

3.6 Magnitude of Structure Factor Peaks

The spin structure factor, Eq. 3.4, has $C(0) = 3/4$ for $S = 1/2$ and satisfies the sum rule

$$\frac{1}{4n}\sum_q S(q) = \frac{3}{4} = \frac{1}{\pi}\int_0^\pi S(q)dq. \tag{3.11}$$

The sum and integral refer to finite and infinite systems with discrete and continuous q. HAF spin correlations, indicated by the subscript zero, between distant sites go as [6, 17]

$$C_0(r) \propto \frac{(-1)^r(\ln r)^{1/2}}{r}. \tag{3.12}$$

Fig. 3.7 shows $S(q)$ for HAFs and for the $J_1 - J_2$ model at $J_1/J_2 = 2$. Since $(-1)^r C_0(r)$ is positive, the sum is over $|C_0(r)|$ and $S(\pi)$ diverges as $(\ln N)^{3/2}$ when the integral is cut off at N. The $S(\pi)$ peak increases as shown from $N = 24$ to 192. The size dependence is weak except at the peak, the area is conserved in all curves, and $S'(\pi)$ is not defined in the thermodynamic limit.

Only spins in the same sublattice contribute to $S(\pi/2)$. At $J_1 = 0$, the correlations between distant sites have even r in Eq. 3.12 and $\cos(r\pi/2)$ instead of $(-1)^r$. The gs has QLRO($\pi/2$) and divergent $S(\pi/2)$. The size dependence in Fig. 3.7 is again small except at the peaks $\pi/2$ and $3\pi/2$ ($= -\pi/2$). The $S(\pi/2)$ divergence is suppressed by J_1 in gapped IC phases. This is readily shown [29] for $1 < J_1/J_2 < 2$ where E_m is large and correlations are short ranged.

Eq. 3.12 indicates divergent $S(\pi)$ at $J_2 = 0$ and $S(\pi/2)$ at $J_1 = 0$ in the thermodynamic limit. Divergent peaks are signatures of QLRO but have not been demonstrated directly for other parameters. Finite $S_{_{MG}}(\pi) = 3/2$ clearly implies a critical point $P4$ such that $S(\pi)$ diverges for $J_1/J_2 \geqslant P4$. The same logic leads to the critical points $P2$ and $P3$ where $S(\pi/2)$ diverges. We compute $C(r)$ in finite systems and compare the size dependence of $S(\pi/2)$ at small J_1 to that of $S(\pi)$ at small J_2.

The magnitudes of $S(\pi; J_2 = 0, 4n)$ and $S(\pi/2; J_1 = 0, 8n)$ are necessarily equal since both systems are $4n$-spin HAFs. Small J_2 gives a first-order correction, $J_2C_0(2)$, that reduces π order for $J_2 > 0$ and enhances it for $J_2 < 0$. Small J_1 couples non-interacting HAFs and there is no first-order correction. The difference between a perturbed system and weak exchange between two systems has important consequences. To lowest order in J_1, spin correlations within a sublattice go as [29]

$$C(2r) = C_0(2r) + O(J_1/J_2)^2. \tag{3.13}$$

The result holds in finite systems whether or not $C(2r)$ is amenable to exact evaluation. The leading terms in the Taylor expansion of $S(\pi; J_2, 4n)$ about $J_2 = 0$ and of $S(\pi/2; J_1, 8n)$ about $J_1 = 0$ are

$$\begin{aligned} S(\pi; J_2/J_1, 4n) &= S(\pi; 0, 4n) - A_n(J_2/J_1) \\ S(\pi/2; J_1/J_2, 8n) &= S(\pi; 0, 4n) - B_n(J_1/J_2)^2. \end{aligned} \tag{3.14}$$

ED for 24 spins returns [29] $A_6 \sim 10B_3 > 0$ for $J_1/J_2 > 0$. DMRG to $N = 100$ confirms [29] that small J_2/J_1 reduces the π peak more than small J_1/J_2 reduces the $\pi/2$ peak, which in turn is reduced faster for $J_1/J_2 > 0$ than for $J_1/J_2 < 0$. The initially quadratic dependence in Eq. 3.13 points to weaker suppression of the $S(\pi/2)$ divergence by J_1 than of the $S(\pi)$ divergence by J_2. Field theory asserts instead that $S(\pi/2)$ becomes finite for arbitrarily small J_1/J_2. Numerical analysis is consistent with divergent peaks in QLRO phases whose critical points are determined by level crossing and gs correlations.

There is a basic difference between the π and $\pi/2$ peaks. $S(q)$ is symmetric about π, with $S(\pi-\varepsilon) = S(\pi+\varepsilon)$. If a finite system has a π peak, the peak remains there when $S(q)$ is assumed to be continuous in the thermodynamic limit, whether or not the system size exceeds the range of spin correlations. In other words, whether or not the assumption is justified. The divergence is not related to the peaks position. The critical points $P2$ and $P3$ are between IC and QLRO($\pi/2$) phases, however, and $S(q)$ is not symmetric about $q = \pi/2$ except at $J_1 = 0$. A finite system with a $\pi/2$ peak has unequal $S(q)$ at $q = \pi/2 \pm \pi/2n$, as can readily be verified analytically. The peak necessarily shifts to $q < \pi/2$ for $J_1 < 0$ and continuous $S(q)$ or to $q > \pi/2$ for $J_1 > 0$ when $S(\pi/2)$ is assumed to be finite in the thermodynamic limit and hence differentiable at the peak. Even if accurate $C(r)$ could be found at small J_1/J_2 in large systems, extrapolation would be necessary to determine whether $S(\pi/2)$ diverges. Gapped IC phases have spin correlations of finite range, and q_G immediately shifts at $P2$ or $P3$ from the $q_G = \pi/2$ plateau in Fig. 3.3.

3.7 Sublattice Spin and Correlations

The critical points $P2 = -1.24$ and $P3 = 0.44$ are far from symmetric about $J_1 = 0$. AF exchange between sublattices quickly induces an IC phase at $P3$ while the IC phase at $P2$ requires stronger FM exchange. A qualitative explanation is that $J_1 > 0$ stabilizes the singlet ${}^1E_{TT}$ that is involved in level crossing and generates the gs degeneracy $(J_1/J_2)_{n+1}$ in systems of $4n$ spins. The eigenstate ${}^1|T\rangle\,|T\rangle$ at $J_1 = 0$ is the singlet linear combination of the lowest triplet on each sublattice. On the contrary, FM exchange raises the energy of ${}^1|T\rangle\,|T\rangle$ and the singlet gs must be achieved with minimal sublattice spin. We present a more quantitative analysis of the $P2, P3$ asymmetry.

The gs of Eq. 1.17 with $J_2 \geqslant 0$ is a singlet for $-4 \leqslant J_1/J_2$. Sublattice spin is conserved at $J_1 = 0$ where $S_A = S_B = 0$, but not in general. The gs expectation value of $\langle S_A^2\rangle = \langle S_B^2\rangle$ per site is

$$\frac{\langle S_A^2\rangle}{2n} \equiv \sum_{r=0}^{2n-1} C(2r) = \frac{S(\pi)}{2} = -2\sum_{r=1}^{n-1} C(2r-1). \tag{3.15}$$

The equality with $S(\pi)/2$ follows on using $S(0) = 0$ for singlets. The second equality is an immediate consequence of $\langle (S_A + S_B)^2\rangle = 0$. The following results are exact: $\langle S_A^2\rangle/2n = 0$ at $J_1 = 0$ as required; $\langle S_A^2\rangle/2n$ is 3/4 at $J_1/J_2 = 2$ and it diverges for $J_1/J_2 \geqslant 4.148$. Another exact result obtained below is $\langle S_A^2\rangle/2n = 1/4$

Table 3.2: DMRG spin correlation functions $\langle \mathbf{S}_0 \cdot \mathbf{S}_r \rangle = C(r)$ to $r = 20$ for $N = 96$ spins in Eq. 1.17 and $J_1/J_2 = -1, 0.4$ and 0.

$N = 96$	$\frac{J_1}{J_2} = -1$	$\frac{J_1}{J_2} = 0.4$	$\frac{J_1}{J_2} = -1$	$\frac{J_1}{J_2} = 0.4$	$J_1 = 0$
r	$C(2r-1)$	$C(2r-1)$	$C(2r)$	$C(2r)$	$C_0(2r)$
1	0.02577	-0.02141	-0.43154	-0.43771	-0.44351
2	-0.05097	0.02980	0.17342	0.17652	0.18238
3	0.03521	-0.02220	-0.13741	-0.14199	-0.15160
4	-0.02960	0.01836	0.09029	0.09506	0.10487
5	0.02275	-0.01498	-0.07859	-0.08305	-0.09414
6	-0.01934	0.01258	0.06035	0.06431	0.07490
7	0.01576	-0.01045	-0.05427	-0.05801	-0.06963
8	-0.01331	0.00890	0.04498	0.04839	0.05917
9	0.01110	-0.00744	-0.04164	-0.04488	-0.05619
10	-0.00928	0.00640	0.03663	0.03959	0.04963

at $J_1/J_2 = -4$, three times smaller than at $J_1/J_2 = 2$. The size dependence is weak when $S(\pi)$ is a minimum. DMRG at $J_1/J_2 = -1$ and 0.4 returns $\langle S_A^2 \rangle / 2n \sim 0.015$ and 0.010, respectively.

In units of J_2, the gs energy per site is $-3/4$ at $J_1/J_2 = -4$. The singlet correlations $C(r)$ go as $\cos(\pi r/2n)$ and satisfy two conditions: $C(0) = 3/4$ and $\sum_r C(r) = 0$. Up to amplitude $A(n)$, we have

$$C(r) = \frac{A(n)}{4} \cos(\pi r/2n) + \left(\frac{3}{4} - \frac{A(n)}{4} \right) \left(\frac{4n\delta_{0r} - 1}{4n - 1} \right), \tag{3.16}$$

where δ_{0r} is the Kroneker delta. The energy per site is $-4C(1) + C(2)$. Setting the energy equal to $-3/4$ gives a linear equation for $A(n)$. We obtain $A(n) = 1 + 1/(2n)$ up to corrections of order n^{-4} and $\langle S_A^2 \rangle / 2n = 1/4$. Adjacent spins are asymptotically parallel in the singlet. Eq. 3.16 is consistent with Hamada *et al.* [7] where a note added in proof indicates that an analytical expression for $\langle S_i^z S_j^z \rangle$ had been found at $J_1/J_2 = -4$.

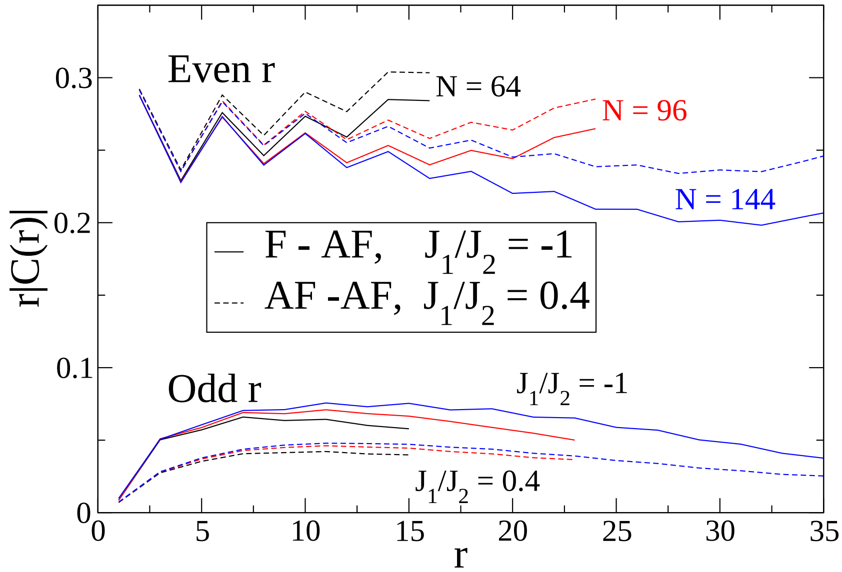

FIGURE 3.8: Spin correlation functions $C(r)$ in $J_1 - J_2$ models with N spins in Eq. 1.17. Both $J_1/J_2 = -1$ and 0.4 are in the decoupled phase with $q_G = \pi/2$ that includes $J_1 = 0$.

We chose to study $J_1/J_2 = -1$ and 0.4 in the decoupled phase with $q_G = \pi/2$. Table 3.2 lists $C(r)$ up to $r = 20$ for $N = 96$ at $J_1/J_2 = -1, 0.4$ and 0, where $C_0(2r)$ refer to a 48-spin HAF. Shiroishi and Takahashi [38] obtained analytical expression for $C_0(r)$ in the thermodynamic limit up to $r = 4$. The first four entries $C_0(2r)$ at $N = 96$ differ from the analytical results by less than 10^{-3}, and the $N = 192$ correlations by $< 2.5 \times 10^{-4}$. DMRG is quite accurate, as expected. Spin correlations $C(2r)$ within sublattices are almost identical at $J_1/J_2 = -1$ and 0.4. Their nodal structure goes as $\cos(\pi r)$, just as at $J_1 = 0$. Indeed, they remain close to $C_0(2r)$ as suggested by Eq. 3.13 even at substantial deviations from $J_1 = 0$. Exchange between sublattices leads to comparable but out of phase $C(2r - 1)$ that follows from the fact that the gs energy has $J_1 C(1) < 0$.

Correlations are strictly limited to $r \leqslant 2n$ in systems of $N = 4n$ sites with PBC. Converged $C(r)$ are further limited to $r \sim n/2 = N/8$ based on various criteria [17, 39]. DMRG results in Fig. 3.8 at $J_1/J_2 = -1$ and 0.4 show $r|C(r)|$ separately for even and odd r up to $r = n$ for $4n = 64, 96$ and 144. Convergence is fair to $r < n/2$ along with typical HAF oscillations at small r, here on sublattices. Converged $r|C(2r)| \sim 0.25$ in Fig. 3.8 are roughly constant whereas the $r|C_0(2r)|$ at $J_1 = 0$ in Eq. 3.12 increases slowly.

Substantial spin correlations $C(2r-1)$ are new results: at intermediate r we find $(2r-1)|C(2r-1)| \sim 0.06$ and ~ 0.04 at $J_1/J_2 = -1$ and 0.4, respectively. The nodal structure of $C(2r-1)$ in Table 3.2 goes as $\pm\sin((2r-1)\pi/2)$ with wave vector $\pi/2$. We understand $J_1C(1) < 0$ and $q = \pi/2$ but not why the magnitude of $C(3)$ is larger than that of $C(1)$ or why $C(2r-1)$ then decreases roughly as $1/r$. The small value of $S(\pi)/2$ at $J_1/J_2 = -1$ or 0.4 in the decoupled phase is due to extensive cancellation in Eq. 3.15 among spin correlations in different sublattices.

FM spin correlations $C(1) > 0$ are central to the Haldane dimer phase proposed by Furukawa *et al.* [28] in the interval $-4 \leqslant J_1/J_2 < 0$, as indicated in their Eq. (32) and shown in their Fig. (2) at $J_1/J_2 = -2, \Delta = 1$ (isotropic exchange), which is well inside the IC phase. The gs has slightly larger $C(1) > 0$ with one neighbor than the other. Such broken symmetry states can be constructed in finite $J_1 - J_2$ models whenever the gs is doubly degenerate, and only inversion symmetry is broken in $J_1 - J_2$ models with isotropic exchange [27]. The IC phases in Fig. 3.1 can also be viewed as dimer or bond-order-wave phases, both with $J_1C(1) < 0$. Numerical results are shown in Fig. (6) of [28] for $C(1)$, correlation lengths and string correlations. No points are shown,however, between $-1 < J_1/J_2 < 0.5$ which is considered to be an IC phase (except at $J_1 = 0$) that is beyond numerical analysis. The excluded region almost coincides with the QLRO($\pi/2$) phase between $P2$ and $P3$ in Fig. 3.1.

3.8 Two Related Models

In this section we summarize two models whose quantum phases are related to those of the $J_1 - J_2$ model. The first is an analytical model with HAFs on sublattices and mean-field exchange that suppresses IC phases and widens the QLRO($\pi/2$) phase; the critical points $P1/P2$ merge to $J_1/J_2 = -4\ln 2$ and $P3/P4$

to $J_1/J_2 = 4\ln 2$. The second retains J_1 between neighbors. Frustration within sublattices merges $P2/P3$ and generates a single IC phase from $q_G = 0$ to $\pm\pi$. The motivation is to manipulate the critical points in Fig. 3.1 in predictable ways using exact thermodynamic results as far as possible.

The $J_1 - J_2$ model has N exchanges J_1 between adjacent sites. The total exchange is the same for $(N/2)^2$ exchanges $4J_1/N$ between all spins in different sublattices, as in the Lieb-Mattis model [40]. Equal exchange $4J_1/N$ is the mean-field (mf) approximation for exchange between sublattices. The frustrated mf model for $4n$ spins is

$$H_{mf} = \frac{4J_1}{N} \sum_{r,r'=1}^{2n} \vec{S}_{2r} \cdot \vec{S}_{2r'-1} + J_2 \sum_{r=1}^{4n} \vec{S}_r \cdot \vec{S}_{r+2}. \tag{3.17}$$

Sublattice spin is conserved as seen on rewriting the first term as

$$\frac{4J_1}{N} \sum_{r,r'=1}^{2n} \vec{S}_{2r} \cdot \vec{S}_{2r'-1} = \frac{2J_1}{N}((S_A + S_B)^2 - S_A^2 - S_B^2). \tag{3.18}$$

The eigenstates of H_{mf} are products of HAF eigenstates in sectors with $S_A = S_B \leqslant n$. We define $J_2 E(S, 2n)$ as the lowest energy for $S \leqslant n$. The $S = 0$ energy per site is $E(0, 2n)/2n = \epsilon_0 = 1/4 - \ln 2$ in the thermodynamic limit. The gs is the combination of $S = S_A + S_B$ and $S_A = S_B$ that minimizes the energy in Eq. 3.17.

The QLRO($\pi/2$) phase with $S = S_A = S_B = 0$ is the gs for $J_1 < 0$ until the FM state with $S = S_A + S_B = 2n$ is reached at $J_1/J_2 = -4\ln 2$ in the thermodynamic limit. The gapped IC phase with $J_1 < 0$ has disappeared and q_G changes discontinuously from 0 to $\pi/2$ at $J_1/J_2 = -2.773$. The quantum transition is first order. The gapped IC and dimer phases are also suppressed for $J_1 > 0$. The AFM state with $S = 0$ and $S_A = S_B = n$ is reached in the thermodynamic limit at $J_1/J_2 = 4\ln 2$ where q_G jumps from $\pi/2$ to π. In fact, the gs remains the product $|G\rangle\, |G\rangle$ of noninteracting HAFs between $J_1/J_2 = -4\ln 2$ and $\pi^2/4$; all $C(2r-1)$ are rigorously zero in the interval [29]. The gs between $\pi^2/4$ and $4\ln 2$ is [41] ${}^1|T\rangle\, |T\rangle$, the singlet linear combination of the lowest triplet of each sublattice.

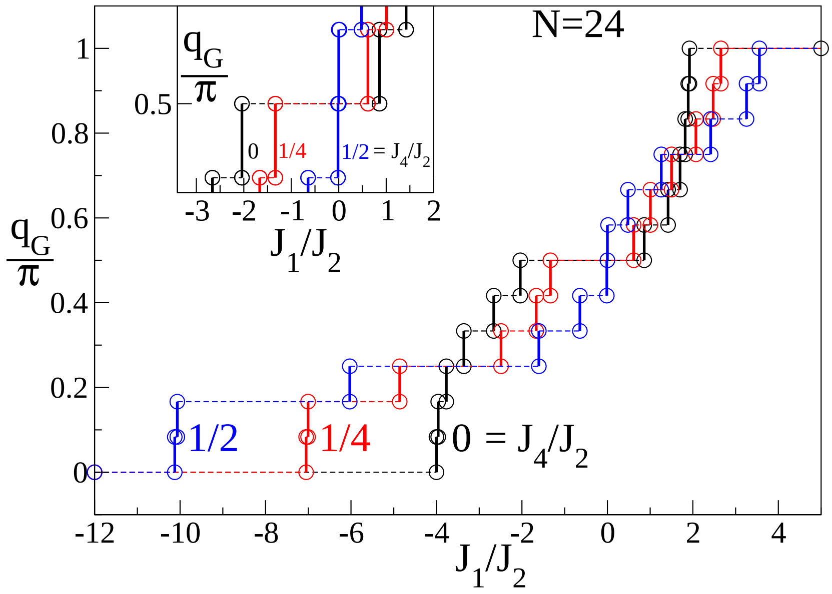

FIGURE 3.9: ED results for the wave vector q_G of gs correlations of the doubly frustrated model, Eq. 3.19, with $N = 24$ spins and $J_4/J_2 = 0, 1/4$, and $1/2$. The inset enlarges the $q_G = \pi/2$ region. The singlet gs is degenerate at 12 points in sectors that are even and odd under inversion at sites.

There are infinitely many ways of going from equal $4J_1/N$ between spins in different sublattices and to nearest neighbor J_1. The critical points depend on the choice of exchange between sublattices. Large $J_1 < 0$ generates LRO(0) while large $J_1 > 0$ generates either [41, 42] LRO(π) or QLRO(π). The mf model, Eq. 3.17, rigorously has a gapless critical QLRO($\pi/2$) phase. The critical points depend on the choice of exchanges, and all choices have QLRO($\pi/2$) at $J_1 = 0$ for decoupled sublattices. If somehow the QLRO($\pi/2$) phase of the $J_1 - J_2$ model were limited $J_1 = 0$, the immediate question would be what exchange between sublattices restores the QLRO($\pi/2$) phase to a J_1/J_2 interval.

The second model is doubly frustrated. In addition to exchange J_1 between first neighbors, we consider exchange$J_4 > 0$ between second neighbors of sublattices. The doubly frustrated chain is

$$H_D = J_1 \sum_r \vec{S}_r \cdot \vec{S}_{r+1} + J_2 \sum_r \vec{S}_r \cdot \vec{S}_{r+2} + J_4 \sum_r \vec{S}_r \cdot \vec{S}_{r+4}. \tag{3.19}$$

Several exact results follow immediately. When $J_1 = 0$, frustration is within sublattices and the MG point at $J_4/J_2 = 1/2$ is four-fold degenerate. The singlet-paired sites in one of the Kekulé diagrams of sublattice A is

$$|K1_A\rangle = (1,3)(5,7)...(2n-3)(2n-1). \tag{3.20}$$

The other diagram goes as $(3,5)(7,9)...(2n-1,1)$. The corresponding pairing in sublattice B is between nearest neighbor even sites. Still at $J_1 = 0$, the QLRO($\pi/2$) phase of either sublattice extends to $J_4/J_2 = 0.2411$, the critical point $P4$ for sublattices.

At constant $J_4/J_2 = 0.2411$, the quantum phase diagram of H_D as a function of J_1/J_2 has a QLRO($\pi/2$) point at $J_1 = 0$ between two IC phases, and any additional frustration $J_1 \neq 0$ suppresses long-range spin correlations. The $J_1 - J_2$ model has $J_4 = 0$ and its QLRO($\pi/2$) phase in Fig. 3.1 is suppressed at finite J_1/J_2. Lets consider the phase boundaries in the $J_1/J_2, J_4/J_2$ plane. The QLRO($\pi/2$) phase at the origin is stable along $J_1 = 0$ up to $J_4/J_2 = 0.2411$ and, in our analysis, to $P2 < 0$ and $P3 > 0$ when $J_4 = 0$. Field theories limit the QLRO($\pi/2$) phase of the $J_1 - J_2$ model to $J_1 = 0$. The implied fragility of the QLRO($\pi/2$) phase to $J_1 \neq 0$ at $J_4 = 0$ is contrasted in the doubly frustrated model its robustness at $J_1 = 0$ to $J_4 > 0$.

The J_4 term of H_D strongly perturbs the points at which the gs is degenerate. ED for $N = 24$ returns the q_G versus J_1/J_2 staircases in Fig. 3.9 for $J_4/J_2 = 0, 1/4$, and 1/2. The inset enlarges where $q_G = \pi/2$ is reached at $J_1 < 0$ and left at $J_1 > 0$. Increasing J_4 substantially lengthens the steps on the $J_1 < 0$ side and decreases the $\pi/2$ plateau, which at $J_4/J_2 = 1/4$ is no wider than some other steps. As shown in the inset, the $q_G = \pi/2$ step is almost entirely suppressed at $J_4/J_2 = 1/2$, the MG point of non-interacting sublattices. Finite J_1 breaks the four-fold degeneracy. The $S(q)$ peak at $J_4/J_2 = 1/2$ remains at $\pi/2$ for $J_1/J_2 = \pm 10^5$ but is already at $\pi/2 \pm \pi/12$ at $J_1/J_2 = \pm 10^{-4}$.

Increasing J_4 shifts the gs degeneracy with the FM state to more negative J_1/J_2. Classical spins provide a qualitative explanation. The extra term $J_4 \cos 4q_{cl}$ leads to pitch angle q_{cl}

$$\frac{J_1}{J_2} = -4\Big(1 + \frac{4J_4}{J_2}\cos 2q_{cl}\Big)\cos q_{cl}. \tag{3.21}$$

The $q_{cl} = 0$ result is $J_1/J_2 = -4$, exact at $J_4 = 0$. It increases to $J_1/J_2 = -8$ and -12 at $J_4/J_2 = 1/4$ and $1/2$, which is more negative than for quantum spins. The slope $(\partial q_{cl}/\partial(J_1/J_2))_0$ at $J_1 = 0$ is $1/4$ when $J_4 = 0$. The slope diverges at $J_4/J_2 = 1/4$, when the rhs of Eq. 3.21 is $-8\cos 3q_{cl}$. For classical spins and $J_4/J_2 = 1/2, q_{cl}$ jumps discontinuously from $\pi/3$ to $2\pi/3$ at $J_1 = 0$, as follows from $4\cos 2q_{cl} = 1$. The $N = 24$ results for $q_{_G}$ in Fig. 3.9 are consistent with the expectation that the QLRO($\pi/2$) phase of $H_{_D}$ is suppressed in the thermodynamic limit for $J_4/J_2 > 0.2411$.

3.9 Discussion

The gs of the $J_1 - J_2$ model, Eq. 1.17 with $J_2 \geqslant 0$, is a singlet for $-4 \leqslant J_1/J_2$. Other spin-1/2 chains with frustrated isotropic exchange have a singlet gs over some range of parameters. The singlet gs of finite systems with PBC is non-degenerate in general, but is doubly degenerate at $2n$ points in models with $4n$ spins and inversion symmetry at sites. The wave vector $q_{_G}$ of spin correlations can be used to find gs degeneracies in IC phases, which is our principal result. Variable $q_{_G}$ in Fig. 3.3 indicates two IC phases. One is between the exact critical point $J_1/J_2 = -4$ and $J_1/J_2 = -1.24$ based on the size dependence of $q_{_G}$; the other is between $J_1/J_2 = 0.44$ estimated from $q_{_G}$ and the exact MG point, $J_1/J_2 = 2$, which is the C-IC point. In between is a gapless critical C phase with non-degenerate gs and QLRO($\pi/2$). The lowest triplets $|T, \pm 1\rangle$ in the decoupled phase have wave vector $k_{_T} = \pm\pi/2$ and broken sublattice spin densities $\rho_{_A} \neq \rho_{_B}$ that reaches $|\rho_{_A} - \rho_{_B}| = 1$ at $J_1 = 0$.

The structure factor $S(q)$ is a convenient way to find energy degeneracies in finite systems using gs properties. The gs is rigorously non-degenerate on the $q_{_G} = \pi/2$ plateaus between $(J_1/J_2)_n$ and $(J_1/J_2)_{n+1}$ in Table 3.1. Our numerical results are in excellent agreement with previous results for $S(q)$ in other contexts. As noted in section 3.3, the Lifshitz point where $S''(\pi) = 0$ is $(J_1/J_2)_L = 0.52066$, which matches the result of Bursill *et al.* [11]. Sudan *et al.* [24] studied multipolar spin correlations and magnetization of the $J_1 - J_2$ model with $J_1 < 0$. The lower panel of their Fig. (4) shows the $S(q)$ peak, q_{max}/π, for $-4 \leqslant J_1/J_2 \leqslant -2$ at zero field based on ED to $N = 28$. Our DMRG results leading to Eq. 3.7 are closely similar: $q_{max}/\pi = 0.250$ at $J_1/J_2 = -3.53$ and ≈ 0.45 at -2 in either case. Furukawa *et al.* [28] use the infinite time evolving block decimation algorithm (iTEBD). The $\Delta = 1$ (isotropic exchange) curve of the $S(Q)$ peak Q versus J_1/J_2 in Fig. (16) of [28] has constant $Q = \pi/2$ in the J_1/J_2 interval from about -1.1 to 0.5. The resemblance to q_G/π in Fig. 3 is striking. In the IC phase at $J_1/J_2 = -1.8$, Fig. (8) of [28], has $Q/\pi = 0.470$ compared to 0.466 according to Eq. 3.7.

We summarize the quantum phase diagram of the $J_1 - J_2$ model in Fig. 3.1 as follows. The gapless FM phase with LRO(0) holds in the sector with $J_1 < 0$ and $J_2/J_1 \leqslant -1/4$, including $J_2 < 0$. Similarly, the gapless AFM phase with QLRO(π) holds in the sector $J_1 > 0$ and $J_2/J_1 \leqslant 0.2411$. The gapless decoupled phase with QLRO($\pi/2$) holds in the sector with $J_2 > 0$ and $-1.24 \leqslant J_1/J_2 \leqslant 0.44$. Between the gapless phases with non-degenerate gs are gapped IC and dimer phases with doubly degenerate gs and spin correlations of finite range. The IC phase with $-4 \leqslant J_1/J_2 \leqslant -1.24$ has variable q_G ranging from 0 to $\pm\pi/2$. The IC phase with $0.44 \leqslant J_1/J_2 \leqslant 2$ has q_G ranging from $\pm\pi/2$ to $\pi(= -\pi)$. The dimer phase has $q_G = \pi$, and $2 \leqslant J_1/J_2 \leqslant 4.148$. As seen in Fig. 3.5, level crossing and gs degeneracy extrapolate to the same critical points $P2 = -1.24$ and $P3 = 0.44$. The gapless QLRO(q) phases have divergent $S(q)$ peaks while gapped phases have finite peaks.

These numerical results have a simple qualitative interpretation. The gs energy per site of the $J_1 - J_2$ model is

$$\epsilon_0(J_1, J_2) = J_1 C(1) + J_2 C(2). \tag{3.22}$$

The gs at $J_2 = 0$ has spin correlations with $q_G = 0$ for $J_1 < 0$ and $q_G = \pi$ for $J_1 > 0$. The second neighbor correlation $C(2)$ is positive in both cases. It follows that $C(1)$ changes sign when J_1 does and that $J_2 > 0$ is frustrating in either case. Increasing J_2 leads to $C(2) = 0$ at the MG point, $J_1/J_2 = 2$, or at $q_G = \pi/4$ where $J_1/J_2 = -3.53$. The situation is quite different in the decoupled QLRO($\pi/2$) phase in which spin correlations $C(2r-1)$ between sublattices are identically zero at $J_1 = 0$. Since the phase is compatible with small $C(1)$ of either sign, finite J_1 is very weakly frustrating at first and the decoupled phase extends over a substantial interval about $J_1 = 0$.

As proposed by White and Affleck [12], the distance dependence of spin correlations in gapped IC phases goes as

$$C_{IC}(r) \propto (\cos Qr) r^{-1/2} \exp -r/\xi. \tag{3.23}$$

They remark that Eq. 3.23 is approximate and holds for $r/\xi \gg 1$. DMRG calculations of $C_{IC}(r)$ at $J_1/J_2 = 0.56$, well inside the IC phase, were fit [12] in their Fig. (9) to $\xi = 17.1$ and pitch angle $Q = \pi/2 + \pi/(4\xi)$. DMRG with two spins added per site has numerical difficulties [12] when $J_1/J_2 < 0.5$. The field theory of White and Affleck leads [12] to $1/\xi \propto \exp(-aJ_2/J_1)$ for $J_1 > 0$, where a is a free parameter, while that of Itoi and Qin returns [14] $1/\xi \propto \exp(-c(J_2/J_1)^{2/3})$ with different c for positive and negative J_1. In either case, $\xi > 0$ ensures a finite range of correlations and hence a finite $S(q)$ peak for $J_1 \neq 0$.

The expression for $C_{IC}(r)$ has been adopted and rationalized in subsequent studies of the $J_1 - J_2$ model [28, 33] as well as the bilinear-biquadratic chain of $S = 1$ spins [30]. Now Q is identified as q^*, the structure factor peak. Furukawa *et al.* [30] report (Fig. 6(b) of [28]) $\xi = 36$ at $J_1/J_2 = -1.8$ in the IC phase; they note that, as anticipated by Itoi and Qin [14], ξ is larger for $J_1 < 0$ than for $J_1 > 0$. Still in the IC phase, DMRG with four spins added [16] per step leads to $\xi = 27$ and 23.5 at $J_1/J_2 = 0.48$ and 0.54, respectively, and as shown in Fig. (6) of [16] requires different amplitudes for $C(2r)$ within and $C(2r-1)$ between sublattices. These examples indicate that $C_{IC}(r)$ holds in IC phases. However, the $C(r)$ in Table 3.2 are not compatible with $C_{IC}(r)$ and $Q = \pi/2$, which immediately gives $C(2r-1) = 0$, in contrast to finite correlations in Fig. 3.9 between spins in different sublattices and $q_G = \pi/2$ at both $J_1/J_2 = -1$ and 0.4. These J_1/J_2 parameters are in the decoupled C phase with QLRO($\pi/2$) rather than in a gapped IC phase.

We have presented numerical evidence for the quantum critical points $P2$ and $P3$ in Fig. 3.1 between gapped IC phases and a gapless decoupled phase with QLRO($\pi/2$). First, gs spin correlations yield the structure factor $S(q)$ whose peak q_G tracks energy degeneracy. The gs is non-degenerate with $q_G = \pi/2$ between $P2 = J_1/J_2 = -1.24$ and $P3 = J_1/J_2 = 0.44$ as shown in Table 3.1 and Fig. 3.3 using DMRG up to $N = 192$ spins. Second, level crossing discriminates between systems whose lowest excitation is a singlet or triplet. Exact level crossings in Fig. 3.5 up to $N = 28$ spins yield the same critical points as q_G. Third, the lowest triplet has $k_T = \pi/2$ and sublattices spin densities $\rho_A \neq \rho_B$ in the decoupled C phase. Fourth, gapless critical phases have divergent $S(q)$ peaks, with $q = \pi$ for $J_1/J_2 \geqslant P4 = 4.148$ in the familiar QLRO(π) phase and $q = \pi/2$ in the C phase between $P2$ and $P3$. Extrapolation to the thermodynamic limit is also required for the divergence of $S(\pi)$ or $S(\pi/2)$. The related models in section 3.8 are additional evidence for a decoupled phase with QLRO($\pi/2$) in spin-1/2 chains with non-interacting sublattices at $J_1 = 0$.

We mentioned in the Introduction that weak exchange J_1 between quantum systems presents challenges with some resemblance to dispersion forces that, for example, have been difficult to include in density functional theory. Methods that are suitable at small frustration J_2/J_1 may be less effective at small J_1/J_2. Field theories extend a finite energy gap to $J_1 = 0$ on the basis of RG flows. The continuum limit of the lattice is an approximation and there are other approximations as well. Field theory has not so far addressed level crossing of excited states, variable q_G of gs spin correlations in IC phases, spin densities of the lowest triplet or the magnitude of $S(q)$ peaks in connection with the critical points $P2$ and $P3$. We anticipate that the field theory of $J_1 - J_2$ model will eventually be as consistent with numerical results in the sector of small J_1/J_2 as it is for the critical point $P4$ and dimer phase at small J_2/J_1.

Bibliography

[1] C. K. Majumdar and D. K. Ghosh, J. Math. Phys. **10**, 1399 (1969).

[2] B. S. Shastry and B. Sutherland, Phys. Rev. Lett. **47**, 964 (1981).

[3] F. D. M. Haldane, Phys. Rev. B **25**, 4925 (1982).

[4] K. Kuboki and H. J. Fukuyama, Phys. Soc. Japan. **56**, 3126 (1987).

[5] T. Tonegawa and I. Harada, J. Phys. Soc. Japan. **56**, 2153 (1987).

[6] I. Affleck, T. Kennedy, E. H. Lieb, and H. Tasaki, Commun. Math. Phys. **115**, 477 (1988).

[7] T. Hamada, J. Kane, S. Nakagawa, and Y. Natsume, J. Phys. Soc. Japan. **57**, 1891 (1988).

[8] I. Affleck, D. Gepner, H. J. Schultz, and T. Ziman, J. Phys. A **22**, 511 (1989).

[9] K. Okamoto and K. Nomura Phys. Lett. A **169**, 433 (1992).

[10] R. Chitra, S. K. Pati, H. R. Krishnamurthy, D. Sen, and S. Ramasesha, Phys. Rev. B **52**, 6581 (1995).

[11] R. Bursill, G. A. Gehring, D. J. J. Farnell, J. B. Parkinson, T. Xiang, and C. Zeng, J. Phys.: Condens. Matter **7**, 8605 (1995).

[12] S. R. White and I. Affleck, Phys. Rev. B **54**, 9862 (1996).

[13] D. Allen and D. Sénéchal, Phys. Rev. B **55**, 299 (1997).

[14] C. Itoi and S. Qin, Phys. Rev. B **63**, 224423 (2001).

[15] M. Kumar, S. Ramasesha, and Z. G. Soos, Phys. Rev. B **81**, 054413 (2010).

[16] M. Kumar, Z. G. Soos, D. Sen, and S. Ramasesha, Phys. Rev. B **81**, 104406 (2010).

[17] A. W. Sandvik AIP Conf. Proc. **1297**, 135 (2010) and references therein.

[18] P. Lecheminant, *Frustrated Spin Systems* ed. by H. T. Diep (Singapore: World Scientific) p 307 ch 6 (2004).

[19] M. Hase, H. Kuroe, K. Ozawa, O. Suzuki, H. Kitazawa, G. Kido, and T. Sekine, Phys. Rev. B **70**, 104426 (2004).

[20] H. T. Lu, Y. J. Wang, S. Qin, and T. Xiang, Phys. Rev. B **74**, 134425 (2006).

[21] S. -L. Drechsler *et al.*, Phys. Rev. Lett. **98**, 077202 (2007).

[22] S. E. Dutton *et al.*, Phys. Rev. Lett. **108**, 187206 (2012).

[23] J. Sirker, V. Y. Krivnov, D. V. Dmitriev, A. Herzog, O. Janson, S. Nishimoto, S-L. Drechsler, and J. Richter, Phys. Rev. B **84**, 144403 (2011).

[24] J. Sudan, A. Lüscher, and A. M. Läuchli, Phys. Rev. B **80**, 140402(R) (2009).

[25] D. V. Dmitriev and V. Y. Krivnov, Phys. Rev. B **77**, 024401 (2008).

[26] T. Hikihara, T. Momoi, A. Furusaki, and H. Kawamura, Phys. Rev. B **81**, 224433 (2010).

[27] M. Kumar and Z. G. Soos, Phys. Rev. B **85**, 144415 (2012).

[28] S. Furukawa, M. Sato, S. Onoda, and A. Furusaki, Phys. Rev. B **86**, 094417 (2012).

[29] M. Kumar, A. Parvej, and Z. G. Soos, J. Phys.: Condens. Matter **27**, 316001 (2015).

[30] U. Schollwöck, T. Jolicoeur, and T. Garel, Phys. Rev. B **53**, 3304 (1996).

[31] K. Nomura and T. Murashima, J. Phys. Soc. Japan. **74**, S42 (2005).

[32] S. R White, Phys. Rev. Lett. **69**, 2863 (1992); Phys. Rev. B **48**, 10345 (1993).

[33] U. Schollwöck, Rev. Mod. Phys. **77**, 259 (2005); K. Hallberg, Adv. Phys. **55**, 477 (2006).

[34] D. Dey, D. Maiti, and M. Kumar, Papers in Phys. **8**, 080006 (2016).

[35] S. Ramasesha and Z. G. Soos, J. Chem. Phys. **80**, 3278 (1984).

[36] F. Woynarovich and H. -P. Eckle, J. Phys. A: Math. Gen. **20**, L97 (1987).

[37] L. D. Faddeev and L. A. Takhtajan, Phys. Lett. **85A**, 375 (1981).

[38] M. Shiroishi and M. Takahashi, J. Phys. Soc. Japan. **74**, S47 (2005).

[39] S. Todo and K. Sato, Phys. Rev. Lett. **87**, 047203 (2001).

[40] E. Lieb and D. Mattis, J. Math. Phys. **3**, 749 (1962).

[41] M. Kumar and Z. G. Soos, Phys. Rev. B **88**, 134412 (2013).

[42] A. Sandvik, Phys. Rev. Lett. **104**, 137204 (2010).

Chapter 4

Vector Chirality in the Frustrated $J_1 - J_2$ Spin-1/2 Chain

4.1 Introduction

Frustrated quantum spin systems have been a frontier area of extensive studies due to the existence of various exotic gs. The realization of low dimensional spin-1/2 systems such as edge-sharing chain cuprates like $(N_2H_5)CuCl_3$ [1], $LiCuSbO_4$ [2], and $LiCuVO_4$ [3], where quantum effects give rise to various interesting magnetic phases [3]. These magnetic systems are modeled by the isotropic $J_1 - J_2$ spin-1/2 model with J_1 AFM [4–13] or FM exchange interaction [14–19]. The isotropic $J_1 - J_2$ model in an axial magnetic field h is written in Eq. 1.18 in chapter 1 where $J_1 = -1$ and J_2 are NN and NNN exchange interaction strength, respectively. For an AFM J_2, competition between these two interaction parameters can lead to frustration [4–14, 16–20]. Systems with isotropic FM J_1 are relatively new and has not been studied extensively. The study of the above model in the presence of the axial magnetic field [21–25] is scant.

Recently synthesized one dimensional (1D) chain compounds, such as $LiCuSbO_4$, $LiCuVO_4$, Li_2CuZrO_4 [26] and quasi-1D like $Ba_3Cu_3In_4O_{12}$ and $Ba_3Cu_3Sc_4O_{12}$ [27, 28] have FM J_1 exchange interactions. These compounds are 1D in nature for temperature greater than 3K. Other compounds like Li_2CuZrO_4, $LiCuSbO_4$ and $LiCuVO_4$ also have low three dimensional ordering temperature T_{3D}, and their interaction strength ratios are $|\alpha| \sim 0.45$, 3.0 and about 0.25 respectively. Therefore, these compounds are suitable for studies of the exotic phases induced by the quantum fluctuations, which are observed at low temperature. Some of these compounds, e.g., $LiCu_2O_2$ show multiferroic behavior below a critical temperature [29].

In the last decade, though the $J_1 - J_2$ model with the FM J_1 in the absence of the magnetic field has been studied extensively [21–25], there is no agreement on the quantum phase diagram in the large $|\alpha|$ limit [13]. In this model the gs has FM phase with long range order for $|\alpha| < 0.25$ and a gapped dimer phase coexisting with a spiral phase for $|\alpha| > 0.25$ [17–20]. The quantum phase diagram of the model at the finite axial magnetic field is the playground of the exotic quantum phases [21–25]. Using bosonization procedure, Chubukov has suggested a uniaxial dimerized and a biaxial spin nematic phase in the gs [21], where the rotational symmetry is broken through the sites or the bonds, respectively [21]. Hikihara *et al.* used bosonization technique, the ED and the DMRG method to calculate the different phases in the presence of the axial magnetic field. The vector chiral (VC) and the multipolar phases are shown to exist in the presence of a finite magnetic field [22, 23]. Sudan *et al.* also showed the presence of the VC and the multipolar phases using the ED. The square of the VC order parameter and the structure factor are used to construct the quantum phase diagram [24]. In the earlier works, the quantum phase diagrams are constructed based on correlation functions, especially the VC phase [23–25], where the square of the order parameter and its related correlation functions are calculated.

In this chapter, we focus mainly on the degeneracies and the level crossings in the gs of the Hamiltonian and these degeneracies are also used to characterize the VC and the multipolar phases of the Hamiltonian H of Eq. 1.18. We also show that in the large $|\alpha|$ limit, the zigzag structure of the spin chain is responsible for a quadrupolar phase. This chapter is organized as follows: section 4.2 discusses about the VC phase, the multipolar phases and various broken symmetry states in those phases. Results are presented in section 4.3 and these results are discussed in section 4.4.

4.2 Vector Chiral and Multipolar Phases

The VC phase is an interesting phase with spontaneously broken spin parity and inversion symmetry [20]. The order parameter of this phase can be written as

$$\boldsymbol{\kappa}_{ij} = \langle \mathbf{S}_i \times \mathbf{S}_j \rangle, \tag{4.1}$$

where i, j are the neighboring sites. The spin current, $J_{ij}\kappa^z_{ij}$ can be derived from the equation of motion [23]. The z-component of the above can be defined as follows

$$\kappa^z_r = \langle \mathbf{S}_i \times \mathbf{S}_{i+r} \rangle^z = \frac{i}{2}\langle S^+_i S^-_{i+r} - S^-_i S^+_{i+r} \rangle, \tag{4.2}$$

where S^+_i and S^-_{i+r} are the spin raising and lowering operators at site i and $(i+r)$, respectively. The z-component of the above operator is just an anti-symmetric combination of bond order operators. For non-zero expectation values of the spin current, the Z_2 symmetry should be broken, i.e., the system chooses a particular direction of the spin current spontaneously [23]. The Z_2 symmetry can also be broken by applying the Dzyaloshinskii-Moriya (DM) interaction.

The spin parity of the Hamiltonian in Eq. 1.18 is not conserved for a non-zero S^z spin state in the presence of a high axial magnetic field. Therefore, to have the VC phase only inversion symmetry of the state with non-zero S^z should be broken. In these systems, spontaneous inversion symmetry is broken for doubly degenerate gs. The expectation value of the axial component of the order parameter, κ^z_r, spin current, as defined in Eq. 4.2 can be written as

$$\kappa^z_r = \langle \psi_+ | \left(\mathbf{S}_i \times \mathbf{S}_{i+r}\right)^z | \psi_- \rangle, \tag{4.3}$$

where $|\psi_+\rangle$ and $|\psi_-\rangle$ are the two degenerate gs with opposite inversion symmetry. The multipolar phases and chiral vector boundaries are determined on the basis of non-zero values of κ^z.

The existence of multipolar phases is an another interesting phenomenon in this model system. At $|\alpha| = 0.25$, the FM and the singlet gs cross each other [17] in the absence of the magnetic field. At $|\alpha| = 0.25$, a multi-magnon state with $p = N/2$ is stable where p is number of magnons condensed. In the neighborhood of the quantum critical point $|\alpha| = 0.25$, smaller p multi-magnon states with $p = 6, 5, 4, 3, 2$ are stable [23, 24]. All the higher p state phases are narrow compared to $p = 3$ and 2 as shown by Hikihara *et al.* [23] and Sudan *et al.* [24]. In this chapter, we concentrate on the triatic ($p = 3$) and the nematic ($p = 2$) phases. It is shown that the nematic phase is a Tomonaga-Luttinger liquid (TL) of hard core bosons with two magnon bound states. The Nematic phase is commensurate with momentum $q = \pi$, whereas incommensurate with its neighborhood. In these phases, both the boson propagator and the density-density correlation follow the power law decay [23]. One can define an $n-$type spin nematic order parameter [30] of this phase as

$$Q_{ij}^{\beta\gamma} = S_i^\beta S_j^\gamma + S_i^\gamma S_j^\beta - \frac{2}{3}\langle \mathbf{S}_i \cdot \mathbf{S}_j \rangle \delta_{\beta\gamma}, \tag{4.4}$$

where β and γ stand for x, y and z-component of the spin. As pointed out by Andreev and Grishchuk [31], and Hikihara *et al.* [23] that

$$\begin{aligned} Q_{ij}^{x^2-y^2} &= S_i^x S_j^x - S_i^y S_j^y, \\ Q_{ij}^{xy} &= S_i^x S_j^y + S_i^y S_j^x, \end{aligned} \tag{4.5}$$

$Q_{ij}^{x^2-y^2}$ and Q_{ij}^{xy} are thought to be the quadrupolar spin operators. As pointed out by Chubukov, the nematic order can be realized because of pairing of two-magnon excitations [21]. The nematic order parameter can be redefined as $Q_{ij}^{--} = Q_{ij}^{x^2-y^2} - iQ_{ij}^{xy} = S_i^- S_j^-$. Similarly, the order parameter of the higher order multipolar phases can also be redefined as octupolar triatic phase $S_i^- S_j^- S_k^-$, hexadecapolar quartic phase $S_i^- S_j^- S_k^- S_l^-$ etc. These phases have been shown to exist in the magnetization curve by Hikihara *et al.* [23] and Sudan *et al.* [24]. Starykh and Balents [32] has also shown the existence of the quadrupolar phase in this model. Using Q_{ij}^{--} as the order parameter, the quadrupolar phase can be characterized by the step $\Delta S^z = 2$ in the magnetization vs. magnetic field as shown in Fig. 4.8.

4.3 Results

In this chapter, we study the quantum phase diagram of the $J_1 - J_2$ model in the presence of an axial magnetic field. Symmetrized ED and DMRG methods [9] are used to calculate the various results presented here. In the conventional DMRG algorithm for the $J_1 - J_2$ model the superblock is constructed by using renormalized operator twice. The multiple times renormalized operator in constructing of superblock Hamiltonian operator leads to poor convergence and low accuracy of the eigenvalue and eigenvector. To avoid that we use a modified DMRG algorithm where four sites are added at every step. This algorithm is used to avoid usage of the twice renormalized operators in constructing superblock, therefore the convergence and efficiency of the DMRG method increase. It is shown that the gs converges faster by using the modified DMRG than the conventional DMRG [33–35]. We have used 500 eigenvectors of the density matrix and $4 - 5$ finite sweeps for our calculations. The truncation error of density matrix eigenvalues of the DMRG calculation is less than 10^{-14}. Accuracy of the energy gaps in the system is 3% whereas the accuracy of the correlation functions are less than 2%. The calculations are done for system sizes up to $N = 300$ with OBC. The ED method with inversion and spin parity symmetries are used to determine various energy level crossing points of the Hamiltonian up to 28 sites. All the calculations are done for the lowest state in each S^z manifold and their respective symmetry subspaces.

The VC order parameter can be directly calculated using the definition as shown in Eq. 4.3. This order parameter is the difference of two operators which are hermitian conjugate of each other. Therefore, the expectation values of operators

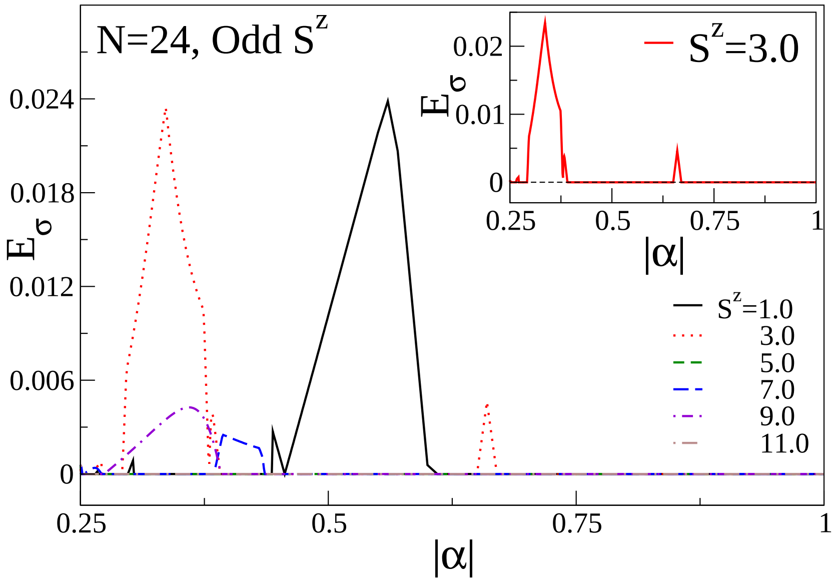

FIGURE 4.1: The lowest excited state gaps E_σ for odd S^z with the system size $N = 24$ are shown. Inset: The lowest excited state gap in a particular $S^z = 3.0$ sector for the system size $N = 24$.

are same in a non-degenerate state of the Hamiltonian in Eq. 1.18 in chapter 1. Let us consider that we have two degenerate states and the linear combination of these two states belonging from two different subspaces of symmetry space break the symmetry of the state. In that case, one can calculate the order parameter in the broken symmetry state. For example, a broken symmetry state which is linear combination of two degenerate states with different spin parity and inversion symmetries have non-zero VC order parameter $\boldsymbol{\kappa}$. At sufficiently high magnetic field, spin parity symmetry is broken for a gs with non-zero S^z. Therefore, to have non-zero VC order parameter $\boldsymbol{\kappa}$, inversion symmetry should also be broken in these states, which can be done by taking a linear combination of the degenerate gs with opposite inversion symmetry. To calculate κ_r^z doubly degenerate state $|\psi_+\rangle$ and $|\psi_-\rangle$ should be studied. To avoid the accuracy problem, in case of small excitation gaps and to separate the two different symmetry subspaces, ED method with inversion symmetry is used. We have calculated the lowest gaps $E_\sigma = E(\sigma = 1) - E(\sigma = -1)$ where $E(\sigma = 1)$ and $E(\sigma = -1)$ are the lowest eigenvalues in a S^z sector with inversion subspace $\sigma = +$ and $\sigma = -$, respectively, for different system sizes.

Fig. 4.1 shows the lowest excited state gaps E_σ for odd S^z sectors as a function of $|\alpha|$ with the system size $N = 24$. The inset of the Fig. 4.1 shows E_σ for $S^z = 3$. We notice that there are multiple energy level crossings between $|\alpha| = 0.26$ and 0.67. These crossings are at 0.261, 0.293, 0.391, 0.65, and 0.67. There is continuous degeneracy of energy levels from $|\alpha| = 0.391$ to 0.65 and $|\alpha| > 0.67$. In the odd S^z sector, there are energy level crossovers between the two fold degenerate states with a non-degenerate state. The zero gap represents continuous degeneracies in the gs. We notice that for smaller $|\alpha| < 0.7$, low S^z states are degenerate at multiple values of $|\alpha|$. The multiple degeneracies for different values of the S^z correspond to the multiple energy levels crossing. These multiple degeneracies are due to the spiral arrangement of the spins. Earlier, it has been shown that spiral phase sets in the systems for $|\alpha| > 0.25$ at magnetic field $h = 0$ [20]. For finite

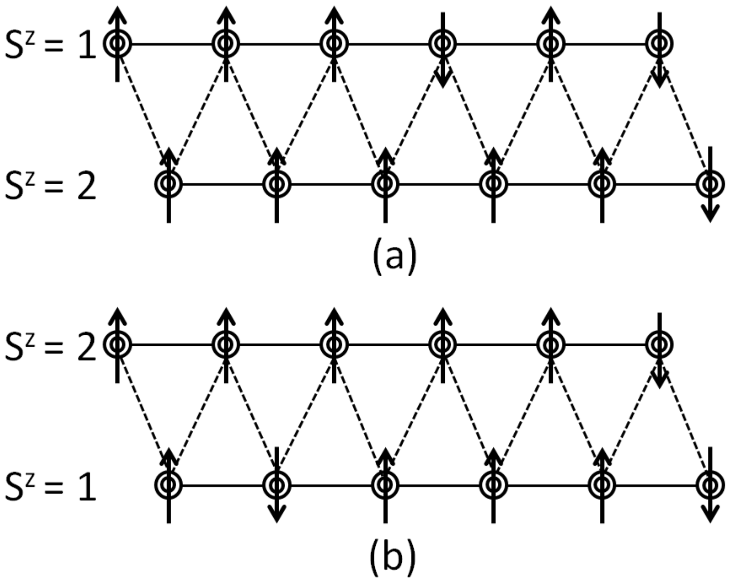

FIGURE 4.2: In the large $|\alpha|$ limit, Fig. 4.2 (a) and (b) show the spin arrangements in the two degenerate states in the $S^z = 3.0$ sector for the system size $N = 12$.

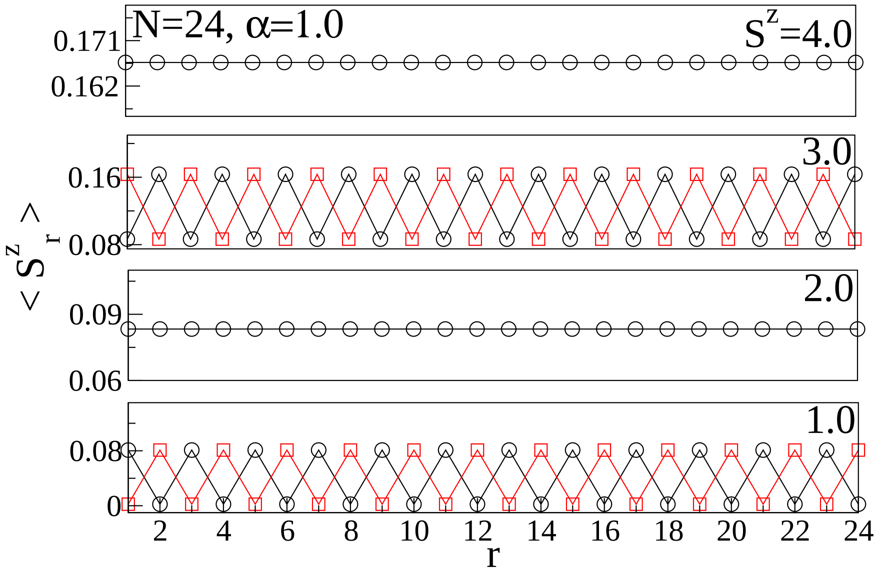

FIGURE 4.3: Spin densities of the gs for different low S^z sectors are shown. In even S^z sectors, spin density of only non-degenerate gs are shown, whereas, spin densities of both the degenerate gs in the odd S^z sectors are shown.

system size, the energy levels become degenerate if the wavelength of the spiral spin wave is commensurate with system size.

For large $|\alpha|$ limit, the above 1D chain can be mapped into a zigzag chain like structure as shown in Fig. 4.2. Degeneracies in the odd $S^z = 2p + 1$ state can be explained in terms of nearly decoupled phase of the zigzag chain. We notice that the $2p$ spin densities are equally distributed on both the legs, but extra $S^z = 1$ is localised either on upper arm of one state or on the lower arm of second state, as shown in Fig. 4.2 (a) and (b).

To verify the hypothesis, spin density in the gs for $S^z = 1, 2, 3,$ and 4 manifolds is calculated for $N = 24$ system size as shown in Fig. 4.3. The spin densities of degenerate states with odd $S^z = 1, 3$ and non-degenerate states with $S^z = 2, 4$ are shown. We notice the spin densities are equally distributed on each leg of the zigzag chain. For $S^z = 1$, almost 99.9% of the spin density is concentrated either on the upper leg for one state or on the lower leg in case of the second state. For $S^z = 3$ sector, two magnons are confined on the upper leg and one on the lower

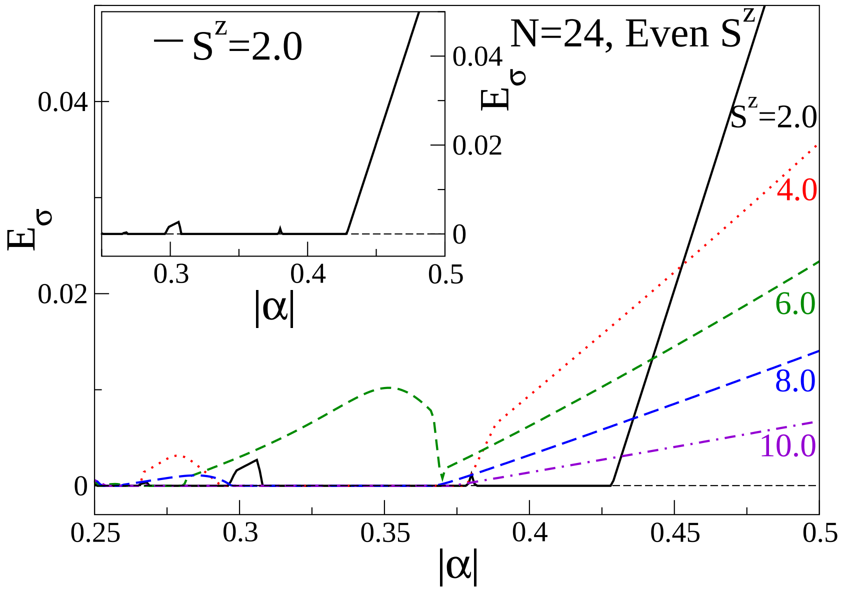

Figure 4.4: The lowest excited state gaps E_σ for even S^z with system size $N = 24$ are shown. Inset: The lowest excited state gap in a particular $S^z = 2.0$ sector for the system size $N = 24$.

leg in one state, whereas one magnon on the upper leg and two on the lower leg in the second state.

Similarly, Fig. 4.4 shows the lowest excited state gaps E_σ for even S^z sectors as a function of $|\alpha|$ for $N = 24$. The inset of the Fig. 4.4 shows E_σ for $S^z = 2$. Clearly E_σ in this S^z sector shows a similar pattern to that of the odd sectors in small $|\alpha|$ limit. The energy level crossings are at $|\alpha| = 0.267, 0.272, 0.296, 0.308, 0.378, 0.381,$ and 0.428. There are continuous degeneracies from 0.308 to 0.378 and 0.381 to

Table 4.1: Last energy levels crossing points $|\alpha_c|$ for different system sizes N in the even S^z sectors are shown.

S^z	$N(16)$	$N(20)$	$N(24)$	$N(28)$
2	0.394	0.412	0.428	0.440
4	0.375	0.376	0.378	0.380
6	0.370	0.368	0.370	0.373
8	-	0.372	0.367	0.367
10	-	-	0.373	0.370
12	-	-	-	0.374

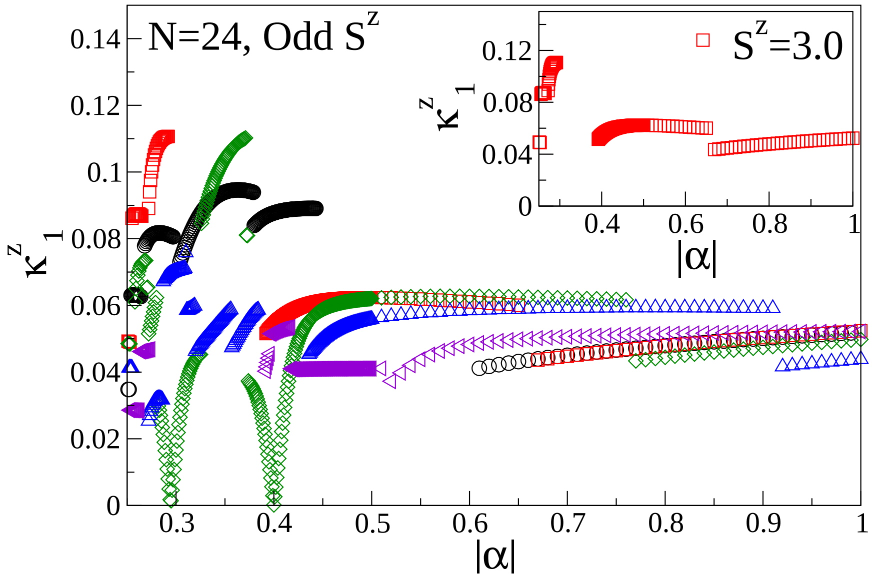

FIGURE 4.5: Expectation values of κ^z in the odd S^z sectors as a function of $|\alpha|$ with system size $N = 24$ are shown. Values of κ^z are calculated only at degenerate points. Inset: The expectation values of κ^z at a particular $S^z = 3.0$ sector as a function of $|\alpha|$ are shown. Black circle, red square, green diamond, blue triangle up, violet left triangle represent $S^z = 1, 3, 5, 7, 9$, respectively.

0.428, because of degenerate gs. In the large $|\alpha|$ limit, E_σ is finite in even S^z sectors, whereas, it is degenerate in even S^z sectors for $|\alpha| > |\alpha_c|$. The $|\alpha_c|$ decreases with increasing values of S^z.

In Table 4.1, the last energy level crossing points $|\alpha_c|$ for even S^z sectors are listed. The ED calculations of system size up to $N = 28$ show weak system size dependence of $|\alpha_c|$ for larger S^z. The $|\alpha_c|$ for system size $N = 28$ in $S^z = 8, 10$, and 12 manifolds are $0.367, 0.370$, and 0.374, respectively. Below $|\alpha_c|$, the first excited state and gs are related by inversion symmetry. Therefore, in these parameter limits, the gs becomes degenerate in the thermodynamic limit. Using these degenerate states broken symmetry states can be constructed, and the VC order parameter is non-zero in this broken symmetry state.

The expectation value of the z-component of the chiral vector order parameter, $\boldsymbol{\kappa}$, is calculated at degenerate points using the Eq. 4.3. For the system size $N = 24$,

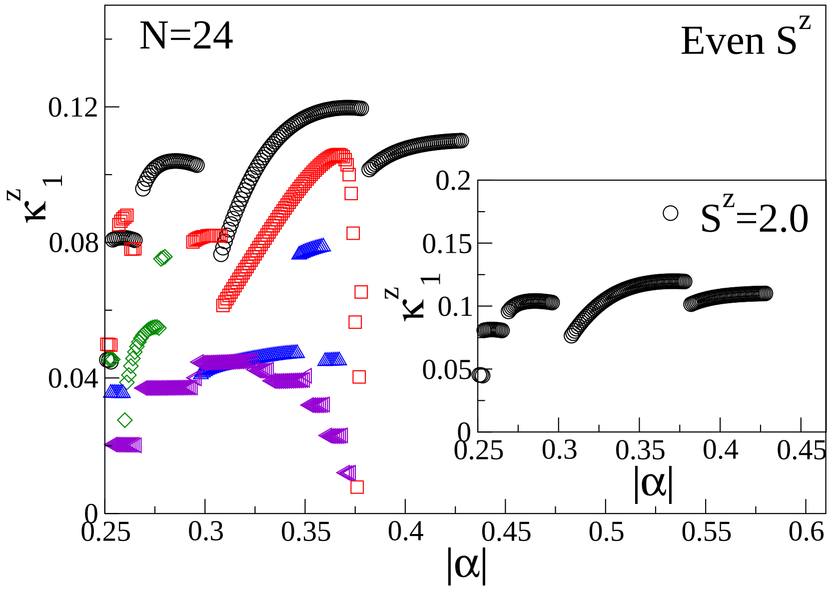

FIGURE 4.6: Expectation values of κ^z in the even S^z sectors as a function of $|\alpha|$ with the system size $N = 24$ are shown. Values of κ^z are calculated only at degenerate points. Inset: The expectation values of κ^z at a particular $S^z = 2.0$ sector as a function of $|\alpha|$ are shown. Black circle, red square, green diamond, blue triangle up, violet left triangle represent $S^z = 2, 4, 6, 8, 10$, respectively.

κ^z for odd S^z sectors are shown in the Fig. 4.5. In the inset of this figure, κ^z as a function of $|\alpha|$ for $S^z = 3$ is shown. κ^z is not a continuous function of $|\alpha|$ because of the energy level crossings. The sudden jumps in κ^z are due to symmetry crossover of lowest states. As shown in the inset, κ^z is continuous for $|\alpha|$ in between 0.392 and 0.66, and $|\alpha| > 0.67$. The energy levels in these intervals are doubly degenerate, as shown in the inset of Fig. 4.1, and the discontinuity in the κ^z at $|\alpha| = 0.66$ is because of energy levels crossing. We notice that the variation of κ^z with the system size is weak. In the main Fig. 4.5, values of κ^z, between $|\alpha| = 0.25$ and 0.4, are relatively high for smaller S^z. In the large $|\alpha|$ limit κ^z in all the odd S^z sectors decrease weakly with $|\alpha|$ and finally go to zero in the decoupled phase.

The κ^z for all the even S^z is shown in Fig. 4.6. The κ^z for the $S^z = 2$ is shown in the inset of the Fig. 4.6. The κ^z is discontinuous at four values of $|\alpha|$ and all the discontinuities occur at the energy level crossing points. We notice that the discontinuity point coincides with the energy levels crossing in the inset of Fig.

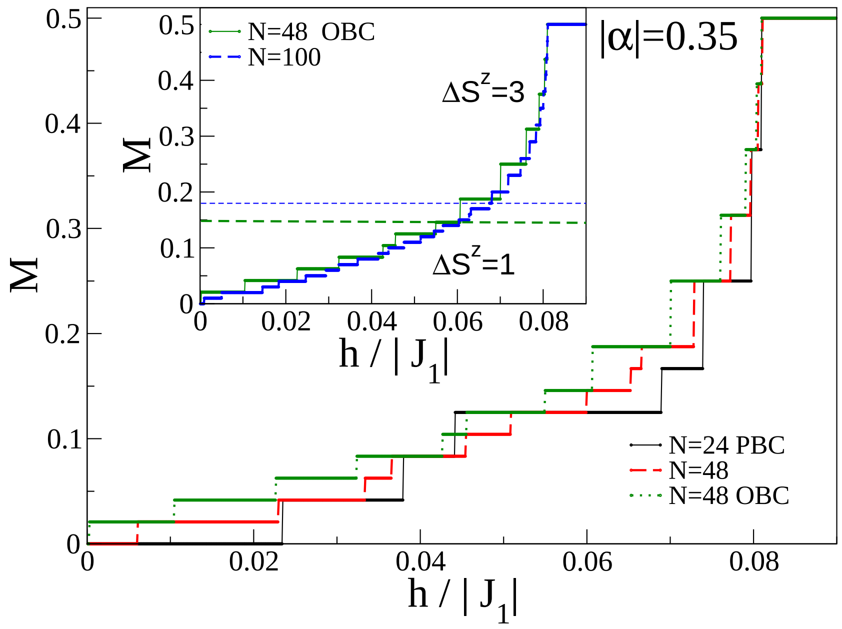

FIGURE 4.7: Magnetization vs. axial magnetic field h for $|\alpha| = 0.35$ is shown. The calculations are done for system sizes $N = 24$ and 48 for the PBC and $N = 48$ for OBC. Inset: The M vs. h for the $N = 48$ and 100 for OBC are shown.

4.4. κ^z of $S^z = 2$ is confined between $|\alpha| = 0.25$ and $|\alpha| \approx 0.45$, whereas this extends to higher values of $|\alpha|$ for $S^z = 3$. The main Fig. 4.6 shows that for all the even sectors of S^z non-zero values of κ^z are confined below $|\alpha| = 0.5$ for the system size $N = 24$. Similar to odd S^z sector, values of κ^z in the small $|\alpha|$ limit are larger for smaller S^z. As we have stated earlier, κ^z is the order parameter for the VC phase, therefore, depending on the values of S^z of the gs in the strong magnetic field h, the VC phase can be confined to less than 0.45 or extended to large values of $|\alpha|$ for even or odd S^z, respectively.

To understand the multipolar phases and value of S^z in the applied axial field at absolute zero temperature, we calculate the magnetization as a function of axial magnetic field h ($M-h$ plot) shown in Fig. 4.7 and 4.8 for $|\alpha| = 0.35$ and $|\alpha| = 0.8$, respectively. In the main Fig. 4.7, $M-h$ curve is shown for $N = 24$, 48 with PBC and for $N = 48$ with OBC. The inset shows $M-h$ curve for the OBC case with system sizes $N = 48$ and 100 with thicker and thinner lines, respectively. For

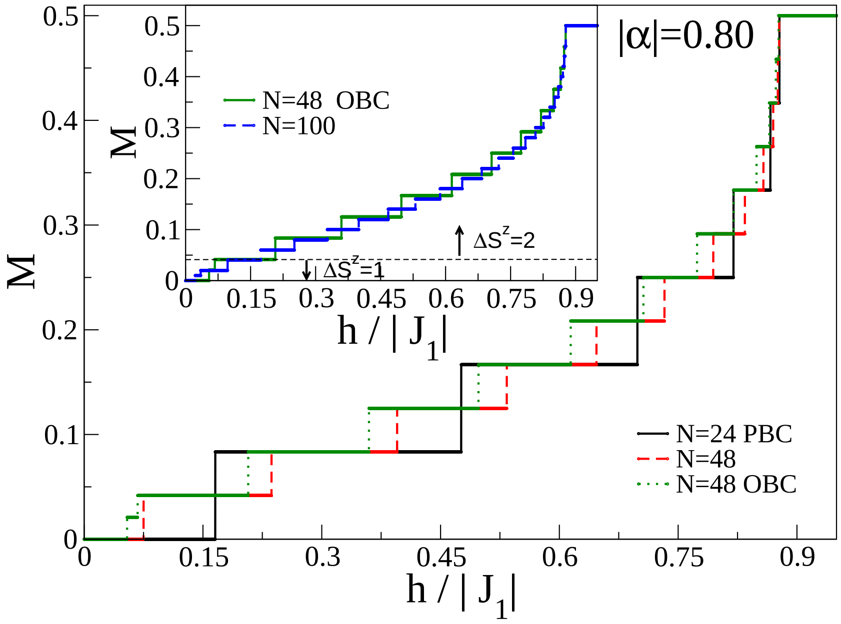

FIGURE 4.8: Magnetization vs. axial magnetic field h for $|\alpha| = 0.60$ for system sizes $N = 24$ and 48 for the PBC and $N = 48$ for OBC is shown. The inset shows M vs. h for the $N = 48$ and 100 for OBC is shown.

$|\alpha| = 0.35$, in PBC case, first few steps in the magnetization are $\Delta S^z = 1$ and afterwards the steps are $\Delta S^z = 3$. The dotted line indicates the boundary of VC ($\Delta S^z = 1$) and triatic phases ($\Delta S^z = 3$). The OBC system also has the similar trend as that of the PBC, except that the magnetic field required in case of OBC is lower than that for PBC case. As shown in the inset of Fig. 4.7, magnetization step ΔS^z is one up to $S^z = 7$ ($M = 0.15$) and $S^z = 18$ ($M = 0.18$) for system sizes $N = 48$ and 100, respectively. The dotted line indicates the boundary of step of one and three. We notice that these steps are associated with the finite binding energies of three magnons in the thermodynamic limit. Therefore, these steps are finite in the triatic phase, even in the thermodynamic limit.

The magnetization M with different h, at $|\alpha| = 0.8$, is shown in the Fig. 4.8. Main figure shows the $M - h$ curve for both PBC with $N = 24$ and 48 and OBC with $N = 48$. In OBC system, magnetization start with step of one for S^z below 2 and the step of 2 for $S^z > 2$. These steps in the PBC systems, are always two. Inset of Fig. 4.8 shows that first two steps are one in the magnetization curve. The inset

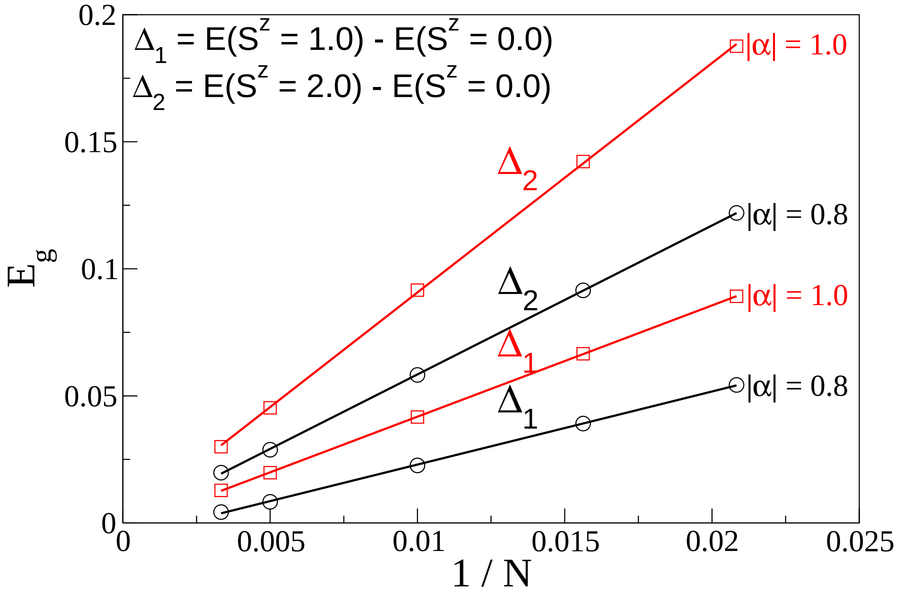

FIGURE 4.9: For two values of $|\alpha| = 0.8$ and 1.0, Δ_1 and Δ_2 are extrapolated where, $\Delta_1 = E(S^z = 1) - E(S^z = 0)$ and $\Delta_2 = E(S^z = 2) - E(S^z = 0)$, where $E(S^z = 0)$, $E(S^z = 1)$, and $E(S^z = 2)$ are the lowest states in the $S^z = 0, 1,$ and 2, respectively.

of Fig. 4.8 shows the magnetization for two systems $N = 48$ and 100 for an OBC systems. Similar to triatic phase, quadrupolar phase also has steps of two and is associated with the binding energies of two magnons [36]. The binding energies are finite and largest for $|\alpha| \approx 1$ at finite magnetic field.

For $|\alpha| = 0.8$, step of one in OBC and PBC systems behave differently. In the infinite size systems, these differences should not be there. To resolve the issue, we have extrapolated the gaps $\Delta_1 = E(S^z = 1) - E(S^z = 0)$ and $\Delta_2 = E(S^z = 2) - E(S^z = 0)$, where $E(S^z = 0)$, $E(S^z = 1)$, and $E(S^z = 2)$ are the lowest states in the $S^z = 0, 1,$ and 2 spin sectors, respectively. In Fig. 4.9, Δ_1 and Δ_2 are shown as a function of $1/N$ for $|\alpha| = 0.8$ and $|\alpha| = 1.0$. Extrapolated values of Δ_1 and Δ_2 are smaller than the accuracy limit of our calculations. Therefore, in the infinite systems for $|\alpha| > 0.8$, one can see only steps of two in both PBC and OBC case. The extrapolated PBC and OBC results are consistent with each other.

At $|\alpha| = 0.25$ our calculations show a magnetization step of $N/2$ which is consistent

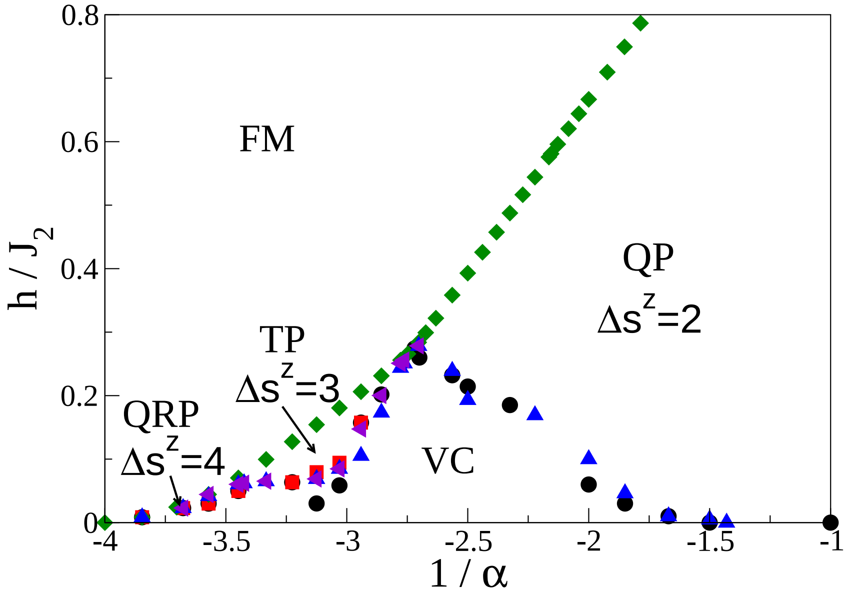

FIGURE 4.10: The quantum phase diagram of $J_1 - J_2$ model in the axial magnetic field is shown. Phase boundaries are obtained using OBC and PBC calculations. FM, QP, TP, and QRP represent ferromagnetic, quadrupolar, triatic, and quartic phase, respectively. Boundary represented by circle and triangle are calculated from PBC and OBC, respectively.

with the earlier calculations [17]. In this limit system goes from a fully polarized state $S^z = N/2$ to singlet gs. We also find that increasing $|\alpha|$, the value of multipolar order p decreases, which is consistent with earlier results [23–25]. Our results for finite system sizes with OBC show that for $|\alpha| > 0.8$, steps are always in steps of 2. Our DMRG calculation for system size up to 48 sites with PBC show that the gs for $|\alpha| > 0.54$ is always in sectors with even S^z in the presence of the axial magnetic field.

Based on the degeneracy and the magnetization steps, the quantum phase diagram is shown in the Fig. 4.10. Our quantum phase diagram in $h - \alpha$ parameter space agrees with the existence of multipolar phases with $p = 2, 3$ and 4. The VC phase is confined to low magnetization, whereas the multipolar phase is a stable phase at higher magnetic field. For $N = 24$ calculation shows that the degenerate gs has always magnetization step of one, i.e., $\Delta S^z = 1$. Therefore, the coexistence of the VC and the multipolar phases are avoided. Our phase boundaries of the quantum phase diagram, for $|\alpha| < 0.5$ are similar to what Hikihara *et al.* found. As stated earlier, the VC phase for the finite system is bounded by $|\alpha_c|$ values listed in Table 4.1. We notice that for an accurate $|\alpha_c|$ value, large system calculations are required. The boundary obtained from energy level crossing in finite N is $|\alpha_c| \approx 0.54$, whereas from magnetization step in large N also gives very similar phase boundary at $|\alpha| \approx 0.8$.

For large values of $|\alpha|$ in OBC, the finite size effect is dominant. A finite system with PBC and OBC have different phase boundaries, but extrapolated values of the phase boundaries of the VC and the quadrupolar phases are same. We notice that for $0.31 < |\alpha| < 0.37$, the boundaries of the VC and the triatic phases are mediated by the small region of the quadrupolar phase.

4.4 Discussion

Numerical study of the isotropic $J_1 - J_2$ model with FM J_1 and AFM J_2 exchange interaction in the axial magnetic field h is done. In this system, Z_2 symmetry is spontaneously broken in the presence of the axial magnetic field [23–25]. In earlier studies, the VC phase has been characterized based on various kinds of correlation functions like current-current correlation function and scalar chiral correlation etc. The scalar chiral vector (SCV) operator involves three spin operators. The z-component of an SCV operator $\mathbf{S_i} \cdot (\mathbf{S_j} \times \mathbf{S_k})$ can be written as $S_i^z(S_j^+ S_k^- - S_j^- S_k^+)$ [37]. The characterization of VC phase based on the SCV correlation can be misleading in a finite size system. Our calculations suggest that this correlation function in a finite system can be non-zero even in the absence of the VC phase. The order parameter $\boldsymbol{\kappa}$ can be calculated using the broken symmetry states in this model, and it is shown for the first time that there are degeneracies in the lower states of $S^z \neq 0$. A large number of level crossing occur at different values of $|\alpha|$ in the presence of spiral phase or chiral phase in the system. The broken symmetry state is constructed using degeneracies in the gs to characterize the VC phase. The calculation of $\boldsymbol{\kappa}$ can be useful in calculating the electronic polarization $\mathbf{P} \propto \boldsymbol{\kappa}$ in the improper multi-ferroic materials such as $LiCuVO_4$ [3, 4].

These frustration induced degeneracies in the gs of the Hamiltonian are very similar to the degeneracy in the spiral phase of AFM-AFM spin-1/2 chain model [10]. These two states are related through inversion symmetry, same as that of the gs of the MG model [4]. There are two prominent reasons for degeneracy; first, because of the spiral like arrangement of spin where degeneracy occurs, in finite system, when spiral wavelength is commensurate with the system size, and second, in the large $|\alpha|$ limit, the zigzag chain behaves like two decoupled chains and for odd number $2p + 1$ of magnon excitation, p number of magnons confined to each leg and extra magnon can be confined to any one of the two legs. Therefore, the gs becomes degenerate to let magnon to be confined in either upper leg or lower leg as shown in Fig. 4.2. We find the second type of degeneracy which is continuous in nature even in the finite system. In the decoupled limit, the lowest excitation is triplet excitation on each leg. In this limit, $2\Delta_1$ is larger than Δ_2, therefore $M - h$ plot shows steps of 2.

We have constructed a new quantum phase diagram using ED and modified DMRG results. Our results agree with the existing phase diagram below $|\alpha| < 0.5$ [23–25]. Contrary to earlier results which show the existence of the VC in low magnetic field and the quadrupolar phase in the high magnetic field [23], our results suggest that for $|\alpha| > 0.8$, only quadrupolar phase exists. These conclusions are based on various criteria such as the magnetic step, the energy level crossings, and the order parameters etc. The magnetic step in our calculations is always $\Delta S^z = 2$ for $|\alpha| > 0.8$, whereas the existing results show $\Delta S^z = 1$ for low field h. The excitation gaps have large finite size effect at low field and earlier studies lack the finite size scaling [23]. The last energy level crossing point is another criterion, below the last crossing points both levels become degenerate and give rise to VC phase. The energy level crossing points are shown in Table 4.1. We notice that the last energy level crossing point for smaller S^z have large finite size effect and underestimate the VC-quadrupolar phase boundary. On the basis of the above results, we conclude that the VC phase exists only in the narrow range of the parameter space $\alpha - h$.

In conclusion, using the ED and the modified DMRG results, a new quantum phase diagram of the $J_1 - J_2$ model in presence of the axial magnetic field is constructed and VC phase is shown to exist only in the narrow range of parameter space. The main focus of this chapter is to show the degeneracies in lowest states in different S^z manifold of the Hamiltonian. Broken symmetry states are constructed using these degenerate gs to calculate the VC order parameters. In the large $|\alpha|$ limit, frustration induced degeneracies in the odd S^z sectors are studied in detail.

Bibliography

[1] N. Maeshima, M. Hagiwara, Y. Narumi, K. Kindo, T. C Kobayashi, and K. Okunishi, J. Phys.: Condens. Matter **15**, 3607 (2003).

[2] S. E. Dutton, M. Kumar, M. Mourigal, Z. G. Soos, J. -J. Wen, C. L. Broholm, N. H. Andersen, Q. Huang, M. Zbiri, R. Toft-Petersen, and R. J. Cava, Phys. Rev. Lett. **108**, 187206 (2012).

[3] M. Mourigal, M. Enderle, B. Fåk, R. K. Kremer, J. M. Law, A. Schneidewind, A. Hiess, and A. Prokofiev, Phys. Rev. Lett. **109**, 027203 (2012).

[4] C. K. Majumdar and D. K. Ghosh, J. Math. Phys. **10**, 1388 (1969).

[5] I. Harada and T. Tonegawa, J. Magn. Magn. Mater **90 & 91**, 234-236 (1990).

[6] S. R. White and I. Affleck, Phys. Rev. B **54**, 9862 (1996); R. Chitra, S. Pati, H. R. Krishnamurthy, D. Sen, and S. Ramasesha, Phys. Rev. B **52**, 6581 (1995).

[7] C. Itoi and S. Qin, Phys. Rev. B **63**, 224423 (2001).

[8] M. Kumar, S. Ramasesha, D. Sen, and Z. G. Soos, Phys. Rev. B **75**, 052404 (2007).

[9] M. Kumar, Z. G. Soos, D. Sen, and S. Ramasesha, Phys. Rev. B **81**, 104406 (2010).

[10] M. Kumar, S. Ramasesha, and Z. G. Soos, Phys. Rev. B **81**, 054413 (2010).

[11] A. W. Sandvik, AIP Conf. Proc. **135**, 1297 (2010) and references therein.

[12] M. Kumar and Z. G. Soos, Phys. Rev. B **88**, 134412 (2013).

[13] M. Kumar, A. Parvej, and Z. G. Soos, arXiv:1405.1578 (2014), M. Kumar, A. Parvej, and Z. G. Soos, J. Phys.: Condens. Matter **27**, 316001 (7pp) (2015).

[14] F. Heidrich-Meisner, A. Honecker, and T. Vekua, Phys. Rev. B **74**, 020403R (2006).

[15] B. Danu, B. Kumar, and R. V. Pai, Europhys. Lett. **100**, 27003 (2012).

[16] I. P. McCulloch, R. Kube, M. Kurz, A. Kleine, U. Schollwöck, and A. K. Kolezhuk, Phys. Rev. B **77**, 094404 (2008).

[17] D. V. Dmitriev and V. Ya. Krivnov, Phys. Rev. B **73**, 024402 (2006).

[18] J. Sirker, Phys. Rev. B **81**, 014419 (2010).

[19] S. Mahdavifar, J. Phys.: Condens. Matter **20**, 335230 (2008).

[20] M. Kumar and Z. G. Soos, Phys. Rev. B **85**, 144415 (2012).

[21] A. V. Chubukov, Phys. Rev. B **44**, 4693 (1991).

[22] L. Kecke, T. Momoi, and A. Furusaki, Phys. Rev. B **76**, 060407R (2007).

[23] T. Hikihara, L. Kecke, T. Momoi, and A. Furusaki, Phys. Rev. B **78**, 144404 (2008).

[24] J. Sudan, A. Lüscher, and A. M. Läuchli, Phys. Rev. B **80**, 140402(R) (2009).

[25] F. Heidrich-Meisner, I. P. McCulloch, and A. K. Kolezhuk, Phys. Rev. B **80**, 144417 (2009).

[26] S. -L. Drechsler, O. Volkova, A. N. Vasiliev, N. Tristan, J. Richter, M. Schmitt, H. Rosner, J. Málek, R. Klingeler, A. A. Zvyagin, and B. Büchner, Phys. Rev. Lett. **98**, 077202 (2007).

[27] S. E Dutton, M. Kumar, Z. G Soos, C. L Broholm, and R. J Cava, J. Phys.: Condens. Matter **24**, 166001 (2012); M. Kumar, S. E Dutton, R. J Cava, and Z. G Soos, J. Phys.: Condens. Matter **25**, 136004 (2013).

[28] O. S. Volkova, I. S. Maslova, R. Klingeler, M. Abdel-Hafiez, Y. C. Arango, A. U. B. Wolter, V. Kataev, B. Büchner, and A. N. Vasiliev, Phys. Rev. B **85**, 104420 (2012).

[29] S. Park, Y. J. Choi, C. L. Zhang, and S. W Cheong, Phys. Rev. Lett. **98**, 057601 (2007).

[30] N. Shannon, T. Momoi, and P. Sindzingre, Phys. Rev. Lett. **96**, 027213 (2006).

[31] A. F. Andreev and I. A. Grishchuk, Sov. Phys. JETP **60**, 267 (1984).

[32] O. A. Starykh and L. Balents, Phys. Rev. B **89**, 104407 (2014).

[33] S. R. White, Phys. Rev. Lett. **69**, 2863 (1992).

[34] S. R White Phys. Rev. B **48**, 10345 (1993).

[35] K. Hallberg, Adv. in Phys. **55**, 477 (2006); U. Schollwöck, Rev. Mod. Phys. **77**, 259 (2005).

[36] M. E. Zhitomirsky and H. Tsunetsugu, Eur. Phys. Lett. **92**, 37001 (2010).

[37] K. A. Al-Hassanieh, C. D. Batista, G. Ortiz, and L. N. Bulae-vskii, arXiv:0905.4871 (unpublished).

Chapter 5

Study of Multipolar Phase in the Spin-1/2 Chain

5.1 Introduction

Interaction induced frustration and confinement of electrons in a one dimensional (1D) magnetic system generates many exotic phases [1–4]. Some of these phases can have well defined order parameters, whereas other phases can have hidden order parameter. The 1D spin-1/2 systems with an isotropic $J_1 - J_2$ model [5–21] in the presence of an axial magnetic field h have been extensively studied [2–5, 22–26]. The $J_1 - J_2$ model in an axial magnetic field h is shown in Eq. 1.18 in chapter 1 where J_1 and J_2 are NN with FM and NNN AFM exchange interactions, respectively. The ratio of NN and NNN is defined as $\alpha = J_2/J_1$ in chapter 1.

The model with a FM J_1 shows many interesting phases like spin liquid [5–9], dimer [5–9], chiral vector [1, 27], spin multipolar [3, 4], decoupled phase [8]. The spin liquid phase is gapless and possesses quasi-long range order [9, 14]. The dimer phase is gapped in nature, and the spin-spin correlation decays exponentially [9, 14, 17]. This model has been extensively used for modeling the magnetization properties of $LiCuSbO_4$ [28], $LiCu_2O_2$ [29], $Rb_2Cu_2Mo_3O_{12}$ [30], Li_2CuZrO_4 [31], $Ba_3Cu_3In_4O_{12}$, and $Ba_3Cu_3Sc_4O_{12}$ [32, 33]. In the chiral vector phase, both spin parity and inversion symmetry are spontaneously broken [34]. This phase has been studied extensively because of its potential application in improper multiferroic systems [35, 36].

The field theoretical and numerical studies by Hikihara *et al.* suggest that metamagnetic or spin multipolar phase exist in the presence of the high axial magnetic field h for FM J_1 [3]. These multipolar phases have hidden order parameters. In this model multipoles of order p depend on the J_2/J_1 ratio [3, 4], and the nomenclature of each phase is done based on the number of bound magnons in the systems i.e., the number of paired magnons p in dipolar, quadrupolar, octupolar and hexadecapolar phases are $1, 2, 3, 4$, respectively. The quadrupolar phase is a Tomonaga-Luttinger liquid of hard core bosons [3], and each boson is made up of two magnons. In this phase, the correlations between bosons and density fluctuations follow a power law. However, the boson propagator is dominant over the density fluctuations in this phase [3]. In his seminal work Chubukov predicts that this phase has dimerized gs [1], but Hikihara *et al.* show the absence of dimerization [3]. In the large J_2/J_1 regime, field theoretical calculations show that the SDW_2 phase exists in low magnetic field, whereas SN phase exists in the narrow range of magnetic field near the saturation field [3]. The numerical calculations in $|\alpha| > 0.6$ show the finite binding energy of magnon even for a small field h [27].

The order parameter of the SN phase $\langle S_i^+ S_{i+1}^+ \rangle$ is defined in Refs. [1, 37, 38]. It is hidden in nature, although the probes like the INS [28, 39] and the resonant inelastic X-Ray scattering (RIXS) [40] methods can indirectly measure these phases. The nematic phase in $\mathrm{LiCuVO_4}$ compound is confirmed by using the INS data of dynamical structure factor [39], and NMR data of this compound shows a sharp single and solitary line which moves with magnetic field [41, 42]. There is a characteristic feature of INS measurement for the SDW_2 and SN phase.

In this model, there are many unsettled issues such as the metamagnetic phase in the small J_2/J_1 regime has been completely unexplored, and is difficult to characterize because of very small gaps. We have shown the gs degeneracies in the odd S^z sectors [27], but dimer order parameter B is vanishingly small in this sector. The existence of quadrupolar phase in spin-1 systems is controversial, as steps of two in the $M-h$ curve is absent [43, 44], whereas the other studies for general spin show the existence of this phase. We explore this phase for the spin-1 system using the Hamiltonian in Eq. 1.18.

We use modified DMRG algorithm, where four new sites are added to avoid the multiple time of renormalization of operators in the superblock which is already discussed in chapter 2. The modified DMRG has better convergence and also has sparse Hamiltonian matrix of superblock for the model Hamiltonian in Eq. 1.18, compared to the conventional DMRG where only one site is added in each block at every step [16]. The number of eigenvectors of the density matrix retained up to $m = 400$ to maintain the truncation error of density matrix eigenvalues less than 10^{-10}. In the worst case error in the energy is less than 0.01%. The DMRG is used for calculating various properties of large system sizes up to $N = 368$ chain with OBC. The number of finite DMRG sweeps required for an accurate gs and spin correlation function in the different S^z sectors is approximately 20. Recently developed PBC algorithm is also employed for calculating the accurate gs and the correlation functions [45].

The rest of the chapter goes in the following sequence. Results are discussed in section 5.2. We start with the higher order multipolar phase and the relation between the pitch angle θ and magnetization M is discussed in subsection 5.2.1. The quadrupolar phase is discussed thereafter. The dimer phase in the SN/SDW$_2$ phase is presented in the subsection 5.2.2. The results for spin-1 for the same model are discussed in section 5.3. The discussion of all the results is done in the next section 5.4.

5.2 Results

The quantum phase diagram of the $J_1 - J_2$ model in an axial magnetic field given in Eq. 1.18 consists of numerous phases such as the vector chiral (VC) [1, 27], the dimer [5–10, 12–21], the decoupled chain [8, 18], and multipolar/SDW$_n$ phases

[3, 4]. In this work, the SN/SDW$_2$ phase and other higher order multipolar phases are discussed. This section is divided into three subsections. In subsection 5.2.1, multipolar phases for spin-1/2 are discussed in the beginning; SN/SDW$_2$ phase is presented in the later part of subsection 5.2.1. The coexistence of dimer and SN/SDW$_2$ phase is presented in subsection 5.2.2.

5.2.1 Multipolar Phases in $S = 1/2$

The multipolar phase and the spin density wave in the $J_1 - J_2$ model for a spin-1/2 chain in the presence of magnetic field h are discussed in this part. We notice that there is a level crossing from FM to singlet gs at $|\alpha_c| = 0.25$ [6], and near to the critical point $|\alpha_c|$, but $|\alpha| > 0.25$ limit, multiple magnons bind to form multipoles below the saturation magnetic field. It is also noted that the number of p changes rapidly with $|\alpha|$. In this chapter, multipolar phase with order p is explored based on the magnetic steps, pitch angle θ of spin density, and spin correlations in the gs at a finite magnetic field h. The angle between two nearest neighbor spin is called pitch angle θ and is defined as

$$\theta = \frac{2\pi}{L}, \tag{5.1}$$

where L is the smallest distance between spins whose pitch angle differs by 2π. The field theoretical bosonization calculations [6] suggest that for $|\alpha| > 0.25$, the system shows SDW$_n$ in low magnetic field, whereas it shows multipolar phase at high magnetic field [3]. The multipolar correlation of order p or boson propagator $\langle S_i^+ S_{i+1}^+ \cdots S_{p+i-1}^+ S_{i+r+1}^- S_{i+r+2}^- \cdots S_{i+r+p-1}^- \rangle$ is written [3] as

$$\begin{aligned} &\langle S_0^+ \cdots S_{p-1}^+ S_r^- \cdots S_{r+p-1}^- \rangle = (-1)^r \langle b_0 b_r^\dagger \rangle \\ &= \frac{A_m (-1)^r}{|r|^{1/\eta}} - \frac{\widetilde{A}_m (-1)^r}{|r|^{\eta + 1/\eta}} \cos(2\pi \rho r) + \cdots, \end{aligned} \tag{5.2}$$

where A_m and $\widetilde{A}_m$ are constants, η is twice of the Luttinger liquid parameter, and r represents distance. The density-density correlation is written as

$$\begin{aligned} C^L(r) = \langle S_0^z S_r^z \rangle &= \left\langle \left(\frac{1}{2} - p b_0^\dagger b_0\right)\left(\frac{1}{2} - p b_r^\dagger b_r\right)\right\rangle \\ &= M^2 - \frac{p^2 \eta}{4\pi^2 r^2} + \frac{A_z \cos(2\pi\rho r)}{|r|^\eta} + \cdots, \end{aligned} \tag{5.3}$$

where $\rho = \frac{1}{p}(1 - \frac{M}{M_0})$, M_0 is the saturation magnetization. The pitch angle $\theta = 2\pi\rho$ varies with the magnetic field. The spin density $\langle S_r^z \rangle$ calculated from the field theoretical method is written [3] as

$$\begin{aligned} \langle S_r^z \rangle &= \frac{1}{2}(1-p) - p z(r;q); \\ z(r;q) &= \frac{q}{2\pi} - a\frac{(-1)^r \sin(qr)}{f_{\eta/2}(2r)}; \\ q &= \frac{2\pi N}{N+1}(\rho - \frac{1}{2}); \\ f_\nu(x) &= \left[\frac{2(N+1)}{\pi}\sin\left(\frac{\pi|x|}{2(N+1)}\right)\right]^\nu. \end{aligned} \tag{5.4}$$

The pitch angle θ_T in transverse direction can also be extracted from the transverse correlation function $C^T(r) = \langle (S_i^x S_{i+r}^x + S_i^y S_{i+r}^y) \rangle$. However, the pitch angle θ in the longitudinal direction is calculated from $C^L(r)$ and spin density $\langle S_r^z \rangle$.

The $\langle S_r^z \rangle$ and $C^L(r)$ are shown in Fig. 5.1 (a) for $M = 0.35$, $|\alpha| = 1.0$ and $N = 168$. The $C^L(r)$ is scaled by 3.25 and r is shifted by 1.0 unit to match the magnitude of $\langle S_r^z \rangle$. Interestingly, the complex looking equation of $\langle S_r^z \rangle$ in Eq. 5.4 has similar variation as that of $C^L(r)$. All the $\langle S_r^z \rangle$ and $C^L(r)$ give the same pitch angle. The Friedel oscillation at the edge of the chain is seen in both $\langle S_r^z \rangle$ and $C^L(r)$. The spin densities are plotted in Fig. 5.1 (b) for $M = 0.05, 0.1, 0.25$ and 0.3. The amplitude of $\langle S_0^z S_r^z \rangle$ decreases with the distance, whereas $|\langle S_r^z \rangle|$ at site r is more or less constant with r. Therefore, it is easier to calculate θ from $\langle S_r^z \rangle$ than from $\langle S_0^z S_r^z \rangle$. We find that θ decreases with M and reduces to zero at $M = 0.5$ for the spin-1/2 system. These results are consistent with the Sudan *et al.* exact diagonalization results [4].

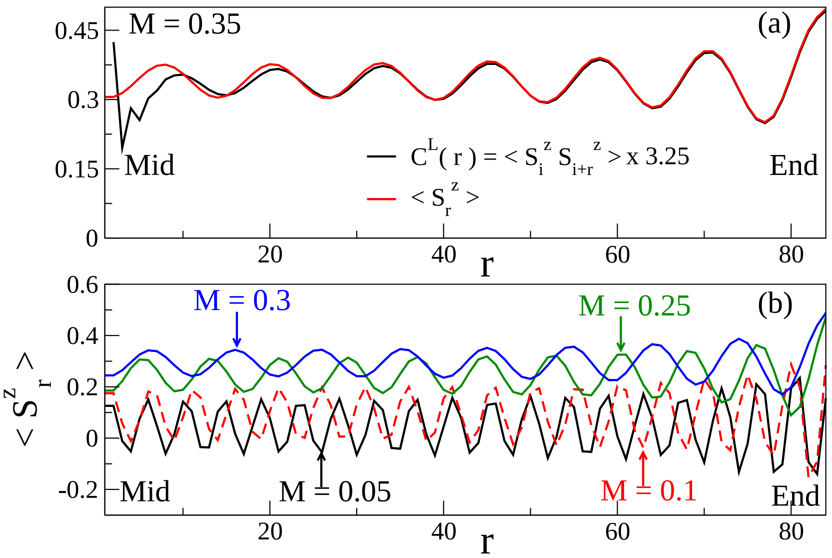

Figure 5.1: The upper panel (a) shows the spin density $\langle S^z_r \rangle$ and longitudinal correlation function $C^L(r)$ for $M = 0.35$. $C^L(r)$ is multiplied by 3.25 times and x-axis of this plot is shifted by 1 unit to match the magnitude and phase of $\langle S^z_r \rangle$. In the lower panel, spin densities $\langle S^z_r \rangle$ for $M = 0.05, 0.1, 0.25,$ and 0.3 are shown. For the $C^L(r)$ mid site of the chain is kept as reference site.

As shown in the Fig. 5.1 (a) θ calculated from $\langle S^z_r \rangle$ and $C^L(r)$ are same. With M the variations in θ_T of the transverse correlation functions $C^T(r)$ is less than 5%. The accurate calculation of θ near $M_0 \approx 0.5$ requires larger system size, and for these calculations we have used $N = 168$ for low magnetization and 368 for higher magnetization. The θ and θ_T are calculated from the $\langle S^z_r \rangle$ and the $C^T(r)$, respectively, for $|\alpha| = 0.265, 0.27, 0.3, 0.4,$ and 1.0 as a function of M/M_0 shown in Fig. 5.2 (a) and 5.2 (b). The filled symbols are the DMRG calculations for $N = 168$ with OBC, and dotted lines are fitted line with $\frac{\theta}{\pi} = \frac{1}{p}(1 - \frac{M}{M_0})$ where p is the order of the multipole.

In Fig. 5.2 (a) we notice that the variation of the θ with M shows linear relation $\frac{\theta}{\pi} = \frac{1}{p}(1 - \frac{M}{M_0})$ especially at large M. For $|\alpha| > 0.4$ and large M, θ varies linearly with M/M_0 with a slope $2/p = 1$. The linear behavior of θ deviates from the straight line at low M/M_0 for $|\alpha| \leqslant 0.6$. The deviation point for $|\alpha| = 0.4$ is at $M/M_0 \approx 0.28$. In the VC phase θ depends weakly on M as shown in Fig. 5.2 (a).

The phase boundary of the quadrupolar and the VC phase is estimated using the level crossing or magnetic step criterion as in Refs. [3, 27]. For $|\alpha| \geq 0.4$ results will be discussed in the later part of this section.

The three magnon bound phase or the triatic/SDW$_3$ phase occurs in the vicinity of $|\alpha| = 0.3$ and $\frac{\theta}{\pi}$ is less than 0.26 at $M < 0.21$ as shown in Fig 5.2 (a). At large M the slope of the green line in Fig. 5.2 (a) is $1/p = 1/3$. The phase boundary of the triatic/SDW$_3$ and the VC phase can also be estimated from the deviation of the $\frac{\theta}{\pi}$ from linear relation as shown in Fig. 5.2 (a). In fact θ weakly depends on M in the VC phase and remains constant for the given value of $|\alpha|$, whereas it varies linearly with slope $1/p = 1/3$ in the triatic/SDW$_3$ phase. The phase boundary of the triatic/SDW$_3$ and the VC phase calculated with this method is consistent with other calculations [3, 4]. The maximum value of θ for a multipole of order p for a given $|\alpha|$ is π/p, and it decreases with the number of magnons or p. Our DMRG result shows that for $|\alpha| = 0.265$ at large M,

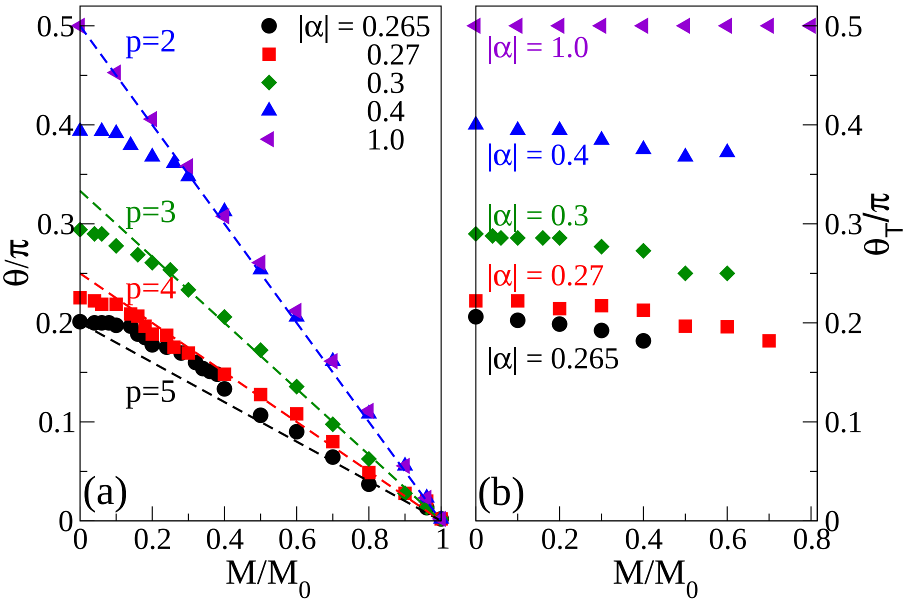

FIGURE 5.2: In panel (a); Pitch angle θ is calculated from $\langle S_r^z \rangle$ and $C(r)$. In panel (b) transverse pitch angle θ_T is calculated from transverse correlation as a function of M/M_0 for $|\alpha| = 0.265, 0.27, 0.3, 0.4$, and 1.0 are shown. The dashed lines in the left panel are fitted lines with the equation $\frac{\theta}{\pi} = \frac{1}{p}(1 - \frac{M}{M_0})$ where p is the order of the multipolar phase.

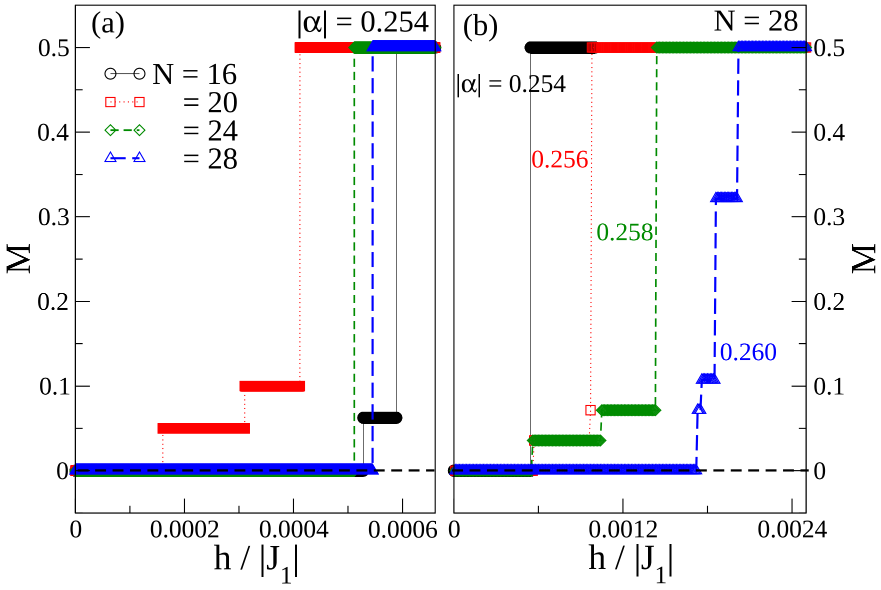

FIGURE 5.3: (a) Magnetization vs. axial magnetic field h for $|\alpha| = 0.254$ is shown. The calculations are done for system sizes $N = 16, 20, 24,$ and 28 with PBC. (b) The M vs. h for $N = 28$ for $|\alpha| = 0.254, 0.256, 0.258,$ and 0.26 with PBC is shown.

$p = 5$ state shows up for $M/M_0 > 0.4$, and system show the $p = 4$ state for intermediate magnetization $0.12 < M/M_0 < 0.4$. The vector chiral phase sets in below the $M/M_0 \leq 0.12$. For $|\alpha| < 0.265$, θ calculations become difficult with the approximate numerical technique. In this limit, energy states are closely spaced, and accurate determination of wavefunctions of the closely spaced energy levels is difficult.

In the quadrupolar phase the binding energy E_b of the magnons defined in Eq. 5.6 below is an important quantity to understand the condensation phenomenon. The $M - h$ curve is analyzed to see the effect of condensation of magnons. Near the critical point $|\alpha_c| = 0.25$, energy level spacings are tiny. Therefore, to maintain the accuracy of results, the ED method is used to solve the Hamiltonian for systems with $N = 16, 20, 24$ and 28. In Fig. 5.3 (a), the finite size effect on the $M - h$ curve is shown for $|\alpha| = 0.254$. The $N = 16$ shows steps of 1 and 7, whereas $N = 20$ shows steps in M of size 1 and 8. The gaps between the energy levels decrease with system size N, and for $N = 24$ and 28 system shows steps of $N/2$. For $|\alpha| = 0.254$ the value of p can be equal or higher than $N/2$. The finite system size effect on the gaps is weak in this parameter regime. The $M - h$ curve for different values of $|\alpha| = 0.254, 0, 256, 0.258$ and 0.26 are shown in Fig. 5.3 (b) for $N = 28$. We notice that the h required for saturation increases with $|\alpha|$. The step size depends on $|\alpha|$ for example, at $|\alpha| = 0.256$ and 0.258 system shows steps of 1 and 12, whereas for $|\alpha| = 0.26$ the steps are 1, 2 and 6. The VC phase exists in the low M limit, and the phase boundary decrease with $|\alpha|$. The magnetic steps or the order of multipole p increases rapidly with $1/|\alpha|$ near the critical point 0.25, and the magnetic gaps decrease with $|\alpha|$ as shown in Fig. 5.3 (a). Unfortunately, we need large system size to confirm the large $p > 14$, but these results are consistent with the prediction of the existence of larger p in Ref. [48].

In case of incommensurate spin density wave, there are level crossings or the gs degeneracies, and these two degenerate states have opposite inversion symmetry [27].

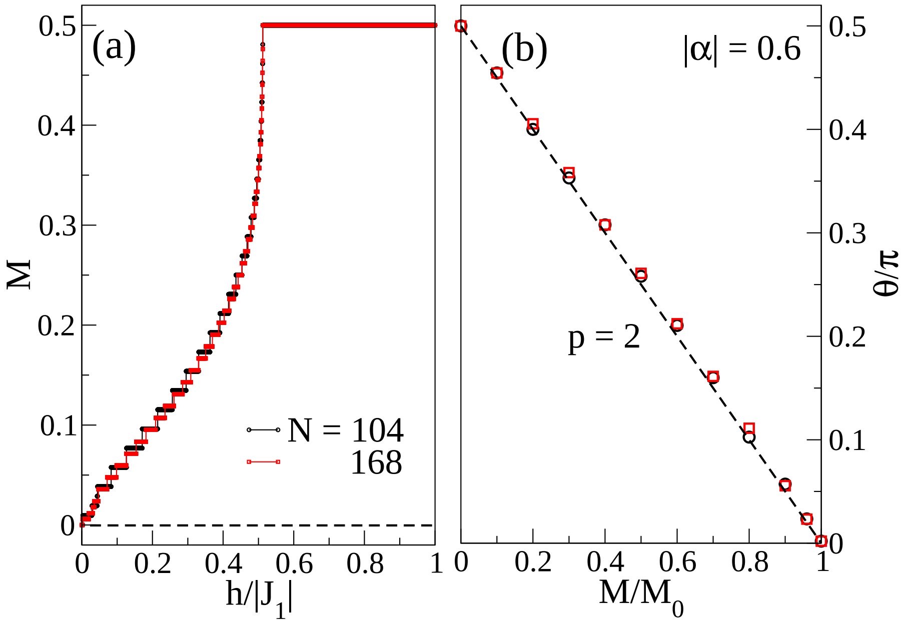

FIGURE 5.4: (a) $M-h$ plot for $|\alpha| = 0.6$ of system sizes $N = 104$ and 168 using DMRG with OBC is shown. (b) The pitch angle θ as a function of magnetization (M/M_0) for system sizes $N = 104$ and 168 at $|\alpha| = 0.6$ is shown. The dotted line is fitted line with $\frac{\theta}{\pi} = \frac{1}{p}(1 - \frac{M}{M_0})$ where $p = 2$.

Our ED calculations show that the gs energies are degenerate at large magnetization for $|\alpha| < 0.4$ for both odd and even S^z sectors. We calculate the z-component of VC order parameter $\kappa_i^z = \frac{1}{N}\sum_i \langle\psi_+| (S_i^+ S_{i+1}^- - S_i^- S_{i+1}^+) |\psi_-\rangle$ [27]. In the multipolar phase, the κ_i^z at large S^z limit is non-zero for $0.25 < |\alpha| < 0.55$ and system sizes up to $N = 28$. The κ_i^z for $N = 24$ system size is shown for different M for $0.25 < |\alpha| < 1.0$ in Ref. [27].

In the large $|\alpha|$ limit, the SDW$_2$ and SN phase exist in the presence of the magnetic field h. In the SN phase, two magnons can condense to form a single boson [3, 27], and this phase is determined based on the presence of magnetic step of two ($\Delta S^z = 2$) in $M - h$ curve [3, 27], order parameter and various correlation functions. In this phase a local order parameter is defined as in Refs. [1, 37, 38]

$$\rho_q = \langle\psi_{n+2}| S_i^+ S_{i+1}^+ |\psi_n\rangle , \tag{5.5}$$

where $|\psi_n\rangle$ and $|\psi_{n+2}\rangle$ are gs of $S^z = n$ and $n+2$ spin sector, but both of these are degenerate in the presence of an applied magnetic field. The order parameter ρ_q can be calculated analytically at $n = N/2 - 2$ and it is proportional to $1/\sqrt{N}$. However, for other values of n ρ_q is calculated numerically, and it has a non-zero value in a finite system size.

In this phase, the variation of θ, magnitude of E_b, and ρ_q as a function of M are calculated in the presence of magnetic field. The variation of magnetization M with h at $|\alpha| = 0.6$ is shown in Fig. 5.4 (a) for chains with $N = 104$ and 168. The magnetic step of $\Delta S^z = 2$ exists in the full range of M. The existing literature shows the SDW$_2$ phase at low magnetic field and SN type at high magnetic field [3, 37, 48]. To analyze the quadrupolar phase, θ is plotted as a function of M/M_0 in Fig. 5.4 (b) for two different $N = 104$ and 168 chains. The dashed line indicate $\frac{\theta}{\pi} = \frac{1}{p}(1 - \frac{M}{M_0})$ line with $p = 2$. These calculations demonstrate weak size dependence of the pitch angle θ.

The average binding energy of two magnons is defined as

$$E_b(n) = \frac{1}{2}\Big[E(n+2) + E(n) - 2E(n+1)\Big], \tag{5.6}$$

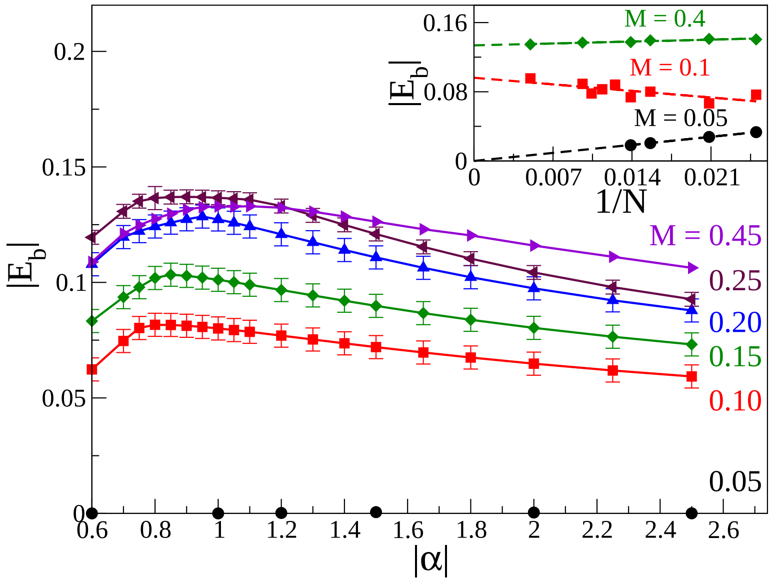

FIGURE 5.5: The main figure shows the binding energy $|E_b|$ as a function of $|\alpha|$ for magnetization $M = 0.05, 0.1, 0.15, 0.2, 0.25$, and 0.45. In the Inset $|E_b|$ vs. $1/N$ for magnetization $M = 0.05, 0.1$, and 0.4 at $|\alpha| = 1.0$ are shown.

where $E(n)$ is the energy of the system with even number of magnons n. The binding energy of two magnons in the SN/SDW$_2$ phase is shown as a function of N in the inset of Fig. 5.5. The $|E_b|$ has weak finite size dependence in large M limit, whereas it shows significant change with system size in low field limit. The finite size scaling are done for $M = 0.05, 0.1$ and 0.4 at $|\alpha| = 1.0$ for N up to 200. $|E_b|$ increases with M and has finite extrapolated value for $M > 0.1$. However, $|E_b|$ at low magnetization $M = 0.05$ is vanishingly small.

In Fig. 5.5 the extrapolated values of $|E_b|$ as a function of $|\alpha|$ for different $M = 0.05, 0.1, 0.15, 0.2, 0.25$ and 0.45 are shown. The error bars reflect the error in extrapolation and inaccuracy in DMRG calculations. We notice that $|E_b|$ increases with $|\alpha|$ and it attains a maximum value around $|\alpha_m(M)|$ for a given M, and decreases thereafter. The value of $|\alpha_m(M)|$ increases with M. The $|E_b|$ increases with M initially and either it saturates or decreases near the saturation magnetic field. This trend of $|E_b|$ is consistent with the calculations done by Onishi [46].

The bond energies are analyzed to understand the contribution of different bonds to E_b. In the large $|\alpha|$ limit the $J_1 - J_2$ model for a chain behaves like a zigzag chain, and the next nearest neighbor interaction J_2 of the model act as the interaction between the spins along the leg, whereas the nearest neighbor interaction J_1 becomes the interaction along the rung [16]. The contribution of different bonds in the E_b are calculated for $|\alpha| = 1.0$ and at $M = 0.25$ and 0.4 for a chain of sizes N =16, 20, 24 and 28 with PBC. However, data are shown only for $N = 24$ and 28 in the Table 5.1. The binding energy contribution of different bonds $E_b^{x,y}$ where x stands for longitudinal (L) or transverse (T) and y stands for leg (L) or rung (R). The E_b is defined in terms of E_b^{xy} as,

$$E_b(n) = \frac{1}{2}\Big[E_b^{x,y}(n+2) + E_b^{x,y}(n) - 2E_b^{x,y}(n+1)\Big]. \tag{5.7}$$

For $M = 0.25$ the major contribution to E_b are transverse component $E_b^{T,R}$, $E_b^{T,L}$ and $E_b^{L,R}$, however, transverse component weakens the E_b as shown in Table 5.1. The $E_b^{L,L}$ decreases with system size, whereas $E_b^{T,L}$ increases with the system size. The magnitude of $E_b^{T,R}$ is significantly smaller than the $E_b^{L,R}$. The major contribution of E_b comes from the $E_b^{L,R}$. The magnitude of $E_b^{T,R}$ is almost 1/3 of the $E_b^{L,R}$, but these two have opposite signs. However, both these quantities increase with M. For $M = 0.4$ both along the leg and the rung transverse bonds contributions

Table 5.1: The contribution of different bonds in the E_b are calculated for $|\alpha| = 1.0$ and at $M = 0.25$ and 0.4 for a chain of sizes N =16, 20, 24, and 28 with PBC

$\|\alpha\|$	*System*	E_b	M = 0.25		M = 0.4	
			$N(24)$	$N(28)$	$N(24)$	$N(28)$
1.0	Leg	$E_b^{L,L}$	-0.0408	-0.0713	-0.0332	-0.0237
		$E_b^{T,L}$	0.1935	0.2208	-0.2217	-0.0815
		Total	0.1526	0.1495	-0.2549	-0.1051
	Rung	$E_b^{L,R}$	-0.7103	-0.6600	-0.7150	-0.7493
		$E_b^{T,R}$	0.2070	0.1963	0.6597	0.5756
		Total	-0.5033	-0.4637	-0.0552	-0.1737
	Total binding energy		-0.3507	-0.3142	-0.3102	-0.2788

weaken the total E_b. The $E_b^{T,L}$ also decreases, whereas $E_b^{T,R}$ increases. The magnitude of $E_b^{L,R}$ and $E_b^{T,R}$ are very similar, but opposite to each-other for $M = 0.4$. In conclusion, rung contributes most of the E_b in small M, but contribution of leg increases with M of $M < M_0$. The E_b is still small, however, $E_b^{T,L}$ is significantly large.

5.2.2 Dimers in Spin Nematic Phase

In the paper by Chubukov, he suggested the existence of dimerized uniaxial SN phase which is different from the conventional dimerization where the two nearest spin form singlet pair [1]. In this type of dimerization state two neighboring spin forms spin $S = 1$ state. The gs wave function is written as

$$\begin{aligned}|\psi_{gs}\rangle &= \prod_{n=2L}\{n, n\pm 1\}, \{i, j\} \\ &= \prod_{n=2L}(|1\rangle_{n,n\pm1} + \eta|{-1}\rangle_{n,n\pm1})/\sqrt{1+\eta^2},\end{aligned} \tag{5.8}$$

where $|1\rangle$ and $|-1\rangle$ are $|\uparrow\uparrow\rangle$ and $|\downarrow\downarrow\rangle$ triplet states, respectively. Although, bosonization calculation by Hikihara *et al.* suggests that dimerization is proportional to $\cos(a\phi_- + \pi M)$ and their average vanishes to zero [3].

We notice that gs is doubly degenerate in odd S^z in a finite system with PBC for $|\alpha| > 0.5$ [27]. These two degenerate gs have opposite inversion symmetry. We notice that these degeneracies are independent of system size. In large J_2 limit

TABLE 5.2: B_{obc} for $|\alpha| = 1.0$ is shown at different M for different N.

$\|\alpha\|$	N	B_{obc}			
		$M = 0.1$	$M = 0.2$	$M = 0.3$	$M = 0.4$
1.0	48	0.0256	0.0205	0.0113	0.0012
	64	0.0242	0.0204	0.0073	0.0013
	72	0.0245	0.0184	0.0076	0.0017
	96	0.0207	0.0157	0.0076	0.0012
	144	0.0186	0.0147	0.0052	0.0007
	200	0.0183	0.0126	0.0049	0.0006

this system is mapped to a zigzag chain with leg A and B. In the odd S^z sectors the difference between the total spin densities on each leg A and B differ by 1. Therefore, the extra magnon is confined to either leg A or B depending on the symmetry of the system [27]. We note that the bond order parameter in the gs of odd S^z sectors have non-zero value in a finite system.

We calculate the dimer order parameter B_{obc} in OBC system in even S^z sector. In this sector, gs is non-degenerate and it shows the spiral arrangement of spins. We follow the standard procedure to calculate B_{obc} as in Refs. [14, 15]. The B_{obc} is defined as

$$B_{obc} = \langle\psi_{gs}|\, S_{N/2} \cdot S_{N/2+1} - S_{N/2+1} \cdot S_{N/2+2}\, |\psi_{gs}\rangle\,. \tag{5.9}$$

In this procedure, B_{obc} is calculated only for the middle bond of the system to avoid the boundary effect. The B_{obc} shows non-monotonic decreasing behavior with system size, and it is small for a large system as shown in Table 5.2. The non-monotonic behavior is associated with the spiral nature of the spin arrangement.

5.3 Quadrupolar Phase in Spin-1 Chains

In this section, we explore the SN/SDW$_2$ or quadrupolar phase for spin $S = 1$ for finite system size with PBC, and assuming the spins interaction follows the model Hamiltonian in Eq. 1.18.

For the model in Eq. 1.18, the FM to singlet crossover occurs at $|\alpha| = 0.25$ and the singlet state extends for all values of $|\alpha| > 0.25$. The singlet and the triplet excitation or spin gap near the critical point $|\alpha| \approx 0.25$ is small compare to the spin gap in AFM J_1 model. However, the double Haldane gap is observed in large $|\alpha|$ limit. The multipolar phase of higher order $p > 2$ is observed for $|\alpha| < 0.5$ which is consistent with earlier studies. The gs have spiral arrangement of the spins for $|\alpha| > 0.25$. A detailed study of these properties of the system will be presented somewhere else [49]. In this section SN or SDW$_2$ phase is explored for a spin-1

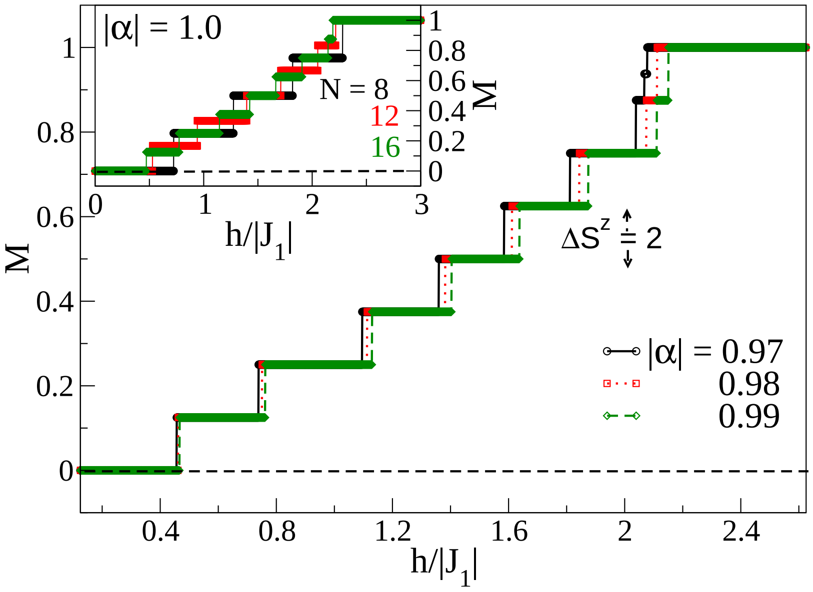

FIGURE 5.6: The $M-h$ curve is shown in the main figure for $|\alpha| = 0.97, 0.98$, and 0.99 and $N = 16$ chain with PBC using the ED for spin $S = 1$. In the inset the finite size effect of $M-h$ plot is shown for $N = 8, 12$, and 16 at $|\alpha| = 1.0$.

chain with PBC in the large $|\alpha|$ limit. We notice that the energy convergence in DMRG calculation depends on the number of relevant degrees of freedom m kept in the calculation, and energy of odd and even S^z sectors follow the linear relation with m but with different slopes. Therefore, we limit our calculations only to ED up to $N = 16$.

The $M-h$ plot for three $|\alpha| = 0.97, 0.98$ and 0.99 for $N = 16$ is shown in Fig. 5.6. The magnetic steps ΔS^z in a chain with OBC is one, however, in PBC chain it is two. This may be because of the edge modes at the end of the chain in OBC case. We notice that there are elementary steps of $\Delta S^z = 2$ in the magnetization with the magnetic field. The transition of steps $\Delta S^z = 1$ to $\Delta S^z = 2$ occurs at high magnetic field, and as $|\alpha|$ value increases the crossover point shifts to higher magnetic field. We also notice that for $|\alpha| > 1$, all the elementary steps are $\Delta S^z = 2$. In the main Fig. 5.6, variation of M with h is shown. The transition from mixed steps of $\Delta S^z = 1$ and $\Delta S^z = 2$ to purely $\Delta S^z = 2$ step occurs at $|\alpha| = 0.98$ for $N = 16$ for different M as shown in the main Fig. 5.6. To see the finite size effect, $M-h$ curve is plotted for $N=8,12$ and 16 for $|\alpha|=1.0$. We notice that the magnetic gaps decrease with N.

5.4 Discussion

In this work frustrated J_1-J_2 model Hamiltonian in Eq. 1.18 for spin-1/2 and 1 chains is studied. Our studies are focused on the model with FM NN and AFM NNN interactions in the presence of a magnetic field h. We use the ED and the DMRG numerical techniques to solve the Hamiltonian in Eq. 1.18. Here we have discussed multipolar phases, and especially, focused on SN phase of this model. The pitch angle θ, the binding energy E_b, the order parameter ρ_q and the steps in the magnetization are used to characterize the SN phase. The quadrupolar phase in the spin-1 chain is also discussed in the large $|\alpha|$ limit.

The multipolar phase is characterized based on the pitch angle θ calculated from spin density and correlation function. We show that spin density and longitudinal spin-spin correlations are commensurate with each other as shown in Fig. 5.1. The pitch angle θ vs. magnetization M plot shows the multipolar phase of the order up to $p=5$ at $|\alpha|=0.265$, however, the previous calculations by Sudan *et al.* are restricted to $p=4$ and all calculations were limited to system size up to $N=28$ [4]. In this work the DMRG calculations are done for system size up to $N=368$, especially in the large magnetization limit. We notice that in $M\rightarrow 0$ limit θ is weakly dependent on M, although, in the large magnetization limit, the pitch angle θ shows a linear behavior in the multipolar phase for $|\alpha|<0.60$. This result is consistent with the calculations of Sudan *et al.* [4]. The junction of flat regime and the linear variation of pitch angle θ is a good estimate of the VC and the multipolar phase boundary. The variation of θ_T calculated from transverse correlation is almost independent of magnetization, and it is explained in terms of the finite gap and exponentially decaying correlation function [3].

The characterization of multipolar phase of order $p>5$ with approximate numerical technique is a difficult task because of the presence of large number of nearly degenerate states, and in this case it is difficult to get pure gs without using symmetry. To avoid the accuracy problem the ED is used to calculate step in $M-h$ curve. After careful investigation of gaps we show that the multipolar phase of order $p=12$ at $|\alpha|=0.256$, and $p=N/2$ for $|\alpha|<0.254$ for $N\geq 24$. Although some of the previous works show that these are metamagnetic phases [3, 4], we find these are actually higher order multipolar phases with small binding energy.

The binding energy $|E_b|$ in SN/SDW$_2$ phase rapidly increases with $|\alpha|$ initially, and it has maxima at $|\alpha_m(M)|$. In the large $|\alpha|$ limit the bond energy contribution of the rung decreases with $|\alpha|$, therefore $|E_b|$ decreases with $|\alpha|$. The value of $|\alpha_m(M)|$ increases with M, and the $|E_b|$ have a broad maximum as a function of $|\alpha|$ as shown in the Fig. 5.5. The bond energy analysis is done in Table 5.1. For lower M, transverse bond energy for legs and rungs both have the contribution to E_b, whereas the longitudinal contribution of rung plays a major role in binding of two magnons. The contributions of legs and rungs for higher M have similar trend except that the magnitude of longitudinal contribution decreases in the leg, and it increases in the rung. The $E_b^{T,L}$ decreases for higher M, whereas $E_b^{T,R}$ increases significantly. The $E_b^{T,R}$ actually weakens the binding of the magnons and longitudinal component try to enhance the E_b. The values of E_b for $|\alpha|=0.5, 1, 1.5$ and 2 have similar value to the previous calculation by Onishi [46].

The earlier studies of J_1-J_2 model of general S chain show the absence of spin nematic phase in $S=1$ chain [43, 44]. However, the study of Balents *et al.* shows the presence of nematic phase in general spin using the Lifshitz non-linear sigma model [48]. Our finite size calculations at $|\alpha|>0.98$ show steps of 2 in $M-h$ curve and this results can be understood using their model [48]. The double Haldane phase agrees with Refs. [43, 44]. However, we note doubly degenerate gs in odd S^z sectors.

The bond dimerization in the SN phase at finite h has been under debate. Chubukov claims that there are $S=1$ dimerization and the doubly degenerate gs [1], but the analytical calculation by Hikihara *et al.* [3] shows the absence of dimerization. We show that the even S^z have non-degenerate and spiral gs. The odd S^z have doubly degenerate gs for PBC system. The bond order B_{obc} decreases non-monotonically with system size in even S^z sector and has very small value for finite $N = 200$.

In conclusion, we have studied the $J_1 - J_2$ model in an axial magnetic field h with FM J_1. The multipolar phases with multipole up to $p = 14$ are calculated. We have analyzed E_b in SN/SDW$_2$ phase, and we show that longitudinal energies of rung have a major contribution to the E_b. In this work, we have shown that magnitude of dimerization is vanishingly small, and gs is doubly degenerate in the SN phase.

The model Hamiltonian in Eq. 1.18 supports many quantum phases in the 1D system. There are many open questions to be answered, like how to characterize the SN phase and other multipolar phases, what happens to magnon pairing in large $|\alpha|$ limit, and how to increase the binding energies of magnon pairing. The RIXS is a good experimental tool which may distinguish the SDW$_2$ and SN phase. In the large $|\alpha|$ limit, the $J_1 - J_2$ chain should behave like two decoupled chains and their behavior looks like HAF chains. We can ask a question like what happens to magnon as low lying excitations should be similar to Heisenberg spin-1/2 one dimensional chain.

Bibliography

[1] A. V. Chubukov, Phys. Rev. B **44**, 4693 (1991).

[2] T. Vekua, A. Honecker, H. -J. Mikeska, and F. Heidrich-Meisner, Phys. Rev. B **76**, 174420 (2007).

[3] T. Hikihara, L. Kecke, T. Momoi, and A. Furusaki, Phys. Rev. B **78**, 144404 (2008).

[4] J. Sudan, A. Lüscher, and A. M. Läuchli, Phys. Rev. B **80**, 140402(R) (2009).

[5] J. Sirker, Phys. Rev. B **81**, 014419 (2010).

[6] T. Hamada, J. Kane, S. Nakagawa, and Y. Natusume, J. Phys. Soc. Jpn. **57**, 1891 (1988).

[7] S. Mahdavifar, J. Phys.: Condens. Matter **20**, 335230 (2008).

[8] M. Kumar, A. Parvej, and Z. G. Soos, J. Phys.: Condens. Matter, **27**, 316001 (7pp) (2015); M. Kumar, A. Parvej, and Z. G Soos, J. Phys.: Condens. Matter, **28**, 175603 (12pp) (2016).

[9] C. Itoi and S. Qin, Phys. Rev. B, **63**, 224423 (2001).

[10] C. K. Majumdar and D. K. Ghosh, J. Math. Phys. **10**, 1388 (1969).

[11] A. W. Sandvik, AIP Conf. Proc. **1297**, 135 (2010).

[12] T. Tonegawa and I. Harada, J Phys. Soc. Jpn. **56**, 21532167 (1987).

[13] R. Chitra, S. Pati, H. R. Krishnamurthy, D. Sen, and S. Ramasesha, Phys. Rev. B **52**, 6581 (1995).

[14] S. R. White and I. Affleck, Phys. Rev. B **54**, 9862 (1996).

[15] M. Kumar, S. Ramasesha, D. Sen, and Z. G. Soos, Phys. Rev. B **75**, 052404 (2007).

[16] M. Kumar, Z. G. Soos, D. Sen, and S. Ramasesha, Phys. Rev. B **81**, 104406 (2010).

[17] M. Kumar, S. Ramasesha, and Z. G. Soos, Phys. Rev. B **81**, 054413(2010).

[18] M. Kumar and Z. G. Soos, Phys. Rev. B **88**, 134412 (2013).

[19] F. D. M. Haldane, Phys. Rev. B **25**, 4925 (1982).

[20] K. Okamoto and K. Nomura, Phys. Lett. A **169**, 433 (1992).

[21] R. Bursill, G. A. Gehring, D. J. J. Farnell, J. B. Parkinson, T. Xiang, and C. Zeng, J. Phys: Condens. Matter **7**, 8605 (1995).

[22] D. V. Dmitriev and V. Ya. Krivnov, Phys. Rev. B **73**, 024402 (2006).

[23] F. Heidrich-Meisner, A. Honecker, and T. Vekua, Phys. Rev. B **74**, 020403(R) (2006).

[24] L. Kecke, T. Momoi, and A. Furusaki, Phys. Rev. B **76**, 060407(R) (2007).

[25] F. Heidrich-Meisner, I. P. McCulloch, and A. K. Kolezhuk, Phys. Rev. B **80**, 144417 (2009).

[26] S. Furukawa, M. Sato, and S. Onoda, Phys. Rev. Lett. **105**, 257205 (2010).

[27] A. Parvej and M. Kumar, J. Mag. Mag. Mater. **401**, 96-101 (2016).

[28] S. E. Dutton, M. Kumar, M. Mourigal, Z. G. Soos, J. -J. Wen, C. L. Broholm, N. H. Andersen, Q. Huang, M. Zbiri, R. Toft-Petersen, and R. J. Cava, Phys. Rev. Lett. **108**, 187206 (2012).

[29] S. Park, Y. J. Choi, C. L. Zhang, and S. W. Cheong, Phys. Rev. Lett. **98**, 057601 (2007).

[30] M. Hase, H. Kuroe, K. Ozawa, O. Suzuki, H. Kitazawa, G. Kido, and T. Sekine, Phys. Rev. B **70**, 104426 (2004).

[31] S. -L. Drechsler, O. Volkova, A. N. Vasiliev, N. Tristan, J. Richter, M. Schmitt, H. Rosner, J. Málek, R. Klingeler, A. A. Zvyagin, and B. Büchner, Phys. Rev. Lett. **98**, 077202 (2007).

[32] S. E. Dutton, M. Kumar, Z. G Soos, C. L Broholm, R. J. Cava, J. Phys.: Condens. Matter **24**, 166001 (2012); M. Kumar, S. E. Dutton, R. J. Cava, Z. G Soos, J. Phys.: Condens. Matter **25**, 136004 (2013).

[33] O. S. Volkova, I. S. Maslova, R. Klingeler, M. Abdel-Hafiez, Y. C. Arango, A. U. B. Wolter, V. Kataev, B. Büchner, A. N. Vasiliev, Phys. Rev. B **85**, 104420 (2012).

[34] M. Kumar and Z. G. Soos, Phys. Rev. B **85**, 144415 (2012).

[35] W. Eerenstein, N. D. Mathur, and J. F. Scott, Nature **442**, 759-765 (2006).

[36] H. Katsura, N. Nagaosa, and A. V. Balatsky, Phys. Rev. Lett. **95**, 057205 (2005).

[37] O. A. Starykh and L. Balents, Phys. Rev. B **89**, 104407 (2014).

[38] K. Penc and A. Läuchli, *Introduction to Frustrated Magnetism*, Springer Series in Solid-State Sciences, Vol. **164**, edited by C. Lacroix, P. Mendels, and F. Mila (Springer, Berlin-Heidelberg, 2011), pp. 331362.

[39] M. Enderle, B. Fåk, H. -J. Mikeska, R. K. Kremer, A. Prokofiev, and W. Assmus, Phys. Rev. Lett. **104**, 237207 (2010).

[40] L. J. P. Ament, M. V. Veenendaal, T. P. Devereaux, J. P. Hill, and J. V. D. Brink, Rev. Mod. Phys. **83**, 705 (2011).

[41] M. Sato, T. Momoi, and A. Furusaki, Phys. Rev. B **79**, 060406(R) (2009).

[42] M. Sato, T. Hikihara, and T. Momoi, Phys. Rev. B **83**, 064405 (2011).

[43] M. Arlego, F. Heidrich-Meisner, A. Honecker, G. Rossini, and T. Vekua, Phys. Rev. B **84**, 224409 (2011).

[44] A. K. Kolezhuk, F. Heidrich-Meisner, S. Greschner, and T. Vekua, Phys. Rev. B **85**, 064420 (2012).

[45] D. Dey, D. Maiti, and M. Kumar, Papers in Physics **8**, 080006 (2016).

[46] H. Onishi, J. Phys. Soc. Jpn. **84**, 083702 (2015).

[47] M. Mourigal, M. Enderle, B. Fåk, R. K. Kremer, J. M. Law, A. Schneidewind, A. Hiess, and A. Prokofiev, Phys. Rev. Lett. **109**, 027203 (2012).

[48] L. Balents and O. A. Starykh, Phys. Rev. Lett. **116**, 177201 (2016).

[49] S. Saha *et al.*, (unpublished).

Chapter 6

Study of the Dynamical Properties of the Multipolar Phase of Spin-1/2 Chain

6.1 Introduction

The frustrated low dimensional spin systems have been a frontier area of active research due to the existence of exotic phases in the system as discussed in chapter 1. These phases can be realized in some real materials like $LiCuVO_4$ [1], $LiCuSbO_4$ [2] etc. Although these systems are 3D in nature, but interaction along two axis are weak and modeled by the 1D isotropic $J_1 - J_2$ model with spin-1/2 in the presence of an axial magnetic field h given in Eq. 1.18 in chapter 1. The $J_1 - J_2$ model with FM J_1 and AFM J_2 in the presence of an axial magnetic field h is our main focus in this chapter. The field theoretical and numerical studies suggest that at high magnetic field h the system shows metamagnetic or multipolar such as dipolar, quadrupolar, octupolar, hexadecapolar phase etc. In this system multimagnon bind to form higher order of multipolar system. The order parameter of these phases are hidden in nature therefore there is no direct evidence for these phases

[3]. However, probes like INS and RIXS can indirectly shows the existence of these phases.

The lowest excitations in the $J_1 - J_2$ model are the magnon which is basically simultaneous flip of the spin in a 1D spin-1/2 chain, and these low-lying excitations can be investigated by INS. In neutron scattering process integer spin excitations are created, and whole process can be understood in terms of the single spin dynamical structure factor [4, 5].

6.2 Dynamical Structure Factor

The dynamical structure factor [4] in the frequency and momentum space is defined as

$$S^{\beta\beta}(q, \omega, M) = \sum_n \frac{| \langle \psi_n | S^\beta_q | \psi_0 \rangle |^2}{E_n - (E_0 + \omega) + i\eta}, \tag{6.1}$$

where $|\psi_0\rangle$ is the gs wavefunction for fixed $S^z = M$ and $|\psi_n\rangle$ is the n^{th} excited state for the same M or $M \pm 1$. S^β_q is defined as, $S^\beta_q = (\sqrt{2\pi/N}) \sum_j S^\beta_j e^{iqj}$, where $\beta = x, y$ and z-component. E_0 and E_n are the gs and n^{th} excited state energies, respectively, ω is the energy transferred to the spin lattice. η is broadening factor and is fixed at 0.1 for all the calculations.

6.2.1 Results for Dynamical Structure Factor

The general observations about the dynamical property and $M - h$ curve in the quadrupolar phase are presented here. In the later part we model the dynamical structure factor of $LiCuVO_4$ [15–17] and $LiCuSbO_4$ [2] compounds and also compare our results with the experimental data available in the literature. Some part of this section is published in Ref. [18].

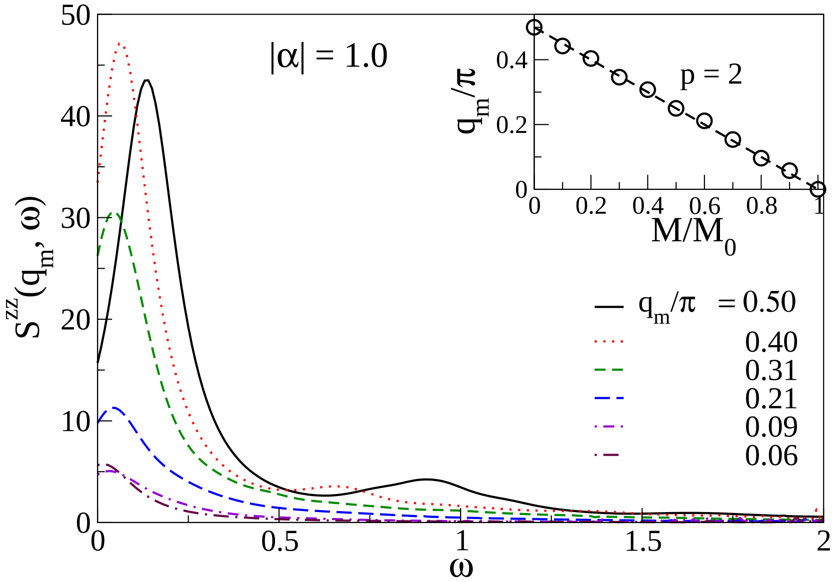

FIGURE 6.1: The longitudinal dynamical structure factor $S^{zz}(q_m, \omega)$ for $|\alpha| = 1.0$ as a function of ω with PBC using dynamical DMRG method is shown in the main figure for finite system size $N = 104$. The maximum value of q_m/π is calculated from $S^{zz}(q, \omega)$ and $q_m/\pi = 0.50, 0.40, 0.31, 0.21, 0.09,$ and 0.06 for $M = 0.0, 0.1, 0.2, 0.3, 0.4,$ and 0.45, respectively. Inset shows q_m/π as a function of M/M_0 for $|\alpha| = 1.0$ and dotted line is fitted line with $\frac{q_m}{\pi} = \frac{1}{p}(1 - \frac{M}{M_0})$ where $p = 2$.

6.2.2 Dynamical Structure Factor in the Quadrupolar Phase

The dynamical structure factor $S^{zz}(q_m, \omega)$ is shown in Fig. 6.1 for $|\alpha| = 1.0$. The $S^{zz}(q_m, \omega)$ for the system of size $N = 104$ with given M represents structure factor for a given value of momentum q_m for which the intensity is the highest. The $S^{zz}(q_m, \omega)$ for q_m is shown as a function of ω for different $M = 0.0, 0.1, 0.2, 0.3, 0.4$ and 0.45. As M increases the peak position of $S^{zz}(q_m, \omega)$ shifts towards lower q_m and ω_m. However, the longitudinal spin excitation is gapless in the SN/SDW$_2$ in the thermodynamic limit. For $M = 0.0$, q_m/π is at 0.5 and q_m decreases with increasing M. In the inset of Fig. 6.1 open circle represents the q_m for different values of M. The calculated q_m is fitted with a function $q_m/\pi = (1 - M/M_0)/2$. These features of SN/SDW$_2$ phase is directly examined by inelastic neutron scattering experiment in the presence of magnetic field h.

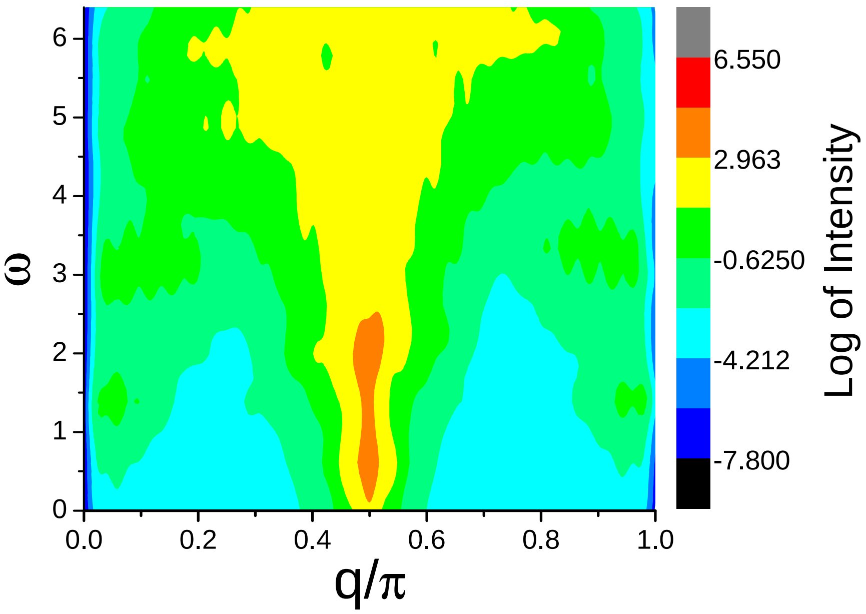

FIGURE 6.2: Calculated Longitudinal dynamical structure factor of $LiCuVO_4$ as a function of wave vector (q/π) and energy (ω). The color box is the longitudinal dynamical structure factor. The logarithm of $S(q, \omega)$ is shown for better resolution of intensities. The calculations are done for $J_1 = -1.6$ meV, $J_2 = 3.8$ meV for $M = 0.0$.

The existence of SN phase in a real material like $LiCuVO_4$ is confirmed in the presence of high magnetic field h. This material consists of planar arrays of spin-1/2 copper chains with a FM nearest neighbor J_1 and AFM next nearest neighbor exchange interactions J_2. The exchange interaction strengths are $J_1 = -1.6$ meV and $J_2 = 3.8$ meV, found by fitting the data of INS and other experiments [1].

We use these parameter values for our calculations. The dynamical structure factor $S^{zz}(q, \omega)$ in the absence of the magnetic field is shown in Fig. 6.2. The intensity is shown by the contour plots. The experimentally observed $S(q, \omega)$ in figure 2 of Ref. [15] shows as a function of q and $\omega > 3$ meV. The random phase approximation (RPA) calculation shows continuous intensity below $\omega < 5$ meV, whereas experimental data shows high intensity between $\omega = 3$ to 5 meV with momentum between $q/\pi = 0.2$ and 0.5. The $S(q, \omega)$ calculation in Ref. [17] also shows that peak is at $q = \pi/2$ and $\omega < 1$ meV for both the parameter. In Ref. [19], they considered $|\alpha| = 2$ for modeling this compound and they also show the highest intensity of $S(q,\omega)$ at $q = \pi/2$ and $\omega < 0.3$ meV. The experimental data is restricted to $\omega \geq 3$ meV and shows only higher level of excitations. For better resolution of intensity, we plot the logarithm of $S(q,\omega)$ intensity in Fig. 6.2. Our DMRG calculations shows that the most intense peak is at $q_m = \pi/2$ and $\omega = 0.4$ meV. In fact, there are several values of q and $\omega < 3$ meV at which this system shows the significant intensity of $S^{zz}(q,\omega)$. The $S(q,\omega)$ follows the sum rule and we notice that major part of the intensity sum is limited to smaller ω, and intensities of $S(q,\omega)$ observed experimentally are only a small fraction of the total intensity. Actually, this is easily justified by the slow variation of intensity for $\omega > 3$ meV in experimentally observed $S(q,\omega)$.

The binding energy $|E_b|$ and momentum q_m in the presence of magnetic field are two important quantities to characterize the SN phase. The INS experiment on LiCuVO$_4$ by Mourigal *et al.* in Ref. [16] shows the linear variation of momentum q with magnetic field in high magnetic field h limit. However, q is independent

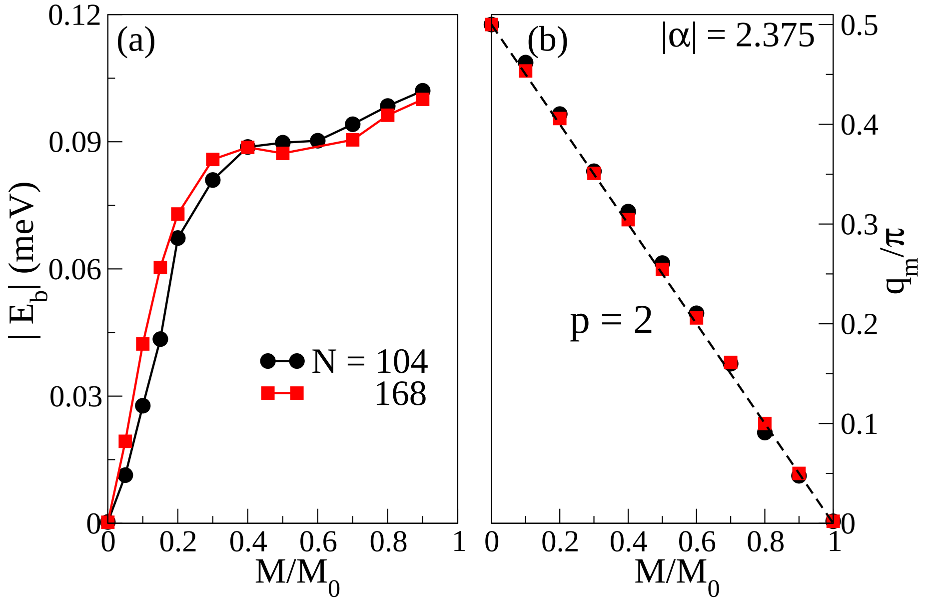

FIGURE 6.3: (a) The binding energy $|E_b|$ of LiCuVO$_4$ sample with $J_1 = -1.6$ meV, $J_2 = 3.8$ meV as a function of magnetization for the system sizes $N = 104$ and 168 using DMRG with OBC is shown. (b) The momentum q_m as a function of magnetization M/M_0 for the system sizes $N = 104$ and 168 using DMRG with PBC is shown. The dotted line is fitted by $\frac{q_m}{\pi} = \frac{1}{p}(1 - \frac{M}{M_0})$ where $p = 2$.

of the magnetic field below $h = 8T$. Our results for the $|E_b|$ and momentum q_m are shown in Fig. 6.3 (a) and (b) for two system sizes $N = 104$ and 168. The q_m for $\mathrm{LiCuVO_4}$ as a function of magnetization is shown in Fig. 6.3 (b) for $T = 0K$. We notice that q_m follows the linear relation with M with a slope of $1/p = 0.5$. The linear dependence of momentum is followed in the full range of M. The $|E_b|$ is shown in Fig. 6.3 (a) as a function of M/M_0. For $M = 0$, $|E_b|$ vanishes and it increases with M up to $M \approx 0.4$ and then remains constant and it increases thereafter.

Similarly, the existence of SN phase in a real material like $\mathrm{LiCuSbO_4}$ is also confirmed in the presence of high magnetic field h. In this material edge-sharing $\mathrm{CuO_6}$ octahedra form spin-1/2 copper chains with a FM nearest neighbor J_1 and AFM next nearest neighbor exchange interactions J_2. The exchange interaction

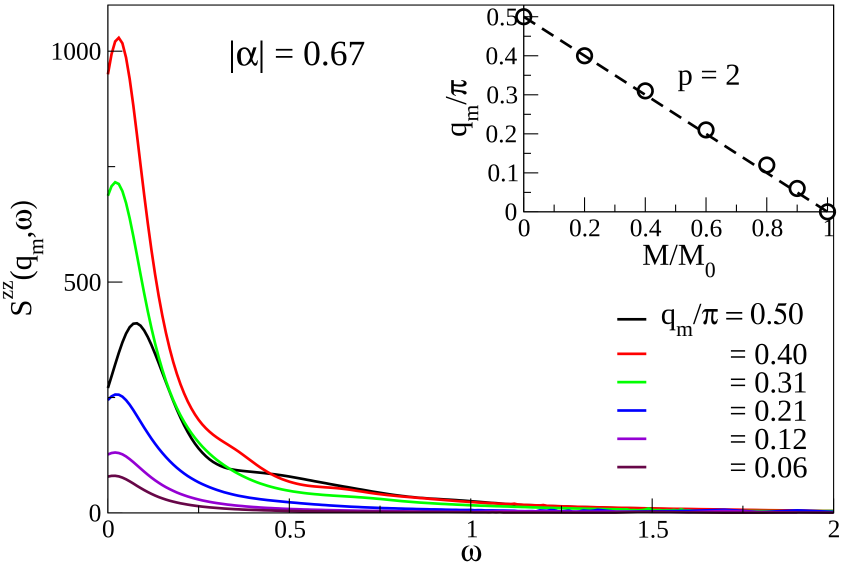

FIGURE 6.4: The longitudinal dynamical structure factor $S^{zz}(q_m, \omega)$ for $|\alpha| = 0.67$ as a function of ω with PBC using dynamical DMRG method is shown in the main figure for finite system size $N = 104$. The maximum value of q_m/π is calculated from $S^{zz}(q, \omega)$ and $q_m/\pi = 0.50, 0.40, 0.31, 0.21$, and 0.06 for $M = 0.0, 0.1, 0.2, 0.3$, and 0.45, respectively. Inset shows q_m/π as a function of M/M_0 for $|\alpha| = 0.67$ and dotted line is fitted line with $\frac{q_m}{\pi} = \frac{1}{p}(1 - \frac{M}{M_0})$ where $p = 2$.

strengths are $J_1 = -2.475$ meV and $J_2 = 1.66$ meV, found by fitting the thermodynamic data such as susceptibility, specific heat and other experiments [20].

The $S^{zz}(q_m, \omega)$ is shown in Fig. 6.4 for LiCuSbO$_4$ at $|\alpha| = 0.67$. The $S^{zz}(q_m, \omega)$ for the system size $N = 104$ with given M represents structure factor for a given value of momentum q_m for which the intensity is the highest. The $S^{zz}(q_m, \omega)$ for q_m is shown as a function of ω for different $M = 0.0, 0.1, 0.2, 0.3, 0.4$ and 0.45. As M increases the peak position of $S^{zz}(q_m, \omega)$ shifts towards lower q_m and ω_m. However, the longitudinal spin excitation is gapless in the SN/SDW$_2$ in the thermodynamic limit. For $M = 0.0$, q_m/π is at 0.5 and q_m decreases with increasing M. In the inset of Fig. 6.4 open circle represents the q_m for different values of M. The calculated q_m is fitted with a function $q_m/\pi = (1 - M/M_0)/p$ with $p = 2$. These features of SN/SDW$_2$ phase is directly examined by INS experiment in the presence of magnetic field h.

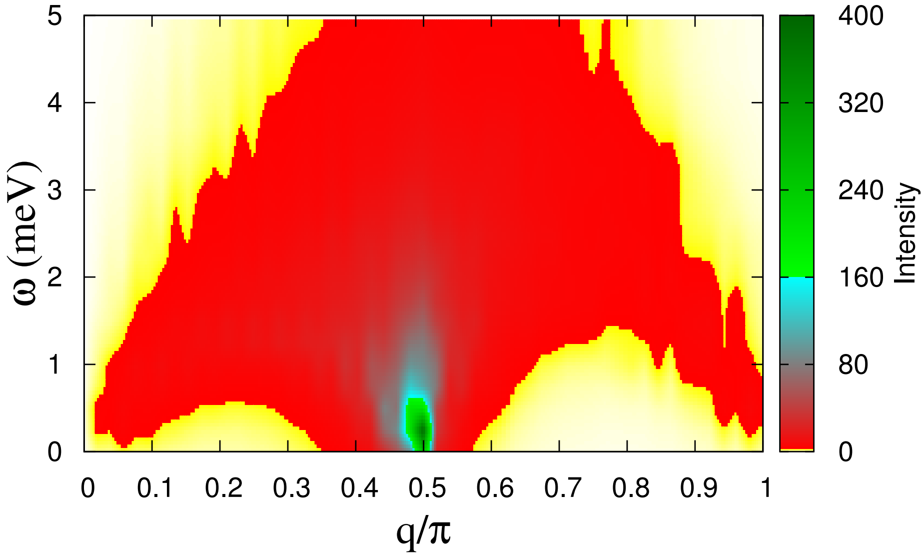

Figure 6.5: Calculated Longitudinal dynamical structure factor of LiCuSbO$_4$ as a function of wave vector (q/π) and energy (ω). The color box is the longitudinal dynamical structure factor $S(q, \omega)$ which is proportional to the intensity in INS experiment. The calculations are done for $J_1 = -2.475$ meV, $J_2 = 1.66$ meV for $M = 0.0$.

The dynamical structure factor $S^{zz}(q, \omega)$ of LiCuSbO$_4$ material in zero magnetic field is shown in Fig. 6.5. The intensity is shown by the contour plots. The experimentally observed $S(q, \omega)$ in figure 4 (a) and (e) of Ref. [2] shows as a function of q and ω. The experimental data shows that most of the intensity is observed below $\omega = 1.8$ meV and the highest intensity is observed at $q/\pi = 0.475$ for $\omega < 0.5$ meV. Our DMRG calculations for system size $N = 104$ at $M = 0.0$ shows that most intense peak is also coming at $q/\pi = 0.5$ and at $\omega = 0.25$ meV. Fig. 6.5 shows significant intensity for other values of q close to the $q/\pi = 0.5$ value. We notice that our calculated values of intensity and experimentally observed intensity agrees well.

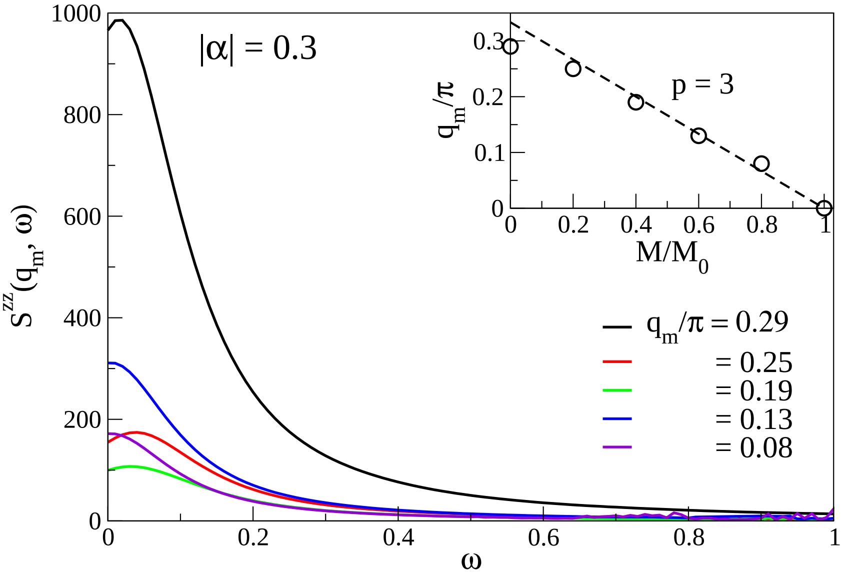

FIGURE 6.6: The longitudinal dynamical structure factor $S^{zz}(q_m, \omega)$ for $|\alpha| = 0.3$ as a function of ω with PBC using dynamical DMRG method is shown in the main figure for finite system size $N = 104$. The maximum value of q_m/π is calculated from $S^{zz}(q, \omega)$ and $q_m/\pi = 0.29, 0.25, 0.19, 0.13$, and 0.08 for $M = 0.0, 0.1, 0.2, 0.3$, and 0.4, respectively. Inset shows q_m/π as a function of M/M_0 for $|\alpha| = 0.3$ and dotted line is fitted line with $\frac{q_m}{\pi} = \frac{1}{p}(1 - \frac{M}{M_0})$ where $p = 3$.

6.2.3 Dynamical Structure Factor in the Triatic Phase

The general observations about the dynamical property in the triatic phase are presented here. We calculate the dynamical structure factor at $|\alpha| = 0.3$ which is shown in Fig. 6.6. The $S^{zz}(q_m, \omega)$ is calculated for the the system of size $N = 104$ with given M. For each M the structure factor has the highest intensity for a given value of momentum q_m. The $S^{zz}(q_m, \omega)$ for q_m is shown as a function of ω for different $M = 0.0, 0.1, 0.2, 0.3$, and 0.4. As M increases the peak position of $S^{zz}(q_m, \omega)$ shifts towards lower q_m and ω_m. For $M = 0.0$, q_m/π is at 0.29 and q_m decreases with increasing M. In the inset of Fig. 6.6 open circle represents the q_m for different values of M. The calculated q_m is fitted with a function $q_m/\pi = (1 - M/M_0)/p$ with $p = 3$. Therefore, in this parameter regime the system is in the triatic phase and this feature is shown in Fig. 5.2 (a) of chapter 5 [18]. These features of triatic phase can be directly examined by INS experiment in the presence of magnetic field h.

6.3 Resonant Inelastic X-ray Scattering Cross Section

In the previous section we have calculated the DSF of single magnon. In this process excitation takes place only between the states with difference in $S^z = \pm 1$. In the $J_1 - J_2$ model our gs is in a singlet spin sector, therefore, all the excitations correspond to the triplet spin sector. The low-lying excitation in the singlet energy manifold is still quite important and unexplored states. To understand the excitations in the singlet spin sector we use resonant inelastic X-ray scattering (RIXS) probe which excites two magnons at a time and the total spin of the system is conserved during this process[6–9].

In RIXS process the incident photon energy is resonant with the absorption edges such as K-edges, L-edges etc. of the material. Recent experiments reveal that indirect RIXS is also a new probe for the spin dynamics. It has two important advantages, first, it is sensitive to weak excitations which are difficult to probe by other techniques, and second, unlike optical methods it can probe directly the momentum dependence of those excitations. The magnetic RIXS scattering amplitude is expressed in terms of an intrinsic dynamical four spin correlation function of the system [6–9] and gives us information about the two magnon excitation process.

The RIXS scattering cross section where core-hole couples to magnetic excitations obtained from Krammers-Heisenberg formulae is [10]

$$I \propto \frac{d^2\sigma}{d\Omega d\omega} \propto \sum_f |A_{fi}|^2 \delta(\omega - \omega_{fi}) \qquad \text{and} \qquad A_{fi} = \omega_{res} \sum_n \frac{\langle f| \hat{D} |n\rangle \langle n| \hat{D} |i\rangle}{\omega_{in} - E_n - i\Gamma}, \tag{6.2}$$

where A_{fi} is the scattering amplitude from the initial state i to a final state f of the system. The momentum and energy transfer to the lattice are $q = q_{in} - q_{out}$ and $\omega = \omega^0_{in} - \omega^0_{out}$ where $q_{in/out}$ and $\omega^0_{in/out}$ are the momentum and energy of the incoming/outgoing photons. $\omega_{_{fi}} = E_f - E_i$ is the energy difference between the final and initial state. ω_{res} represents resonant energy, n denotes the intermediate state and $\hat{D}$ is the dipole operator which describes the excitation from initial to intermediate states and the de-excitation from intermediate to final state. E_n is the energy of the intermediate state $|n\rangle$ with respect to the resonance energy ω_{res}. $\omega_{in} = \omega^0_{in} - \omega_{res}$ is the energy of the incoming X-rays with respect to the resonant energy ω_{res}. Γ denotes core-hole energy broadening which is proportional to the inverse core-hole lifetime.

The RIXS amplitude is calculated by expanding it in a power series [11]

$$A_{fi} = \frac{\omega_{res}}{\Delta} \sum_{j=1}^{\infty} \frac{1}{\Delta^j} \langle f| \hat{D}(H_{int})^j \hat{D} |i\rangle \,, \tag{6.3}$$

where $\Delta = \omega_{in} - i\Gamma$ and H_{int} is the Hamiltonian in the intermediate state. The intermediate state Hamiltonian consists of two part $H_{int} = H_0 + H_1$, where H_0 is the Hamiltonian without core-hole interaction and H_1 is the Hamiltonian when core-hole interaction is present in the system. In order to calculate magnetic RIXS cross section one needs to find out the operator $(H_{int})^j$. So for $\Gamma \gg E_n$, A_{fi} can be expanded in a power series and the magnetic differential scattering cross section can be written as

$$I \propto \frac{d^2\sigma}{d\Omega d\omega} \propto S^{exch}(q, \omega), \tag{6.4}$$

where $S^{exch}(q, \omega)$ is the spin exchange dynamical structure factor and which has the form

$$S^{exch}(q, \omega) = 2\pi \sum_n |\langle 0| O_q^\beta |n\rangle|^2 \delta(\omega - \omega_n), \tag{6.5}$$

where $|0\rangle$ is the gs, $|n\rangle$ excited states, excitation energies $\omega_n = E_n - E_{gs}$, $\beta = x, y$ and z-component and the spin exchange operator is defined [6–10] as

$$O_q^\beta = \sqrt{2\pi/N} \sum_j (\mathbf{S}_j^\beta \cdot \mathbf{S}_{j+1}^\beta) e^{iqj}. \tag{6.6}$$

From above equations it is clear that magnetic RIXS measures four spin correlation function.

We use the ED method to numerically study RIXS data for the spin dynamics of the $J_1 - J_2$ model Hamiltonian in the presence of a magnetic field h in Eq. 1.18 in the chapter 1. Our main focus in this section is to analyze the singlet excitation at $h = 0$ especially for parameter $J_2/J_1 = -0.67$ and $J_2/J_1 = -2.375$ which are corresponding to model parameters for $LiCuSbO_4$ and $LiCuVO_4$. We know from the previous literature [2] that $LiCuSbO_4$ is close to the decoupled phase boundary, whereas $LiCuVO_4$ is in the decoupled phase.

In the Table 6.1 and 6.2, we show the matrix element $|\langle\psi_n|O_q^\beta|\psi_0\rangle|^2$ between the gs and first few low-lying n^{th} excited states with an energy gap ω_n for two compounds $LiCuVO_4$ and $LiCuSbO_4$. This matrix element is corresponding to the transition probability between these two states. We notice that the lowest singlet

Table 6.1: Non-zero value of matrix element of $|\langle\psi_n|O_q^\beta|\psi_0\rangle|^2$ for LiCuVO$_4$ compound with the model parameter $J_2/J_1 = -2.375$.

q/π	ω_n	$\lvert\langle\psi_n\vert O_q^\beta\vert\psi_0\rangle\rvert^2$	State
0.000	5.8033500	0.0098381	99
0.000	6.7819909	0.0594062	176
0.000	7.6080435	0.1518843	286
0.000	8.6209214	0.1700853	460
0.125	4.9408855	0.0604943	54
0.125	4.9408855	0.0604944	55
0.125	6.6782809	0.0001408	159
0.125	6.6782809	0.0001408	160
0.250	4.5288968	0.0374585	40
0.250	4.5288968	0.0374586	41
0.250	5.5979352	0.1101265	85
0.250	5.5979352	0.1101266	86
0.375	3.9885498	0.1626607	27
0.375	3.9885498	0.1626609	28
0.375	4.5590547	0.0036086	42
0.375	4.5590547	0.0036086	43
0.500	**2.1663662**	**0.0374589**	**4**
0.500	2.1663662	0.0374591	5
0.500	6.3765184	0.0066716	139
0.500	6.3765184	0.0066716	140
0.625	4.3805133	0.0058464	35
0.625	4.3805133	0.0058463	36
0.625	5.0331897	0.3643616	56
0.625	5.0331897	0.3643624	57
0.750	4.6329864	0.0003192	44
0.750	4.6329864	0.0003192	45
0.750	5.6038037	0.1374158	87
0.750	5.6038037	0.1374153	88
0.875	5.2487638	1.3171722	68
0.875	5.2487638	1.3171744	69
0.875	6.4607713	1.0378879	149
0.875	6.4607713	1.0378886	150
1.000	**2.8122485**	**5.1472578**	**10**
1.000	4.1711524	0.7469611	29
1.000	5.8970968	0.0659032	103
1.000	6.9872321	0.0497567	197

Table 6.2: Non-zero value of matrix element of $|\langle\psi_n|O_q^\beta|\psi_0\rangle|^2$ for $\mathrm{LiCuSbO_4}$ compound with the model parameter $J_2/J_1 = -0.67$.

q/π	ω_n	$\lvert\langle\psi_n\rvert O_q^\beta\lvert\psi_0\rangle\rvert^2$	State
0.000	1.1055764	0.0051602	81
0.000	1.5789376	0.0018013	282
0.000	1.7797202	0.0001214	428
0.000	1.9533380	0.0056165	597
0.125	1.3150370	0.0006355	146
0.125	1.3150370	0.0006355	147
0.125	1.3513820	0.0117696	154
0.125	1.3513820	0.0117696	155
0.250	0.8579474	0.0594621	43
0.250	0.8579474	0.0594621	44
0.250	1.5066503	0.0046201	229
0.250	1.5066503	0.0046201	230
0.375	0.7872240	0.1332974	28
0.375	0.7872240	0.1332976	29
0.375	1.3690526	0.0003898	163
0.375	1.3690526	0.0003898	164
0.500	0.4544681	0.2364985	9
0.500	0.4544681	0.2364984	10
0.500	1.2540109	0.0076316	129
0.500	1.2540109	0.0076316	130
0.625	0.9414896	0.0468909	51
0.625	0.9414896	0.0468908	52
0.625	1.2344720	0.0073031	123
0.625	1.2344720	0.0073031	124
0.750	0.8519285	0.0000427	41
0.750	0.8519285	0.0000427	42
0.750	0.9928458	0.0260883	62
0.750	0.9928458	0.0260884	63
0.875	0.8328589	0.0349973	35
0.875	0.8328589	0.0349973	36
0.875	1.1452325	0.0099153	84
0.875	1.1452325	0.0099153	85
1.000	**0.4260147**	**0.3651047**	**5**
1.000	1.0331458	0.4873706	68
1.000	1.1615131	1.0219555	98
1.000	**1.3629430**	**2.6490684**	**162**

is degenerate and have almost negligible transition probability. The highest transition probability highlighted with bold face in Table 6.1 and 6.2 is for magnons with $q \approx \pi$ which is very similar to INS results. We notice that lowest singlet states with finite matrix element are 4 and 5 for $LiCuVO_4$ and $LiCuSbO_4$ as lower states belong to triplet manifold. Most of dominant transition probabilities are restricted to low-lying states.

6.4 Discussion

We modeled the dynamical structure factor $S(q, \omega)$ of the $LiCuVO_4$ and $LiCuSbO_4$ compound using the parameter values at $|\alpha| = 2.375$ and $|\alpha| = 0.67$ in the literature [1, 2].

To characterize the SN/SDW_2 or quadrupolar phase the dynamical structure factor $S(q, \omega)$ is analyzed, and we notice that the momentum q_m of most intense peak of $S(q, \omega)$ for a given M varies linearly with M. This result can be directly confirmed by the INS experiments. The $LiCuVO_4$ is the most studied material for SN/SDW_2 phase, and we calculate the $S(q, \omega)$ in the absence of magnetic field h. The high energy peak is consistent with the earlier results, but the most intense peak is at $q = \pi/2$ and $\omega = 0.4$ meV. We also predict the dependence of q_m as a function of M and the $M - h$ curve for a single crystal of this compound. The linear variation of q with magnetic field h is shown for $LiCuVO_4$ at a high magnetic field by Mourigal *et al.* [16]. However, a more accurate measurement should be performed at a low field to verify the theoretical predictions. For this material, our calculation shows the linear variation of q_m with M for longitudinal $S^{zz}(q, \omega)$ for the given parameter in Ref. [1]. We also analysed the RIXS data for gs of $LiCuVO_4$ and $LiCuSbO_4$.

In conclusion, we have studied the dynamical properties of the $J_1 - J_2$ model in the presence of an axial magnetic field h. We have shown the characterization of the SN phase with INS experiment and also predicted the $q_m - M$ relation. We think that the most of intensities of $S(q, \omega)$ in $LiCuVO_4$ is below 3 meV and the most intense peak is at $q = \pi/2$ and $\omega = 0.4$ meV. We have also characterized the dynamical structure factor for LiCuSbO_4 and also predicted the $q_m - M$ relation which confirms the existence of SN/SDW_2 phase. We have shown the triatic ($p = 3$) phase by analyzing dynamical structure factor in the presence of a magnetic field h. Our small system size calculation using ED shows that excitations in the system which is probed through RIXS is corresponding to the singlet sector.

Bibliography

[1] M. Enderle, C. Mukherjee, B. Fåk, R. K. Kremer, J. -M. Broto, H. Rosner, S. -L. Drechsler, J. Richter, J. Málek, A. Prokofiev, W. Assmus, S. Pujol, J. -L. Raggazzoni, H. Rakoto, M. Rheinstadter, and H. M. Rønnow, Eur. Phys. Lett. **70**, 237243 (2005).

[2] S. E. Dutton, M. Kumar, M. Mourigal, Z. G. Soos, J. -J. Wen, C. L. Broholm, N. H. Andersen, Q. Huang, M. Zbiri, R. Toft-Petersen, and R. J. Cava, Phys. Rev. Lett. **108**, 187206 (2012).

[3] T. Hikihara, L. Kecke, T. Momoi, and A. Furusaki, Phys. Rev. B **78**, 144404 (2008).

[4] G. Müller, H. Thomas, H. Beck, and J. C. Bonner, Phys. Rev. B **24**, 1429 (1981).

[5] H. Onishi, J. Phys. Soc. Jpn. **84**, 083702 (2015).

[6] L. J. P. Ament, M. van Veenendaal, T. P. Devereaux, J. P. Hill, and J. van den Brink, Rev. Mod. Phys. **83**, 705 (2011).

[7] J. van den Brink and M. van Veenendaal, Eur. Phys. Lett. **73**, 121-127 (2006).

[8] J. van den Brink, Eur. Phys. Lett. **80**, 47003 (2006).

[9] A. Klauser, J. Mossel, Jean-Sébastien Caux, and J. van den Brink, Phys. Rev. Lett. **106**, 157205 (2011).

[10] H. A. Kramers and W. Heisenberg, Z. Phys. **31**, 681 (1925).

[11] T. Tohyama, H. Onodera, K. Tsutsui and S. Maekawa, Phys. Rev. Lett. **89**, 257405 (2002), K. Tsutsui, T. Tohyama, and S. Maekawa, Phys. Rev. Lett. **91**, 117001 (2003).

[12] D. Dey, D. Maiti, and M. Kumar, Papers in Physics **8**, 080006 (2016).

[13] S. Ramasesha, Z. Shuai, and J. L. Brèdas, Chem. Phys. Lett. **245**, 224-229 (1995).

[14] E. Jeckelmann, Phys. Rev. B **66**, 045114 (2002).

[15] M. Enderle, B. Fåk, H. -J. Mikeska, R. K. Kremer, A. Prokofiev, and W. Assmus, Phys. Rev. Lett. **104**, 237207 (2010).

[16] M. Mourigal, M. Enderle, B. Fåk, R. K. Kremer, J. M. Law, A. Schneidewind, A. Hiess, and A. Prokofiev, Phys. Rev. Lett. **109**, 027203 (2012).

[17] S. -L. Drechsler, S. Nishimoto, R. O. Kuzian, J. Málek, W. E. A. Lorenz, J. Richter, J. van den Brink, M. Schmitt, and H. Rosner, Phys. Rev. Lett. **106**, 219701 (2011).

[18] A. Parvej and M. Kumar, Phys. Rev. B **96**, 054413 (2017).

[19] J. Ren and J. Sirker, Phys. Rev. B **85**, 140410 (R) (2012).

[20] D. Dey, M. Kumar, S. E. Dutton, R. J. Cava, and Z. G. Soos (to be published in Phys. Rev. B).

Chapter 7

Conclusion

In conclusion, this thesis presents a detailed study of the exotic phases, spin dynamics, and their characterization for the frustrated $J_1 - J_2$ model Hamiltonian in Eq. 1.18 of chapter 1 with AFM and FM J_1 and AFM J_2 for spin-1/2 chain in the absence and presence of a magnetic field h. We have presented the numerical evidence for the quantum critical points $P2$ and $P3$ between gapped IC phases and a gapless decoupled phase with QLRO($\pi/2$) in the quantum phase diagram of $J_1 - J_2$ model in the absence of the magnetic field h. The quantum phase diagram of this model is shown in Fig. 3.1 for the Hamiltonian in Eq. 1.17 in chapter 3 of this thesis. The decoupled phase is non-degenerate with $q_G = \pi/2$ between $P2 = -1.24$ and $P3 = 0.44$ as shown in Fig. 3.1. The characterization of the decoupled phase has shown based on following criteria like level crossing, divergence of structure factor peak, and jump in spin densities in the lowest triplet state. The divergent structure factor peaks in the gs denote the critical gapless phase with QLRO with wave vector $q_G = \pi/2$ or π.

Furthermore, this thesis elaborates numerical studies of exotic phases in the isotropic $J_1 - J_2$ model with FM J_1 and AFM J_2 exchange interaction in the axial magnetic field h. In this system, Z_2 symmetry is spontaneously broken in the presence of the axial magnetic field. In earlier studies, the VC phase has been characterized based on various kinds of correlation functions like current-current correlation function and scalar chiral correlation etc. Our calculations suggest that this correlation function in a finite system can be non-zero even in the absence of the VC phase. The order parameter $\boldsymbol{\kappa}$ can be calculated using the broken symmetry states in this model, and it is shown that there are degeneracies in the lower states of $S^z = 0$. A large number of level crossings occur at different values of $|\alpha|$ in the presence of spiral phase. The VC order parameter $\boldsymbol{\kappa}$ is proportional to the electronic polarization $\mathbf{P} \propto \boldsymbol{\kappa}$ in the improper multi-ferroic materials such as $\mathrm{LiCuVO_4}$. A new quantum phase diagram of the $J_1 - J_2$ model in the presence of the axial magnetic field is constructed, and the VC phase is shown to exist only in the narrow range of parameter space.

In this thesis, we have also studied higher order multipolar phase of order up to $p = 14$. These studies are done based on the magnetic steps in $M - h$ curve and the variation of the pitch angle between neighboring spins with magnetic field. We have analyzed binding energy E_b in the SN/SDW$_2$ phase and show that the longitudinal component of bond energy of zigzag ladder of rung have major contribution to the E_b. The binding energy of the two magnons decreases with $|\alpha|$. It is shown that the existence of quadrupolar and triatic phase can be characterized through INS experiments, by measuring the dynamical structure factor. The momentum q of the most intense peak varies linearly with the magnetization M. We have shown this relation to $\mathrm{LiCuVO_4}$ and $\mathrm{LiCuSbO_4}$ compounds. For given parameters of $\mathrm{LiCuVO_4}$, most of the intensities of $S(q, \omega)$ in $\mathrm{LiCuVO_4}$ is below 3 meV, and the most intense peak is at $q = \pi/2$ and $\omega = 0.4$ meV. In this thesis, we have shown that magnitude of dimerization is vanishingly small, and gs is doubly degenerate in the SN phase. The existence of the quadrupolar phase is shown for the frustrated FM spin-1 $J_1 - J_2$ model with FM J_1 and AFM J_2 based on the step in the magnetization in the presence of magnetic field h.